University of Alberta

MAGNETICALLY ACTUATED CMOS MICROMACHINED MICROMIRRORS

by

Xiaohong Quan

A thesis submitted to the Faculty of Graduate Studies and Research in partial fulfillment of the requirements for the degree of Mater of Science.

Department of Electrical and Computer Engineering

Edmonton, Alberta

Fall, 2004

Reproduced with permission of the copyright owner. Further reproduction prohibited without permission.

Library and Archives Canada

Published Heritage Branch

395 Wellington Street
Ottawa ON K1A 0N4
Canada

Bibliothèque et Archives Canada

Direction du Patrimoine de l'édition

395, rue Wellington
Ottawa ON K1A 0N4
Canada

Your file Votre référence
ISBN: 0-612-95838-8
Our file Notre référence
ISBN: 0-612-95838-8

The author has granted a non-exclusive license allowing the Library and Archives Canada to reproduce, loan, distribute or sell copies of this thesis in microform, paper or electronic formats.

L'auteur a accordé une licence non exclusive permettant à la Bibliothèque et Archives Canada de reproduire, prêter, distribuer ou vendre des copies de cette thèse sous la forme de microfiche/film, de reproduction sur papier ou sur format électronique.

The author retains ownership of the copyright in this thesis. Neither the thesis nor substantial extracts from it may be printed or otherwise reproduced without the author's permission.

L'auteur conserve la propriété du droit d'auteur qui protège cette thèse. Ni la thèse ni des extraits substantiels de celle-ci ne doivent être imprimés ou aturement reproduits sans son autorisation.

In compliance with the Canadian Privacy Act some supporting forms may have been removed from this thesis.

Conformément à la loi canadienne sur la protection de la vie privée, quelques formulaires secondaires ont été enlevés de cette thèse.

While these forms may be included in the document page count, their removal does not represent any loss of content from the thesis.

Bien que ces formulaires aient inclus dans la pagination, il n'y aura aucun contenu manquant.

Canada

Reproduced with permission of the copyright owner. Further reproduction prohibited without permission.

ACKNOWLEDGEMENTS

I would like to express my sincere gratitude to my supervisors, Dr. A.M. Robinson and Dr. J.N. McMullin, for their patience, encouragement and guidance throughout this research work. Special appreciation should be extended to Dr. R.P.W. Lawson, Dr. F. Vermeulen, Dr. M. Brett, and Dr. C. Backhouse, for their enlightening discussions and help in various areas.

I am also grateful for the support provided by Canadian Microelectronics Corporation (CMC), as well as the services afforded by the University of Alberta Micromachining and Nanofabrication Facility (NanoFab). Special thanks to D. Chambers, M. Aktary, K. Westra, and S. Bozic for their instruction and assistance with the facilities at NanoFab, as well as for their help suggestion and advice.

It is also my wish to extend special thanks to D. Lu, K.B. Brown, M. Argument, H. Qiao, M. Hu, J. Foo, A. Peterson and J. Yang for their knowledgeable advice and tremendous help throughout various stages of this work.

It is a pleasure to thank my friend E. Chun for insightful ideas, encouragement and invaluable help.

Finally I would like to express my thanks to my parents and my sisters for their love. This thesis is dedicated to them.

Reproduced with permission of the copyright owner. Further reproduction prohibited without permission.

Table of Contents

Chapter 1

Introduction 1

1.1 CMOS Micromachining 1

1.2 Optical MEMS Switching 2

1.3 Thesis Overview 3

Chapter 2

Design and Fabrication of Micromirror Devices 5

2.1 The Micro-mirror Structures 5

2.2 Design Flow for CMOS Micromachined Micromirrors 9

2.3 Fabrication of Micromirror Devices 11

2.4 Post-processing 12

2.4.1 XeF_2 isotropic silicon etching 13

2.4.2 TMAH anisotropic silicon etching 15

2.4.3 The problem of residues 19

Chapter 3

Analytical Estimation 22

3.1 Actuation Modes 22

Reproduced with permission of the copyright owner. Further reproduction prohibited without permission.

3.2 Theoretical Calculation 24
3.2.1 Static Modeling for Device A1 26
3.2.1.1 Static Deflection Mode I: angular deflection *26*
3.2.1.2 Static Deflection Mode II: parallel movement *32*
3.2.2 Dynamic Response Modeling 34
3.2.2.1 Classical Vibration Theory for Single Degree-of-freedom Systems35
3.2.2.2 Dynamic Behaviour for Torsional Systems *37*
3.2.2.3 The Vertical Vibration *39*

Chapter 4

ANSYS Simulation 41
4.1 Building Models 42
4.1.1 The Basic Models Using Element SOLID92 42
4.1.2 Simplified Models Using Element SOLID46 45
4.2 Static and Dynamic Analyses 46
4.3 ANSYS simulation Results 47
4.4 Limitation of ANSYS Simulation for MEMS devices 54

Chapter 5

Experiments and Results 55
5.1 Experimental Setup for Magnetically Actuation 55
5.2 Angular Deflection 57
5.2.1 Optical Detection Method to Measure Angular deflection of Micromirrors 57
5.2.2 Experimental Results of the Angular Deflection Testing 59

Reproduced with permission of the copyright owner. Further reproduction prohibited without permission.

5.2.2.1 Static Deflection *59*

5.2.2.2 Dynamic Response *63*

5.2.3 Discussion on the Angular Deflection Testing 66

5.2.3.1 Static Deflection *66*

5.2.3.2 Dynamic Response *71*

5.3 Parallel Displacement 76

5.3.1 Optical Detection Method to test parallel displacement of Micromirrors76

5.3.2 Results and Discussion 78

5.4 Device Design and Optimization 83

5.5 Potential Applications 84

Chapter 6

Conclusions and Future Work 86

6.1 Magnetically Actuated Micromirror devices 86

6.2 Future work 87

References 89

Appendix A

The calculation of twist angle on the support arm in device A1 94

Appendix B

B-I: Figures of ANSYS Simulation Results 100

B-II: ANSYS Simulation Command files 105

Reproduced with permission of the copyright owner. Further reproduction prohibited without permission.

List of Tables

Table (2-1) Process sequences of TMAH etching 18

Table (3-1): Thickness and material properties of constitutive layers [26] 25

Table (3-2): The results of twist angles for micromirror device A1 31

Table (4-1) ANSYS results: Natural frequencies of micromirror devices.................... 48

Table (5-1): Finite element, analytical and optical results for Figures 5.14, 5.15, and 5.16 70

Table (5-2): Finite element, analytical and optical results for Figures 5.17, 5.18, and 5.19 74

Table (5-3): The errors of two finite element analysis models. 75

Reproduced with permission of the copyright owner. Further reproduction prohibited without permission.

List of Figures

Figure2.1: (a) Photograph of an unetched micromirror device (Unit A1); (b) Metal I layer distribution: top edge on device Unit A1; (b) Metal II layer distribution: bottom edge on device Unit A1. 6

Figure 2.2: Different designs of micromirror devices on one chip 7

Figure 2.3: (a) Photograph of an etched micromirror device (Unit D); (b) Metal II layer distribution: left and right traces on device Unit D; (c) Metal I layer distribution: top and bottom traces on device Unit D...8

Figure 2.4: Layout design flow for CMOS micromachined micromirror devices........10

Figure 2.5 The schematic cross section of a typical CMOS micromaching fabrication11

Figure 2.6: Schematic cross-sectional view of two types of silicon etching 12

Figure 2.7: XeF_2 etching system schematic...13

Figure 2.8: Undercutting, cracking and breakage on XeF_2 etched chips......................15

Figure 2.9 TMAH silicon etching system...17

Figure 2.10: residues after different etching procedures..21

Figure 3.1: Magnetic actuation principle for micromirror structures 23

Figure 3.2: Two modes of platform movement 24

Figure 3.3: The cross-section of a support arm..26

Reproduced with permission of the copyright owner. Further reproduction prohibited without permission.

Figure 3.4: The mechanical equilibrium of the micromirror device A1 27

Figure 3.5: The rotation angles of the arm and the platform of device A1...................28

Figure 3.6: Composite arm of two materials 29

Figure 3.7: Schematic diagrams of clamped-clamped beams.......................................32

Figure 3.8: The cross-sectional view of a support arm: (a) original; (b) transformed..33

Figure 3.9: The single degree of freedom system subject to forced vibration with viscous damper...35

Figure 3.10: Example of a harmonic response curve showing half power points and bandwidth..37

Figure 4.1: Schematic of the 3-D 10-node Tetrahedral Structural Solid element SOLID92 43

Figure 4.2: The half model of a micromirror device...44

Figure 4.3: Schematic of the 3-D 8-node Layered Structural Solid element SOLID4645

Figure 4.4: Cross-sectional view of meshing results on the arm 46

Figure 4.5: ANSYS models of the micromirror device A2 under influence of simulated Lorentz forces 47

Figure 4.6: The angular deflection of micromirror devices..49

Figure 4.7: The parallel displacement of micromirror devices....................................50

Figure 4.8: Stress on micromirror devices during tilting...51

Figure 4.9: Stress on micromirror devices during parallel moving. 52

Reproduced with permission of the copyright owner. Further reproduction prohibited without permission.

Figure 4.10: Vibration modes of the micromirror device A1. 53

Figure 4.11: Vibration modes of the micromirror device A2. 53

Figure 5.1: The external magnetic field. 56

Figure 5.2: The experimental setup for the angular deflection measurement..............57

Figure 5.3: Deflection angle illustration. 58

Figure 5.4: Static angular deflection of micromirror device A1.................................60

Figure 5.5: Static angular deflection of micromirror device A2.................................60

Figure 5.6: Static angular deflection of micromirror device C. 61

Figure 5.7: Static angular deflection of micromirror device A1 due to Lorentz forces only. 62

Figure 5.8: Static angular deflection of micromirror device A2 due to Lorentz forces only. 62

Figure 5.9: Static angular deflection of micromirror device C due to Lorentz forces only. 63

Figure 5.10: Dynamic angular deflection of micromirror device A1. 64

Figure 5.11: Dynamic angular deflection of micromirror device A2. 64

Figure 5.12: Dynamic angular deflection of micromirror device C. 65

Figure 5.13: Maximum angular deflections at resonance for given value of AC current. 66

Figure 5.14: ANSYS, theoretical, and optical experimental data for static angular deflection of micromirror device A1. 67

Reproduced with permission of the copyright owner. Further reproduction prohibited without permission.

Figure 5.15: ANSYS simulation and optical experimental data for static angular deflection of micromirror device A2. 69

Figure 5.16: ANSYS simulation and optical experimental data for static angular deflection of micromirror device C...69

Figure 5.17: ANSYS, theoretical, and optical experimental data for dynamic response of micromirror device A1 (angular deflection). 72

Figure 5.18: ANSYS simulation and optical experimental data for dynamic response of micromirror device A2 (angular deflection mode). 73

Figure 5.19: ANSYS simulation and optical experimental data for dynamic response of micromirror device C (angular deflection mode). 73

Figure 5.20: The experimental setup for the parallel displacement measurement........76

Figure 5.21: The interference fringe movements under different driving currents. 79

Figure 5.22: The interference fringe movements with or without external magnetic field. 80

Figure 5.23: The parallel displacement of the micromirror device A1........................81

Figure 5.24: The parallel displacement of the micromirror device A1 due to Lorentz force only. 82

Figure A.1: The mechanical equilibrium of the micromirror device A1 94

Figure B.1: Example of static deflection on micromirror device A1..........................100

Figure B.2: Example of static deflection on micromirror device A2..........................101

Figure B.3: Example of static deflection on micromirror device C (continued). 102

Figure B.4: Example of static deflection on micromirror device B............................102

Reproduced with permission of the copyright owner. Further reproduction prohibited without permission.

Figure B.4: Example of static deflection on micromirror device B (continued). 103

Figure B.5: Example of static deflection on micromirror device D............................103

Figure B.5: Example of static deflection on micromirror device D (continued). 104

Reproduced with permission of the copyright owner. Further reproduction prohibited without permission.

Chapter 1

Introduction

1.1 CMOS Micromachining

Micromachining, or Microelectromechanical systems (MEMS) as it is referred to in North America and Microsystems Technology (MST) in Europe and Japan, represents a new class of systems that is the integration of mechanical and/or optical elements, sensors, actuators, and electronics on a common silicon substrate through the utilization of micro-fabrication technology. The dimensions of MEMS devices are typically in the millimetric to micrometric range. Compared to macro-size counterparts, MEMS devices have many advantages, such as lower weight, faster response, less energy consumption and lower manufacturing cost.

Traditionally, micromachining can be divided into two categories: bulk micromachining and surface micromachining [1]. Bulk micromachining is usually performed by selectively etching crystalline silicon [2]. The mechanical structures developed with bulk micromachining are made of ether crystalline silicon or thin films deposited or grown on silicon. Surface micromachining, on the other hand, refers to the construction of devices completely by deposition and etching of thin films on the surface of substrate [3,4,5].

Although most micromachining fabrication technologies are borrowed from the microelectronics industry, the standard integrated circuits (IC) processes have not been

Reproduced with permission of the copyright owner. Further reproduction prohibited without permission.

directly used for building MEMS structures until Parameswaran, from the University of Alberta, initiated a new approach, CMOS (Complementary Metal Oxide Silicon) micromachining, in 1988 [6,7,8]. This approach utilizes the standard CMOS IC fabrication processes and adds post-processing etching steps to obtain MEMS structures. The post processing can be accomplished through either surface or bulk micromachining. Devices fabricated by CMOS micromachining are inexpensive, reliable, and easily integrated with electronic components.

Standard commercialized CMOS IC processes can be accessed by universities in Canada through the Canadian Microelectronics Corporation (CMC).

CMOS micromachining has become a simple yet powerful approach. Over the past decade, several CMOS micromachined devices such as thermal radiation sensors [9,10], gas pressure sensors [11, 12] and microresonators [13, 14] have been developed and extensively tested.

1.2 Optical MEMS Switching

In recent years, micromachining technology research and applications have grown rapidly in a wide range of industries including optoelectronics, transportation, aerospace, robotics, chemical analysis systems, biotechnologies and biomedical engineering.

The incorporation of micromechanical structures into fiber-optic systems holds promise of reducing costs and providing new opportunities for systems applications. Small optical MEMS (also known as oMEMS or MOEMS) switches are gradually replacing traditional opto-electronic-opto (OEO) switches to protect network equipment at the optical domain level. Furthermore, MOEMS switching subsystems may ultimately play an important role as a technology platform for reconfigurable add/drop multiplexers, all-optical cross-connects, and tunable lasers and filters.

Reproduced with permission of the copyright owner. Further reproduction prohibited without permission.

MOEMS switches normally contain one or more controllable moving parts, which can be actuated based on different physical phenomena [15], such as:

- Electrostatic [16]: MEMS switches using electrostatically deflectable micromirrors are presented in articles. These micromirrors can be arrays of simple cantilever beams, torsion beams or circular membranes.
- Thermal [17]: New bistable moving-fiber switches have been developed based on the thermal expansion and bimetal effect.
- Piezoelectric [18]: By using a piezoelectrically driven short focal length microlens or a microprism structure, optical switching can be achieved.

Several companies have developed commercialized MOEMS switching systems [19, 20, 21,22]. However, most present designs require special complex fabrication processes in order to be manufactured.

1.3 Thesis Overview

The following thesis presents the findings and conclusions obtained from investigating the characteristics of the static deflection and resonant vibration features of magnetically actuated micro-mirror devices. This work is essentially intended as a precursor to the study of micro-mirrors as the principal devices in optical switches, optical interferometers, or magnetic sensors.

The micro-mirror devices are based on magnetic actuation, produced by Lorentz forces, the product of an interaction of electric current with an external static magnetic field. Compared with thermal and piezoelectric methods, magnetically actuated devices have shorter response time, because magnetic force appears simultaneously with the presence of the electrical current. Another advantage of this method is that the movement direction

Reproduced with permission of the copyright owner. Further reproduction prohibited without permission.

of micromirrors can be easily controlled by changing the directions of currents through the driving wires.

CMOS Micromachining is the main fabrication scheme for all devices discussed in this thesis. Several different micromirror structures have been fabricated using CMOS processes offered by Mitel through CMC.

Chapter 2 describes the structure design, fabrication, and post-processing of micro-mirror devices.

Chapter 3 discusses the theoretical calculation concerning the static and dynamic characteristics of a basic structure of micromirror devices. Simulations using numerical methods are presented in the Chapter4. ANSYS, a commercial Finite Element Analysis software package is used for simulating the static deflection and resonant vibration of micromirror devices.

Experimental procedures utilized in this thesis work are demonstrated in Chapter 5, as well as the analysis of the experimental result data. This chapter also compares experimental findings with the results obtained from theoretical estimation and ANSYS simulation mentioned in Chapter 3 and Chapter 4.

Finally, Chapter 6 presents conclusions and an outlook for future research work.

Reproduced with permission of the copyright owner. Further reproduction prohibited without permission.

Chapter 2

Design and Fabrication of Micromirror Devices

This chapter describes structure design, fabrication and post-processing of magnetically actuated micro-mirror devices.

2.1 The Micro-mirror Structures

The micromirror device investigated in this project comprised of a platform suspended over a trench by two or four support arms, which are fixed to the surrounding substrate at their ends. All support arms are about 20 μm wide and consist of several layers of silicon dioxide, aluminum traces and silicon nitride (in the passivation layer). In the central platform, an electrically isolated metal layer is deposited to serve as a mirror for reflecting the laser beam.

The geometry of the simplest design (Unit A1) is illustrated in Figures 2.1. In this device, the size of the central platform is 325 μm by 320 μm, while the length of each straight arm is 200 μm. Two aluminum traces, parallel distributed on the opposite edges of the platform, are deposited on different metal layers (separated by a CVD oxide layer). The details about the fabrication process will be discussed in later sections.

In order to determine optimum arm/platform structure, several devices with different geometry of support arms or platforms have been designed and fabricated, as shown in Figure 2.2. Among them, the second micro-mirror design (Unit A2) is very similar to the

Reproduced with permission of the copyright owner. Further reproduction prohibited without permission.

simplest design (Unit A1); however the shapes of support arms are more complicated. The design of device Unit C has four zigzag-shape support arms. In designs of Unit B and Unit D, each platform has four straight aluminum traces, which make it possible for angular deflection about two axes. A microphotograph and schematics of Unit D can be found in Figure 2.3. Circular micromirror platforms with circular current traces are designed in Unit E and Unit F.

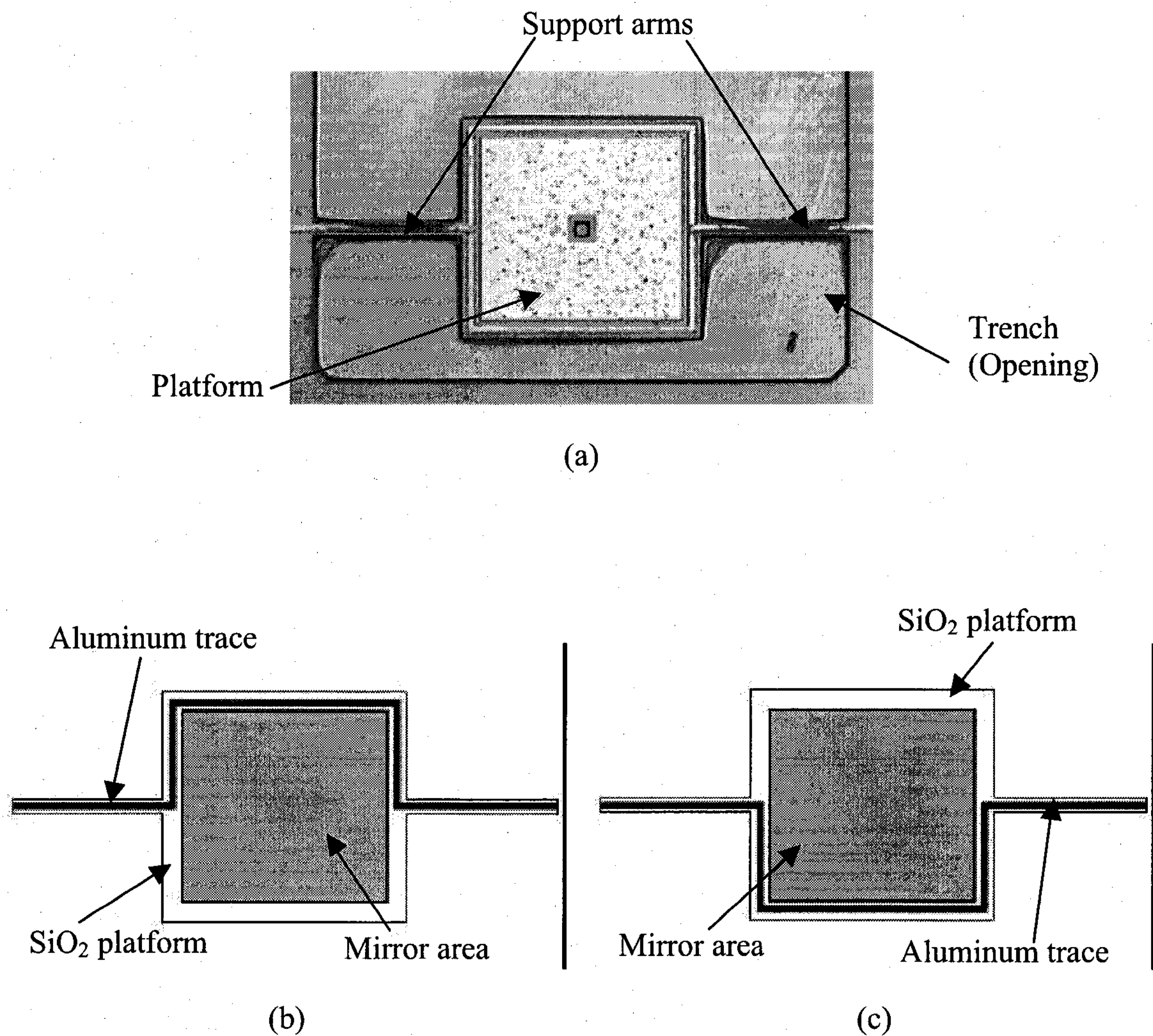

Figure2.1: (a) Photograph of an unetched micromirror device (Unit A1); (b) Metal I layer distribution: top edge on device Unit A1; (b) Metal II layer distribution: bottom edge on device Unit A1.

Reproduced with permission of the copyright owner. Further reproduction prohibited without permission.

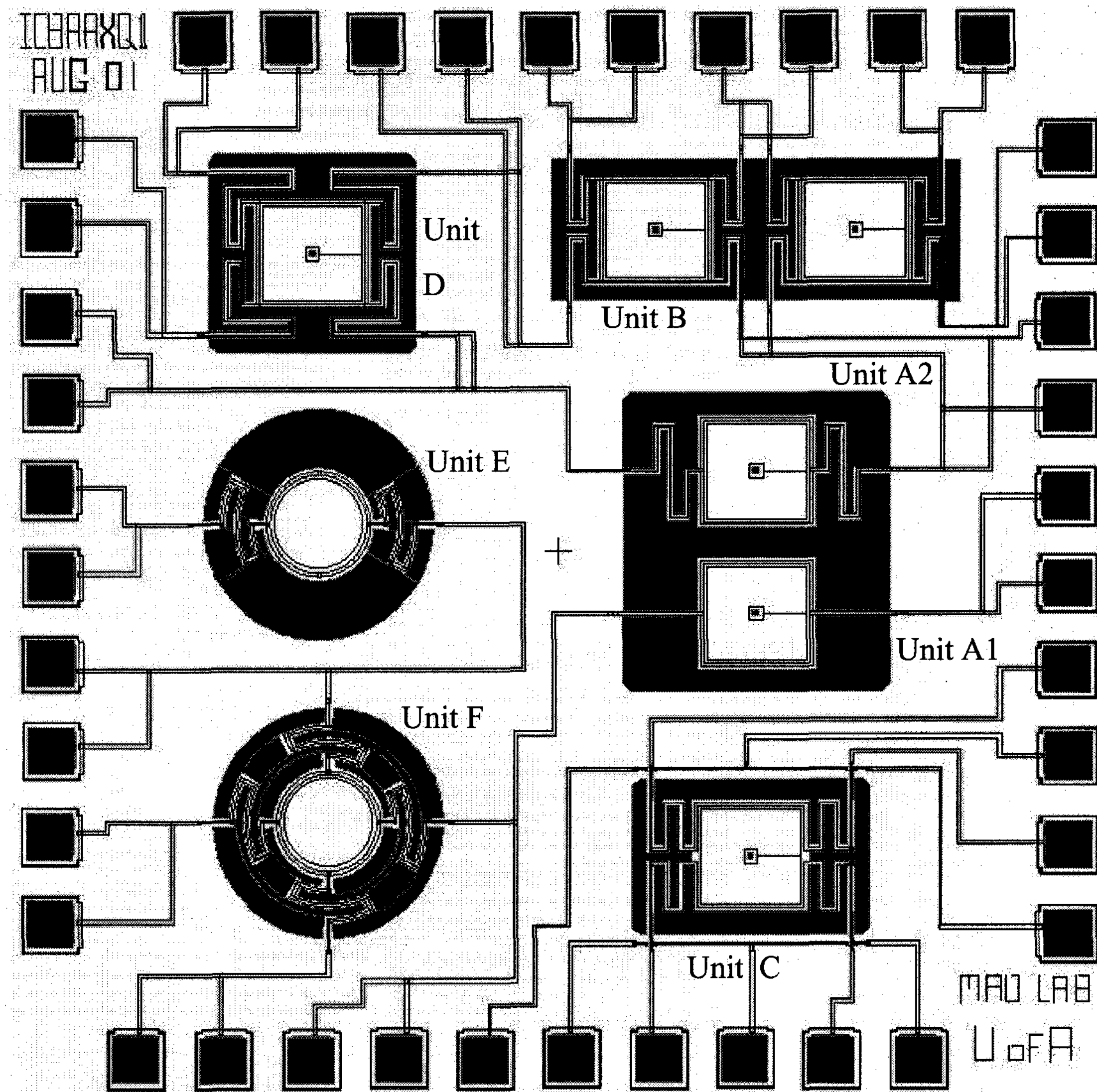

Figure 2.2: Different designs of micromirror devices on one chip

Reproduced with permission of the copyright owner. Further reproduction prohibited without permission.

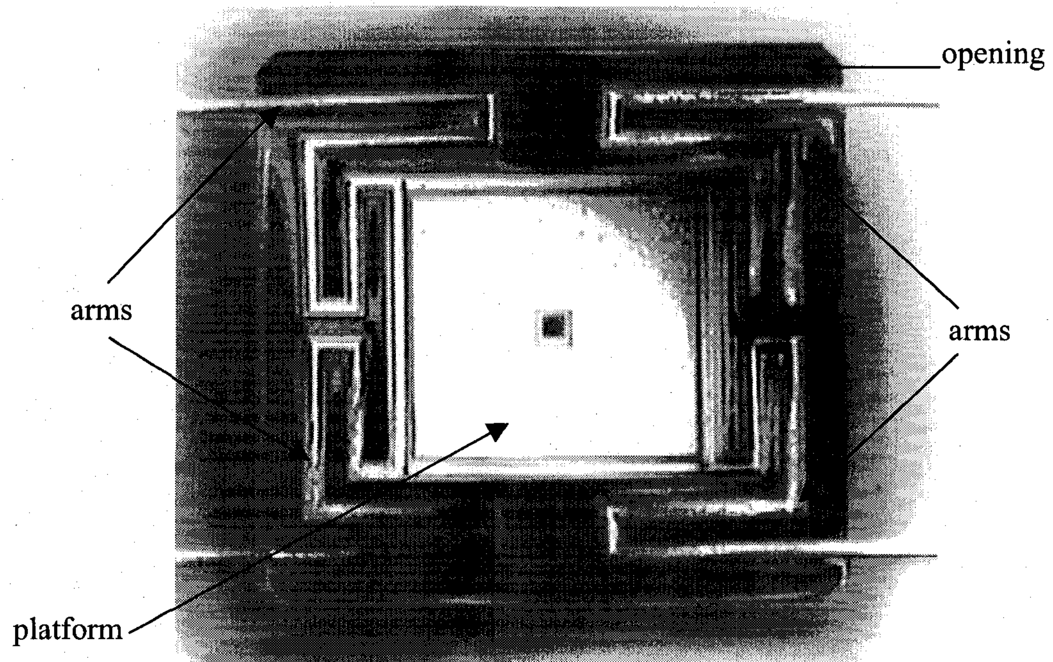

(a)

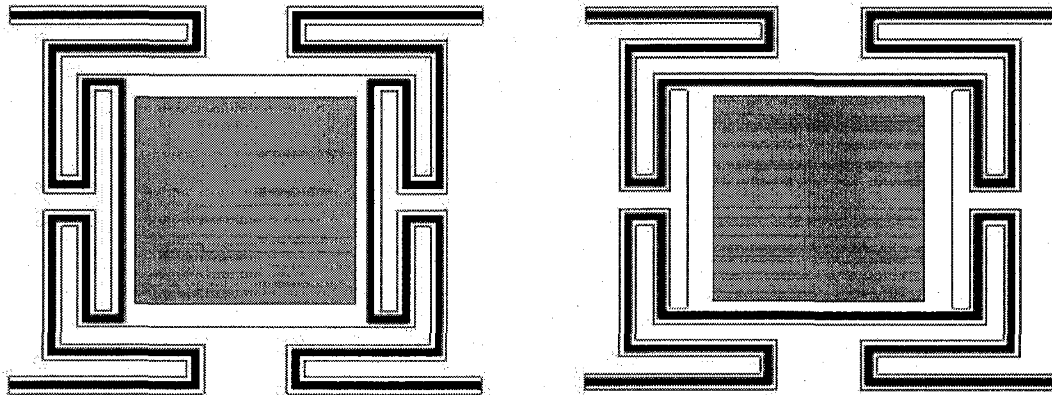

(b) (c)

Figure 2.3: (a) Photograph of an etched micromirror device (Unit D); (b) Metal II layer distribution: left and right traces on device Unit D; (c) Metal I layer distribution: top and bottom traces on device Unit D.

Reproduced with permission of the copyright owner. Further reproduction prohibited without permission.

2.2 Design Flow for CMOS Micromachined Micromirrors

CMOS micromachining, or fabrication of a three-dimensional MEMS device using a standard CMOS IC process, involves the deposition, doping and patterning of the desired material, layer by layer, and finally the selective etching of the underlying support. The thickness of each layer and other parameters are determined by the CMOS manufacturer. The task of a 3-D MEMS device design, therefore, is accomplished by designing series of 2-D masks. The design process of micromirror structures is introduced in this section.

MEMS-pro L-Edit, an IC design package developed by MEMSCAP Inc., is used to lay out the structure layer by layer, shown as follows:

1) Firstly, the ***Active Area*** is drawn to define the area where field oxide will not be grown. It actually provides the basic shape of the silicon etching opening, as shown in Figure 2.4(a).

2) Second, a ***Contact Cut*** layer is introduced to define the contact cut region. Additionally, the Contact Cut layer is also used to expose the silicon substrate by overlapping on the Active Area layer, as shown in Figure 2.4(b).

3) The third layer is ***Metal 1***, which forms part of the aluminum traces on the arms and the platform, as shown in Figure 2.4(c).

4) The ***Via*** is normally used to connect two metal layers. In the design of MEMS devices, the ***Via*** layer should be also applied to overlap the Active Area for the post-processing of silicon etching, as shown in Figure 2.4(d).

5) The remainder of the aluminum traces and the mirror plate are defined in the ***Metal 2*** layer, as shown in Figure 2.4(e).

6) In a CMOS process with triple or more metal layers, more Metal and Via layers are also added to the design process.

7) The last layer is the ***Passivation*** layer. It overlaps the Active Area, Contact Cut layer, and the Via layer to avoid silicon dioxide and nitride deposition, as shown in Figure 2.4(f).

Reproduced with permission of the copyright owner. Further reproduction prohibited without permission.

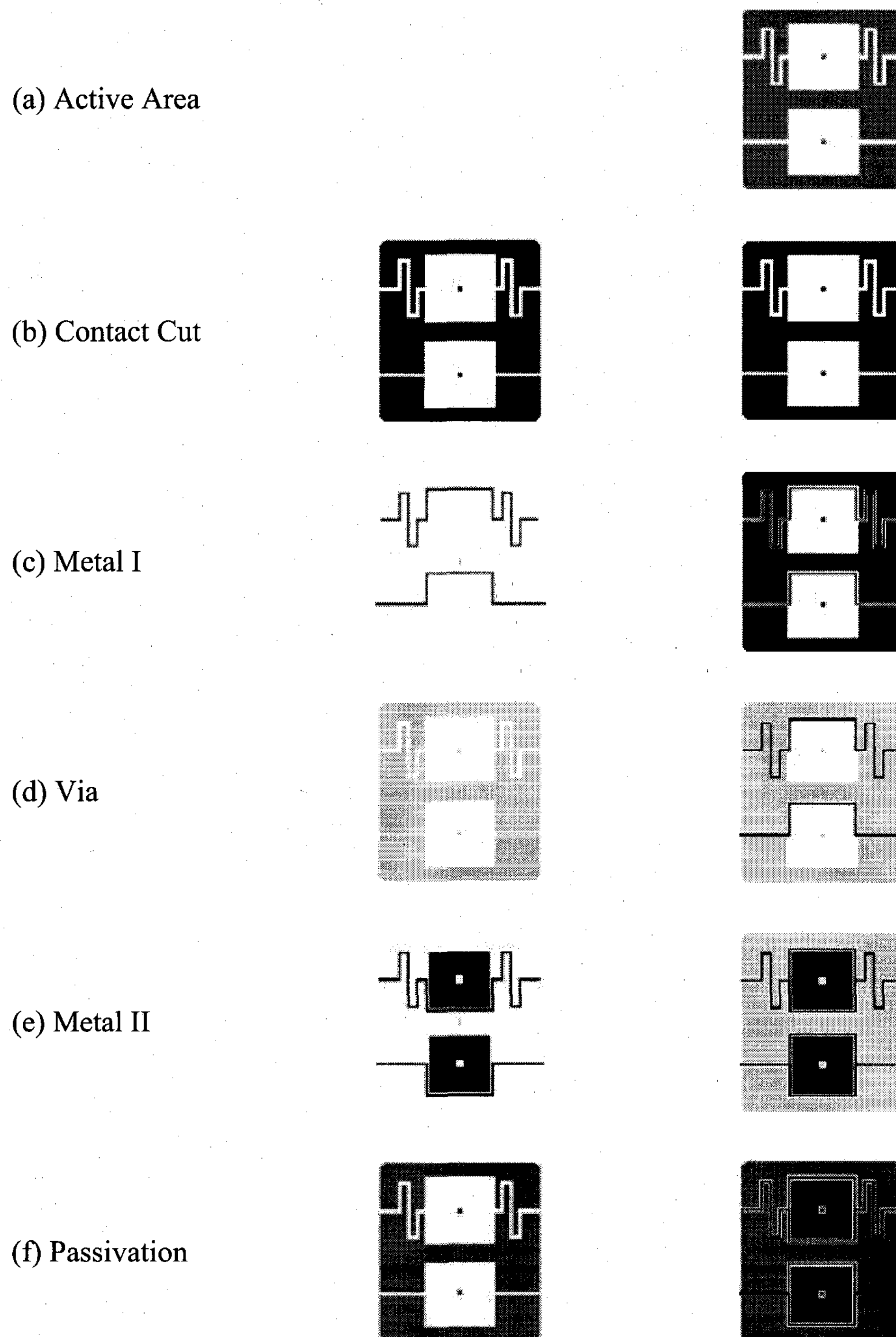

Figure 2.4: Layout design flow for CMOS micromachined micromirror devices

Reproduced with permission of the copyright owner. Further reproduction prohibited without permission.

2.3 Fabrication of Micromirror Devices

In this project, layout data containing all mask designs for micromirror devices, electrical circuits and pads on one chip are submitted to the Canadian Microelectronics Corporation (CMC) in GDSII format. Micromirror devices were fabricated using the Mitel 1.5 micron CMOS technology through CMC.

According to the datasheet from Mitel, a typical fabrication process for building a micromirror device may include the following steps. The schematic cross section is shown in Figure 2.5.

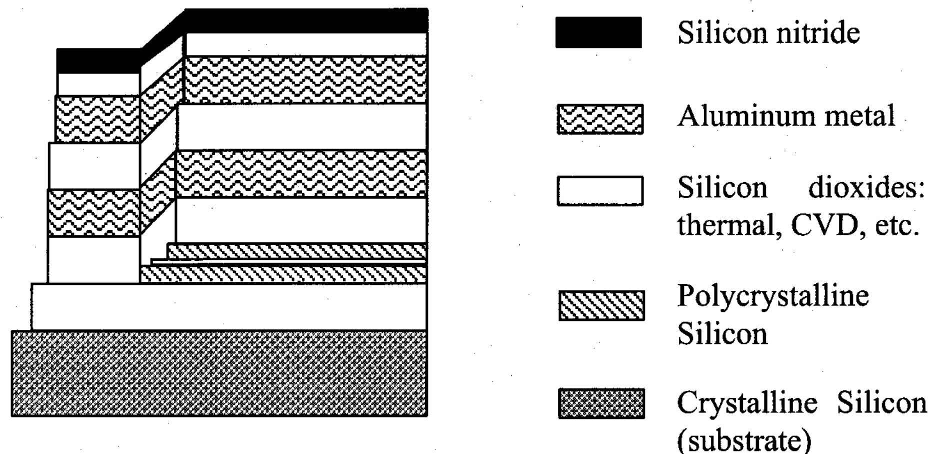

Figure 2.5 The schematic cross section of a typical CMOS micromaching fabrication

- The Mitel 1.5 micron process is a p-well-based process starting with an n-type wafer.
- A 0.9 μm field oxide layer is generated after initial oxidation and p-well diffusion. This layer may be used as structure material as well as a dielectric layer, which electrically isolates the polysilicon structure from the crystalline substrate.
- After the field oxidation and gate oxidation (about 0.027 μm, not shown in Figure 2.5), two layers of low-stress doped polysilicon (about 0.32 μm and 0.25 μm thick, respectively) may be deposited with a 0.02 μm oxide layer between.
- Then a 0.8 μm dielectric layer mainly composed of phosphosilicate glass (PSG) is

Reproduced with permission of the copyright owner. Further reproduction prohibited without permission.

deposited.

- Two 0.8 μm patterned aluminum layers are used to form electrical connections. There is a 1.0 μm inter-dielectric oxide layer between two metal layers.
- Finally, a passivation layer comprising 0.5 μm oxide and 0.5 μm nitride layer is deposited.

2.4 Post-processing

Several procedures have been involved in the post-processing of CMOS micromachined devices, such as electrical continuity test, dice mount, wire bonding and silicon etching. Among them, silicon etching is an essentially critical step, because only after silicon etching can the micromirror platforms be released from substrates.

Figure 2.6 shows two types of etching: isotropic and anisotropic. In our Lab, we use gas-phase XeF_2 (xenon difluoride) for silicon isotropic etching, while TMAH (tetra-methyl ammonium hydroxide) solution is used for silicon anisotropic etching.

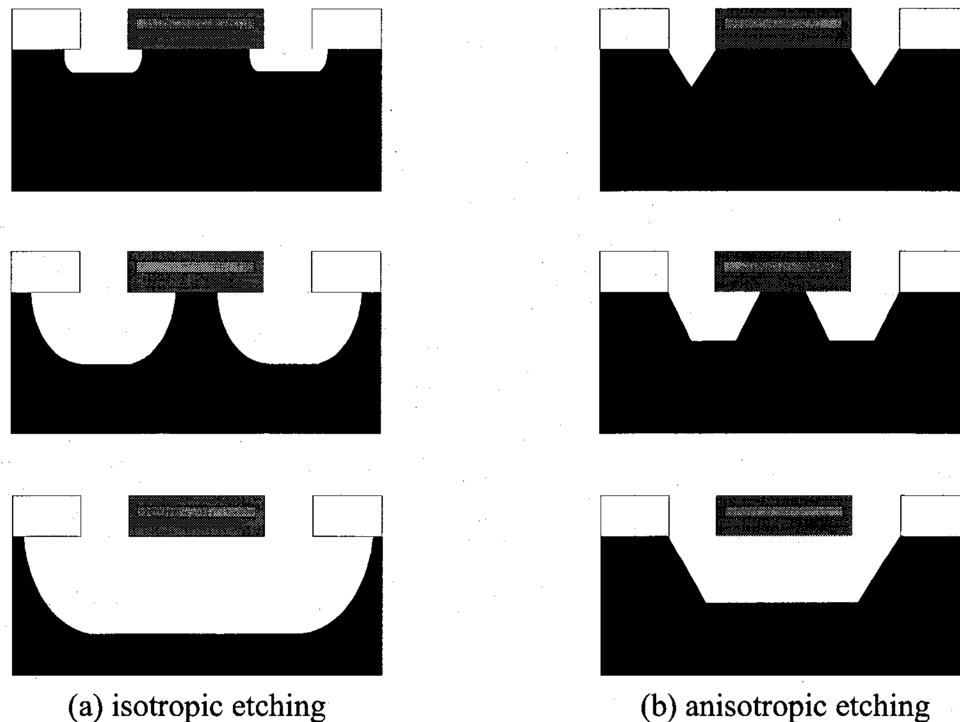

(a) isotropic etching (b) anisotropic etching

Figure 2.6: Schematic cross-sectional view of two types of silicon etching

Reproduced with permission of the copyright owner. Further reproduction prohibited without permission.

2.4.1 XeF_2 isotropic silicon etching

XeF_2 is in granular crystalline form at standard room conditions; however, the crystals sublimate into a vapor when the environment pressure is less than its equilibrium vapor pressure, approximately 600 Pa (4.5 Torr). The reaction between XeF_2 and silicon occurs through a sequence of steps. Gaseous XeF_2 is first absorbed on the silicon and then reacts to form a thick layer of fluorosilyl consisting of SiF, SiF_3, and SiF_4. The fluorosilyl product desorbs into the gas phase. The principal gas-phase product has been determined to be SiF_4, which is volatile at room temperature. The reaction equation for XeF_2 and silicon is approximately given by

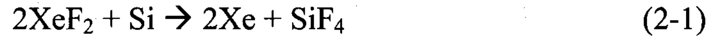

$$2XeF_2 + Si \rightarrow 2Xe + SiF_4 \qquad (2\text{-}1)$$

Figure 2.7 shows the main parts of the XeF_2 etching system, which primarily consists of three chambers and computer-controlled flow valves between chambers. The system also contains a pump and other mechanical components, a Zeolite trap, and a nitrogen gas source.

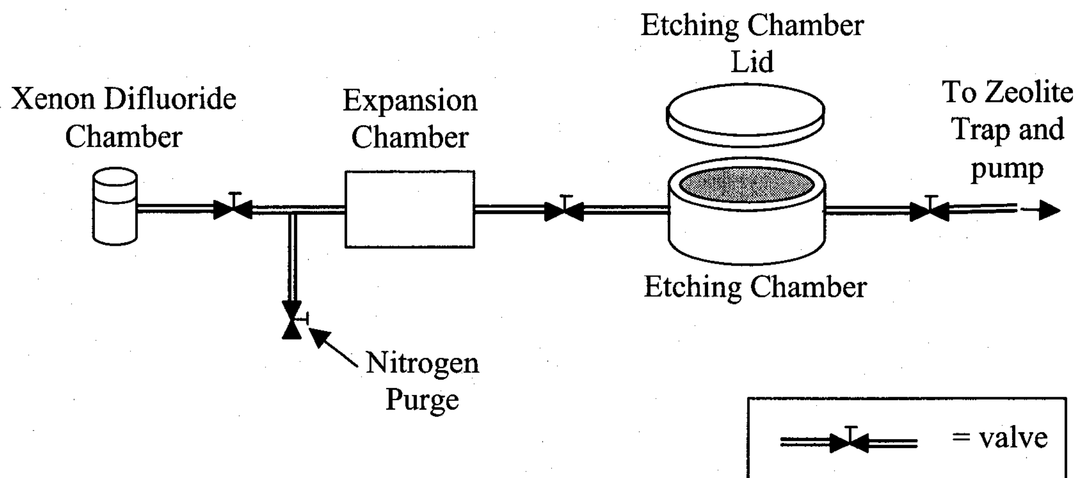

Figure 2.7: XeF_2 etching system schematic

Firstly, etching samples are placed in the etching chamber and the chamber lid is held in place under vacuum. After pumping the chambers and system lines, vacuum conditions

Reproduced with permission of the copyright owner. Further reproduction prohibited without permission.

within the system are created (approximately 50 mTorr). The system is then purged via nitrogen gas to clean extraneous gases and water vapour. Once the system has been purged, the XeF_2 gas is allowed to expand into the expansion chamber for about one minute; and then, the gas is passed into the etching chamber where the etching occurs for approximately another minute; the gas is finally pumped from the etching chamber. The three steps mentioned above are collectively named an etch pulse. A MEMS device may need several etch pulses to fully release structures. After each four etch pulses, the etching system is purged again with nitrogen.

XeF_2 provides high selectivity for aluminum, silicon dioxide, and photoresist. For instance, the etch speed ratio of $Si:SiO_2$ is more than 1000:1. The etching achieves a relatively high rate (>1 μm/min). It is a dry process, requiring no washing or drying steps. The reaction products are in a gaseous phase and do not remain on the surface. The isotropic characteristic allows for undercutting of large structures. These properties make XeF_2 very useful for CMOS post processing, especially when etching pre-packaged and bonded substrates.

The test chips discussed in later chapters were etched in XeF_2. Release of the structures required approximately 15 etch pulses.

The main problem of XeF_2 etching is undercutting; that is, the silicon substrate around the opening area is etched away because XeF_2 etching is isotropic. Undercutting also occurs at sidewalls of die, where bare silicon is exposed to the XeF_2 during the etching process. Undercutting increases the fragility of devices and leads to cracking and breakage, due to the inherent stress between the deposition layers and if the devices are not handled with extreme care, shown as in Figure 2.8.

In the Figure 2.8, the colour variation across the mirror platform and arms suggests that the platform and arms are curved after etching. This is a result of strain inside the laminated oxide and metal layers [23]. To alleviate this problem, it may be necessary to develop the post-processing steps required to deposit a strain compensation layer.

Reproduced with permission of the copyright owner. Further reproduction prohibited without permission.

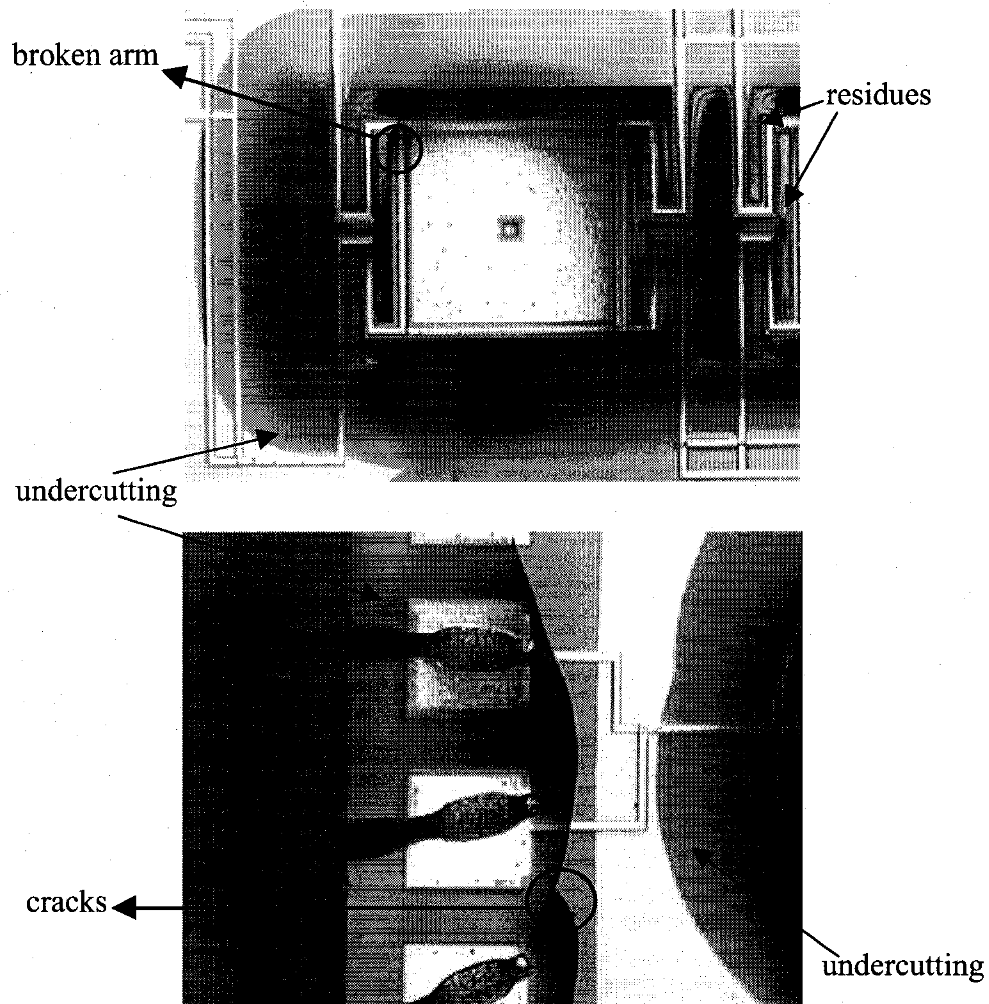

Figure 2.8: Undercutting, cracking and breakage on XeF_2 etched chips

2.4.2 TMAH anisotropic silicon etching

In anisotropic etching, silicon is selectively removed at a rate which depends on the orientation of the crystal lattice structure.

Potassium hydroxide (KOH), ethylene diamine pyrocatechol (EDP), and tetramethyl ammonium hydroxide (TMAH) are commonly used as anisotropic etchants. These

Reproduced with permission of the copyright owner. Further reproduction prohibited without permission.

etchants all have high silicon etch rate and anisotropy. However, KOH is not CMOS compatible because it attacks aluminum and SiO_2 and contaminates the gate oxides with mobile alkali metal ions. As for EDP, it is difficult to use because it is toxic and is even suspected to be carcinogenic. TMAH is an attractive alternative as it is relatively safe to work with and has very high selectivity for silicon dioxide.

The effects of TMAH concentration, temperature and the silicon (or silicic acid) doping of the etchant with TMAH have been studied previously: [24, 25]

- As reported, with an increase of the concentration of the TMAH in solution, there was a decrease in the etching rate. But at the lower concentration, the etched surface became extremely rough. At approximately 20wt% TMAH, the etched surface became quite smooth.

- The higher the temperature, the faster the etch rate. However this temperature must be carefully controlled because the boiling point of TMAH solution is about 98~100°C.

- The main problem with TMAH etching is that TMAH attacks aluminum pads, and makes electrical connection impossible. Some reports proposed that dissolved silicon or silicic acid in the TMAH would protect the Al by decreasing the pH.

Fig.2.9 shows the TMAH anisotropic silicon etching system, which consists of a hotplate with an oil bath, a magnetic stirring bar, a beaker containing the etchant placed in the oil, a thermometer, nitrogen gas bubbler, and a reflux condenser to minimize the loss of water. The system is placed inside a fume hood.

Reproduced with permission of the copyright owner. Further reproduction prohibited without permission.

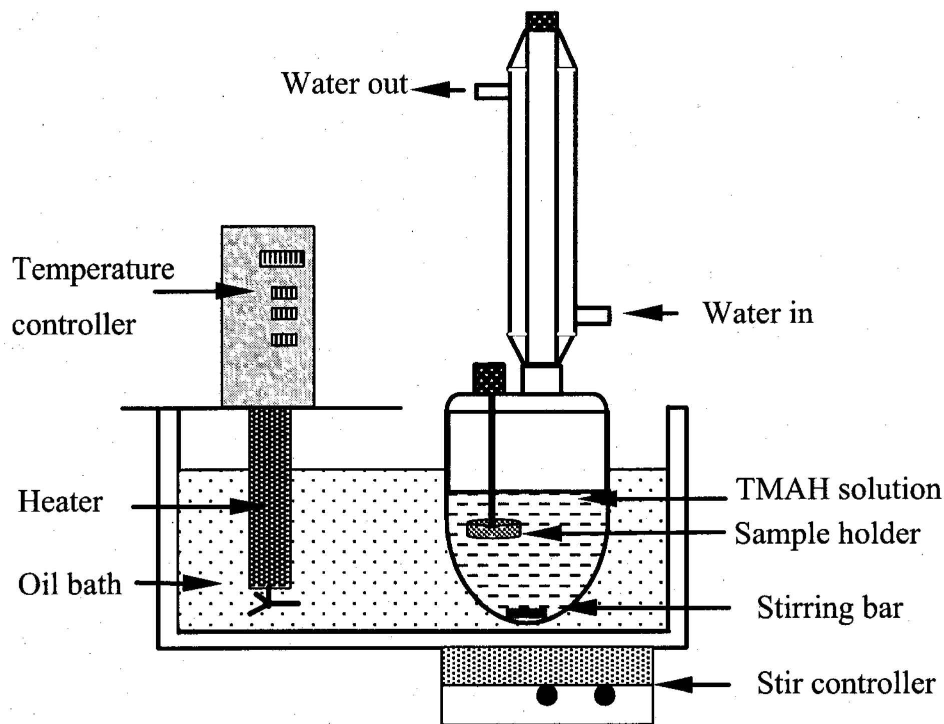

Figure 2.9 TMAH silicon etching system

The recipe of the TMAH solution used for anisotropic silicon etching is from the NanoFab, University of Alberta. Key points of this recipe are:

- 250 ml TMAH (25%);
- 375 ml deionized (DI) water;
- 22 g silicon dust dissolved into solution;
- use at 90°C.

By this recipe, the concentration is 10 wt.% TMAH with 3.4 wt.% dissolved silicon. The etch rate is about 1 μm/min.

A silicon surface exposed to the air immediately grows a thin oxide layer, called the native or natural oxide layer. For XeF_2 etching, in most cases, stripping of the native oxide layer is not necessary, and the chips are readily etched. However, the native oxide layer will inhibit TMAH etching. Therefore, a short-time XeF_2 etching or buffered oxide etch (BOE) dipping step is required before TMAH etching.

Reproduced with permission of the copyright owner. Further reproduction prohibited without permission.

Table (2-1) shows three procedure sequences of TMAH etching experiments. In the experiment using process sequence 1, samples were firstly etched by XeF_2 for only one pulse, and then dipped in BOE (10:1) solution for 30 seconds. After 2 hours TMAH etching, devices kept good structures and no pad was attacked by TMAH. BOE dipping step was skipped in the experiment of process sequence 2, while the samples were etched in XeF_2 for 3 pulses and then they were immediately put into TMAH etching system. The MEMS structures were totally released from substrate after 2 hours TMAH etching, but two out of 40 pads were found slightly damaged by the TMAH solution. In the experiment of process sequence 3, samples were dipped in BOE (10:1) solution for 60 seconds to remove the native oxide layer, and then etched by TMAH for 3 hours. All of the devices were released completely and also kept good structures. The pad surface has not been attacked. Compared with other two experiments, we preferred sequence 3 as a standard process arrangement, because even after XeF_2 etching, fresh silicon surface can be oxidized by air if we don't process TMAH etching in a short time after XeF_2 etching.

Table (2-1) Process sequences of TMAH etching

No.	Process sequence
1	1) The samples (CMOS devices) were etched by XeF_2 for 1 pulse; 2) Dipping the samples into the BOE (10:1) solution for 30 seconds; 3) TMAH etching for 2 hours.
2	1) The samples were etched by XeF_2 for 3 pulses; 2) TMAH etching for 2 hours.
3	1) Dipping the samples into the BOE (10:1) solution for 45~60 seconds; 2) TMAH etching for 3 hours

Reproduced with permission of the copyright owner. Further reproduction prohibited without permission.

A big problem with TMAH etching is its poor reproducibility. We did some successful experiments of TMAH etching work, but many experiments failed even following the same process procedures. The main reason is that the concentration of silicon doping in the TMAH solution is quite difficult to maintain.

On the one hand, excess TMAH, only a little beyond that needed to neutralize the Si, resulted in significant attack on the aluminum bonding pads. But there are two main problems with silicon dissolving process. First, it takes a very long time to dissolve silicon dust into TMAH solution. Second, if the solution containing dissolved silicon is cooled, white precipitate form and the solution is cloudy, which means that the concentration of silicon doping changed again.

On the other hand, insufficient TMAH caused premature termination of etching or failures of the etchant to even start removing silicon. In our experiments, the TMAH is used up very quickly, even only after a few times of etching.

2.4.3 The problem of residues

It was found there are some residues left behind in the corners and along the edges of the Active areas on the chips fabricated by Mitel Corporation's 1.5 μm process. Under optical inspection, two distinct types of residue are visible. A fairly common layer of residue appears clear or light gray, and is likely an oxide of some sort. As for the second layer of residue, it is seen as tiny dabs of bright metallic residue in the tightest corners and smallest open areas, particularly near the edges of Metal I and Metal II regions. Because these residues actually decrease the size of opening area, it takes more time to release the MEMS structures completely. Furthermore, residues may vary the dimensions and material properties of devices, and finally affect the mechanical characteristics.

The reason for residue generation is probably due to imperfect alignment of mask layers. As described in section 2.2, open silicon areas were defined by stacking four layers (Active area, Contact area, Via and Passivation layer) directly on top of each other.

Reproduced with permission of the copyright owner. Further reproduction prohibited without permission.

Although this method is common for MEMS designs, it breaking standard design rules of CMOS fabrication.

From the results of our experiments, the residues could be removed by chemical or mechanical methods:

- We found that part of residues disappeared after TMAH etching, shown as Figure 2.10. The critical step for residue removal in the TMAH etching process is BOE dipping, which is originally to remove native oxide layer on the opening area. This also confirms that part of residue is silicon dioxide. Although increasing BOE etching time may remove more residues, the BOE will also attack the SiO2 platform and arms, and result in improper geometries on the devices.
- Laser material removal could be a good mechanical method to strip residues. The Laser Plasma Interaction Group, ECE department in University of Alberta, has set up a laser ablation system using high-power ultra-short laser pulses. The ablation rate and the size of laser spot should be adjusted extremely carefully, because MEMS devices are very fragile, and easily to be damaged.

Reproduced with permission of the copyright owner. Further reproduction prohibited without permission.

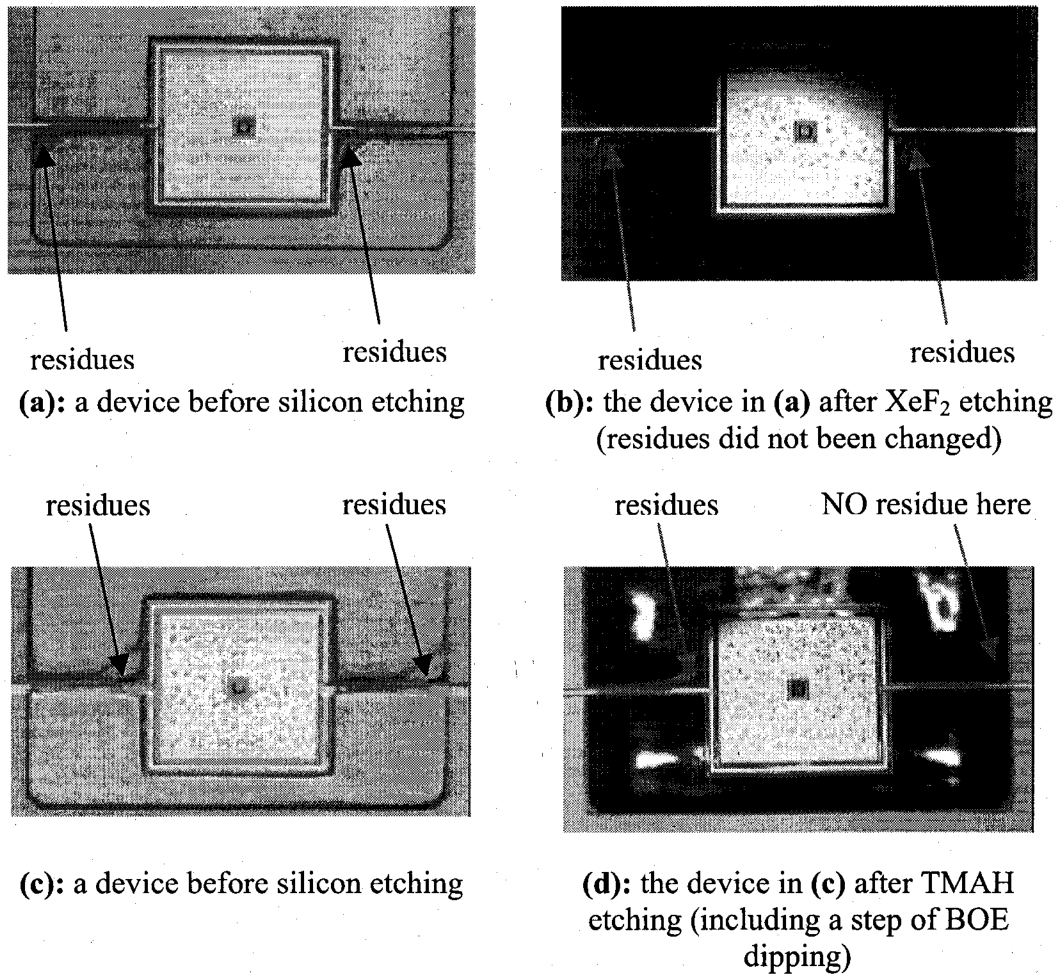

(a): a device before silicon etching

(b): the device in **(a)** after XeF_2 etching (residues did not been changed)

(c): a device before silicon etching

(d): the device in **(c)** after TMAH etching (including a step of BOE dipping)

Figure 2.10: residues after different etching procedures

The final yield of functional devices was very low. The main problem resulted from the chip fabrication. About 80% of aluminum traces on the Metal II layer have electrical connection problems even before post-processing. Thus, most devices cannot work in the mode as the original designs. Other problems concerning yield issue include the residue problem from fabrication, as well as mistakes in post-processing and chip design. As mentioned before, some common MEMS design methods actually violate the design rules of CMOS technologies badly. A few improvements of the design rule violations are discussed in the last chapter.

Reproduced with permission of the copyright owner. Further reproduction prohibited without permission.

Chapter 3

Analytical Estimation

After a brief introduction to actuation methods of the micro-mirror devices, this chapter discusses the analytical calculation concerning the static and dynamic characterizations of devices.

3.1 Actuation Modes

As demonstrated in the previous chapter, a micromirror device consists of a platform suspended over a trench by two or four support arms, which are fixed to the surrounding substrate at each ends. Actuation of the micromirror devices is produced by Lorentz forces resulting from the interaction between an external magnetic field and the currents flowing through the aluminum traces on the platform. The Lorentz force is governed by the following equation:

$$\vec{F} = I_s \vec{L}_s \times \vec{B} \tag{3.1.1}$$

where the symbol I_s denotes the driving current, $\vec{L}_s$ is the length of a straight aluminum trace where the magnetic force acts and $\vec{B}$ indicates the external magnetic field. An example of the micromirror actuation is given in Figure 3.1, where an external magnetic field is applied in the plane of the substrate and perpendicular to the arms. The symbol ⊗ indicates the Lorentz force directed into the paper, and ⊙ indicates the Lorentz force

Reproduced with permission of the copyright owner. Further reproduction prohibited without permission.

directed out of the paper. In the region of Figure 3.1 where two metal lines are side-by-side, they actually overlap each other on the real devices but are electrically isolated, because they are deposited on the different layers and separated by an oxide layer.

As shown in Figure 3.2, when driving currents flow in opposite directions through two parallel aluminum traces on opposite edges of the platform, the Lorentz forces on the traces also have opposite direction, and the platform will tend to tilt due to the applied forces. On the other hand, when driving currents have the same direction, the platform will have experience a net force but no torque and tend to undergo a parallel displacement.

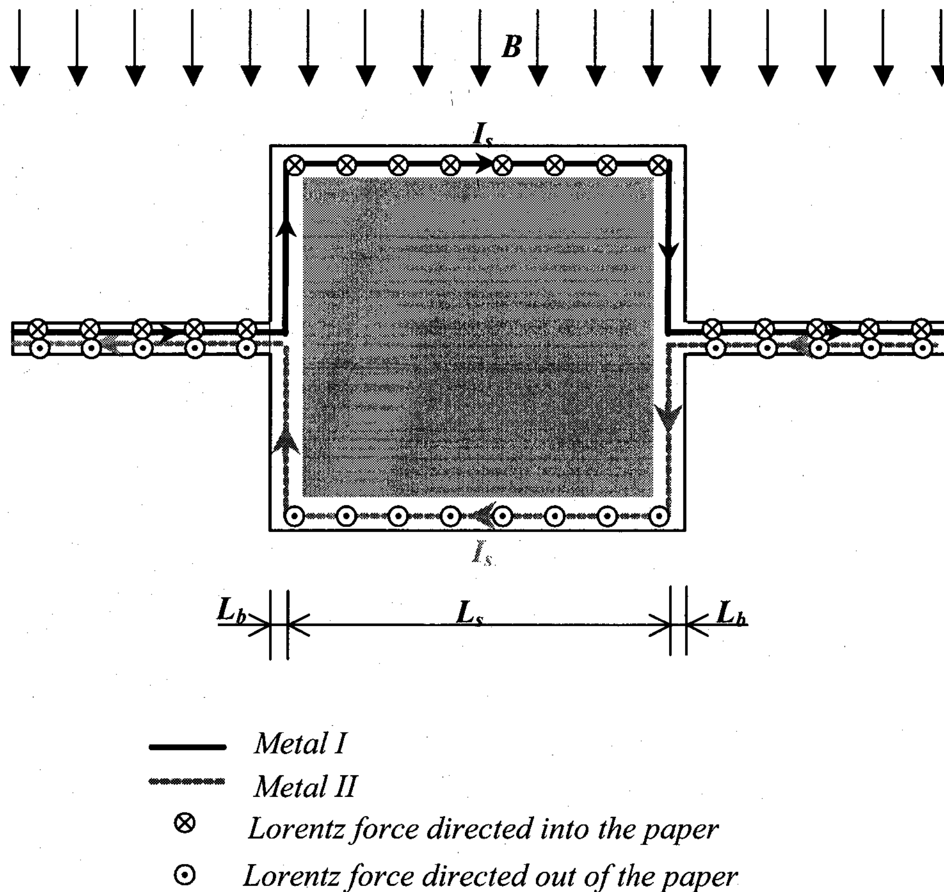

Figure 3.1: Magnetic actuation principle for micromirror structures

Reproduced with permission of the copyright owner. Further reproduction prohibited without permission.

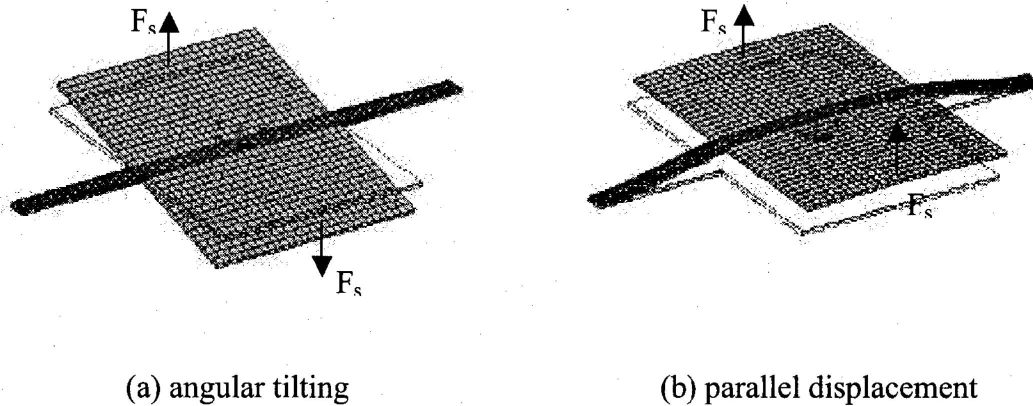

(a) angular tilting (b) parallel displacement

Figure 3.2: Two modes of platform movement

3.2 Theoretical Calculation

As shown in Figure 2.2, several micromirror devices with different supporting arm configurations have been designed. But most structures are too complicated for analytical calculation. This section presents the theoretical estimation for device A1, which is the simplest design of micro-mirror devices developed in this project. For other designs, simulations using finite element method will be introduced in the next chapter.

Micro-mirror devices investigated in this project were fabricated using the Mitel CMOS 1.5 μm process. The properties, such as Young's modulus, Poisson ratio, and density of the different CMOS-compatible materials are given in Table (3-1).

Figure 3.3(a) illustrates the cross section of a typical support arm with two metal layers embedded. All silicon dioxide layers, including the dielectric deposition, inter-dielectric, spin-on-glass and passivation oxide layer, are merged together.

Reproduced with permission of the copyright owner. Further reproduction prohibited without permission.

Due to the similar Young's modulus E between the silicon dioxide and the aluminum as indicated in Table (3-1), the silicon dioxide section of arms, containing aluminum traces, can be regarded as a homogenous material, as shown in Figure 3.3(b).

Table (3-1): Thickness and material properties of constitutive layers [26]

	Layer	Thickness	Young's Modulus (E) [GPa]	Poisson Ratio (ν)	Density [kg/m^3]
1	Passivation (nitride)	0.5 μm	380	0.24*	3100
2	Passivation (oxide)	0.5 μm	75	0.17	2200
3	Metallization II (Al)	0.8 μm	74.14	0.33*	2700*
4	Inter-dielectric & Spin-on-glass	1.0 μm	75	0.17	2200
5	Metallization I (Al)	0.8 μm	74.14	0.33*	2700*
6	Dielectric deposition (mainly PSG)	0.8 μm	75	0.17	2200
7	Field oxidation	0.7 μm	75	0.17	2200

notes:

- *Layer 1 is the uppermost layer. Values of the thickness of the layers were obtained from Mitel.*
- *Material properties marked with an asterisk denote the corresponding bulk material values, but the remainder of the values pertain to thin films.*

Reproduced with permission of the copyright owner. Further reproduction prohibited without permission.

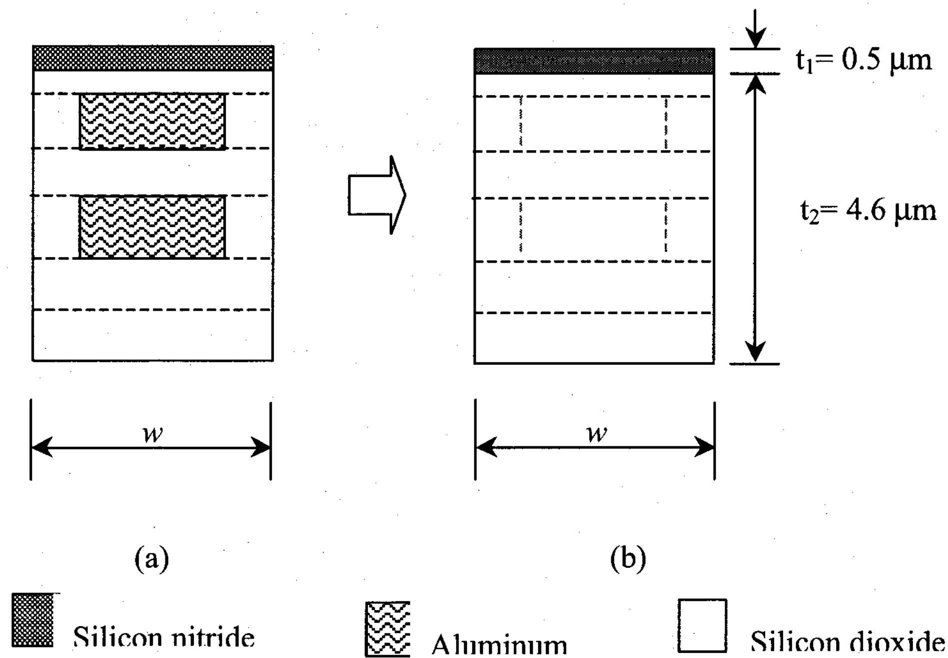

Figure 3.3: The cross-section of a support arm

The cross-section figure of the mirror platform is very similar to Figure 3.3(b), and only w (the width) has a different value. The width of support arms is 20 μm, while the width of the platform is 300 μm.

3.2.1 Static Modeling for Device A1

3.2.1.1 Static Deflection Mode I: angular deflection

Figure 3.4 shows the simplest micro-mirror device A1. In this figure, L_a denotes the length of support arm, and L_d indicates the distance between two parallel aluminum traces. L_s is the effective length of one driving trace, while B and I_s are the external magnetic field and driving current, respectively.

When driving currents have opposite directions in the two parallel aluminum traces on

Reproduced with permission of the copyright owner. Further reproduction prohibited without permission.

the platform, the Lorentz forces produce a platform tilt around the support arms. The arms are considered to be rigid at support A and D. Mechanical equilibrium is obtained when the mechanical restoring torque is equal to the magnetic torque.

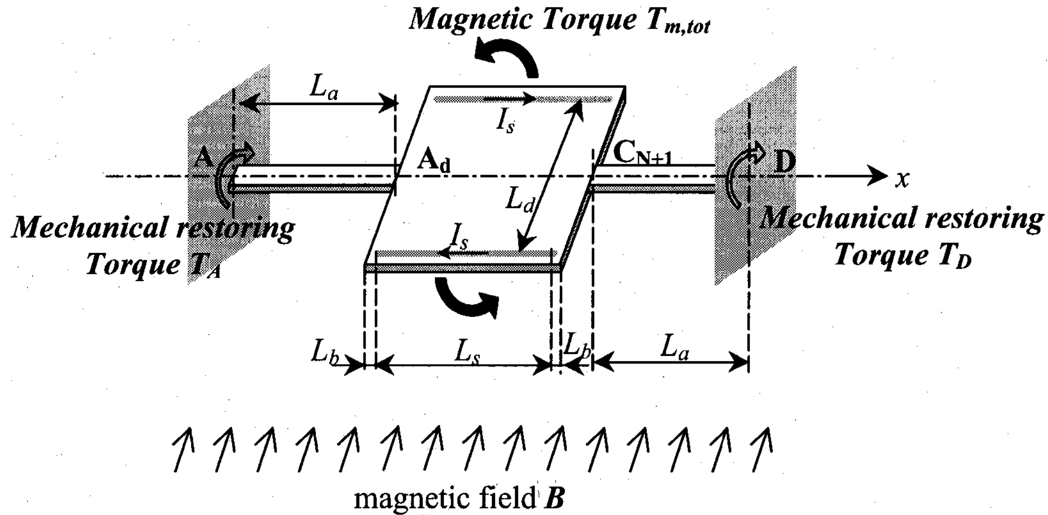

Figure 3.4: The mechanical equilibrium of the micromirror device A1

The torsional equation of equilibrium is

$$T_A + T_D = T_{m,tot} = 2(BL_sI_s)\frac{L_d}{2}\cos\theta = (BL_sI_s)L_d\cos\theta \approx (BL_sI_s)L_d \tag{3.2.1}$$

Here, θ is the rotation angle. In practice, θ is very small, then $\cos\theta\ (\approx 1)$ can be ignored. And the device is symmetric, then

$$T_A = T_D = \frac{T_{m,tot}}{2} \tag{3.2.2}$$

- ***Twist angles:***

For linear elastic materials, the rate of change of angular twist over the length L is formulated by [27]

Reproduced with permission of the copyright owner. Further reproduction prohibited without permission.

$$\frac{\Phi}{L} = \frac{T}{(GJ)} \tag{3.2.3}$$

J is a factor dependent on the form and dimensions of the cross section. For a circular section, *J* is the polar moment of inertia I_p; for other sections *J* is less than I_p and may be a very small fraction of *Ip*. *G* is the shear modulus of elasticity, and and for an isotropic material it is related to the Young's Modulus *E* and Poisson Ratio ν by the following equation:

$$G = \frac{E}{2(1+\nu)} \tag{3.2.4}$$

(GJ), known as the torsional rigidity, is determined by the cross section geometry and mechanical properties of the torsion beam. In this device, two arms are symmetric, therefore

$$(GJ)_{AA_d} = (GJ)_{C_{N+1}D} = (GJ)_a \tag{3.2.5}$$

Practically, the torsional rigidity of whole micromirror platform is not exactly the same, because the distribution of aluminum traces is not uniform, as illustrated in Figure 3.4. But the properties of aluminum and silicon dioxide are quite similar by the Table (3-1), thus we assume all segments of the platform have the same value of $(GJ)_b$.

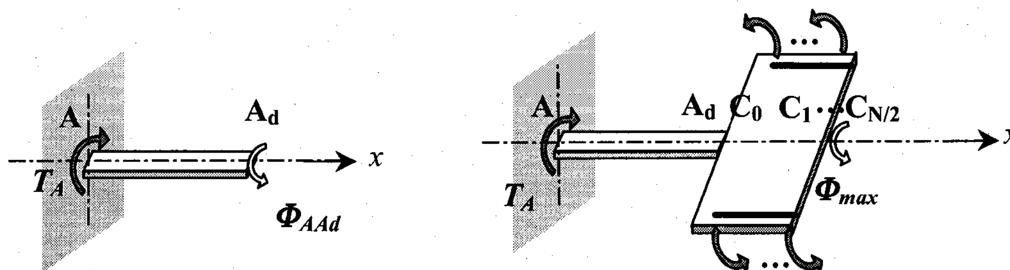

Figure 3.5: The rotation angles of the arm and the platform of device A1.

Reproduced with permission of the copyright owner. Further reproduction prohibited without permission.

Details of twist angle calculation for device A1 is described in Appendix A. The final results are shown as follows:

The twist angle on point A_d, as shown in Figure 3.5 (a), is

$$\Phi_{AA_d} = \frac{T_A L_a}{(GJ)_a} = \frac{T_{m,tot} L_a}{2(GJ)_a} \tag{3.2.6}$$

The maximum twist angle occurs just at the middle symmetric axis of the platform (perpendicular to the x-axis), as shown in Figure 3.5 (b), and this angle is given by

$$\Phi_{\max} \approx \frac{T_{m,tot} L_a}{2(GJ)_a} + \frac{T_{m,tot} L_b}{2(GJ)_b} + \frac{T_{m,tot} L_s}{8(GJ)_b} \tag{3.2.7}$$

➤ *Approximate calculation of GJ:*

First, consider a model with two layers: an oxide layer and a nitride passivation layer.

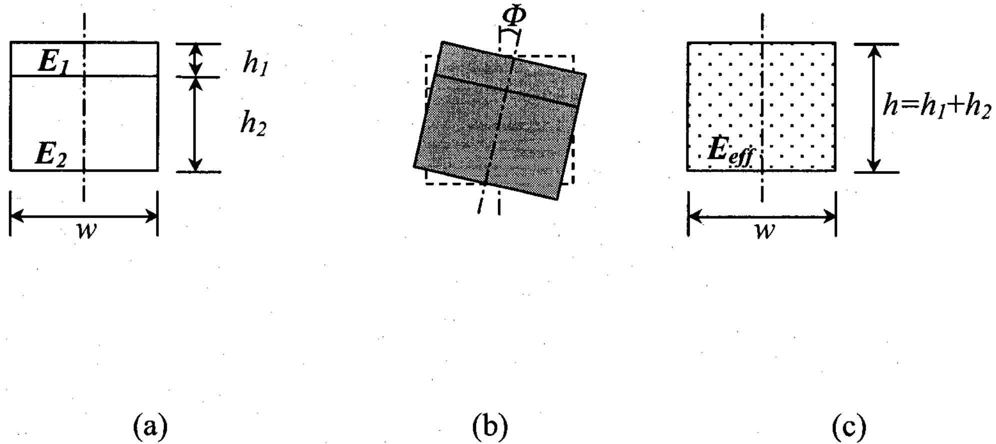

Figure 3.6: Composite arm of two materials

Generally, a composite bar, which cross section is shown in Figure 3.6(a), twists under a torque T, which is resisted by torques T_1 and T_2 developed in the nitride layer and oxide layer, respectively. From static equilibrium, we have

Reproduced with permission of the copyright owner. Further reproduction prohibited without permission.

$$T = T_1 + T_2 \tag{3.2.8}$$

The angles of twist are the same for both parts because they are bonded together. Therefore, from compatibility of rotations, we find the equation:

$$\Phi = \frac{T_1 L}{G_1 J_1} = \frac{T_2 L}{G_2 J_2} \tag{3.2.9}$$

in which L is the length of the bar. Solving equations (3.2.8) and (3.2.9) can give solutions of T_1 and T_2, the torques in the two parts of the bar, and then the angle of rotation Φ now becomes:

$$\Phi = \frac{TL}{G_1 J_1 + G_2 J_2} = \frac{TL}{(GJ)_{eff}} \tag{3.2.10}$$

in which $(GJ)_{eff}$ is the total torsion rigidity of the composite bar. A simple approach to approximately calculate Φ is shown in Figure 3.6(c), where the composite bar has been converted to a single material device with a simple rectangular cross section. The effective Young's modulus and Poisson ratio of this new model are defined by the following equations:

$$E_{eff} = \frac{\sum_{i=1}^{n} E_i A_i}{\sum_{i=1}^{n} A_i} = \frac{E_1 h_1 + E_2 h_2}{h_1 + h_2} \tag{3.2.11}$$

$$\nu_{eff} = \frac{\sum_{i=1}^{n} \nu_i A_i}{\sum_{i=1}^{n} A_i} = \frac{\nu_1 h_1 + \nu_2 h_2}{h_1 + h_2} \tag{3.2.12}$$

Then, using equation (3.2.7), we can get

$$(GJ)_{eff} = G_{eff} J_{eff} = \frac{E_{eff}}{2(1 + \nu_{eff})} J_{eff} \tag{3.2.13}$$

Reproduced with permission of the copyright owner. Further reproduction prohibited without permission.

For a rectangular cross section, the torsion constant J_{eff} can be calculated by equation (3.2.14) [28]:

$$J_{eff} = \left(\frac{h}{2}\right)^3 \left(\frac{w}{2}\right)\left[\frac{16}{3} - 3.36\frac{h}{w}\left(1 - \frac{h^4}{12w^4}\right)\right] \quad (3.2.14)$$

where w and h ($w \geq h$) are the width and thickness of torsion bar, respectively.

The equations (3.2.13) and (3.2.14) can be directly used for a device made from a single material.

Table (3-2): The results of twist angles for micromirror device A1

	I (mA)	Φ_{AB} (°)	Φ_{max} (°)
Without any passivation layer	10	0.0369	0.0379
$h = 4.1$ μm	20	0.0737	0.0757
Without nitride passivation layers	10	0.0266	0.0273
$h = 4.6$ μm	20	0.0532	0.0546
With nitride and oxide passivation layers	10	0.0143	0.0147
$h = 5.1$ μm	20	0.0286	0.0293

- ***The further simplification:***

From equations (3.2.1), (3.2.6-7) and (3.2.11-14), we can calculate Φ_{AAd} (the twist angle at the point A_d) and Φ_{max} (the maximum twist angle of the device).

Data in Table (3-2) indicate that Φ_{max} is very similar to Φ_{AB} under the same magnetic

Reproduced with permission of the copyright owner. Further reproduction prohibited without permission.

torque $T_{m,tot}$ (the same magnetic field B and same driving current I). The relative difference between Φ_{max} and Φ_{AB} is only about 2.7%. Thus the twist angle contributed by the platform is much less than the twist angle produced by support arms.

In equation (3.2.14), when w >> h, the torsion constant J_{eff} is proportional to the width of the cross section w. Because the width of support arms is 20 μm, while the width of the platform is 300 μm, J_a (on the arm) << J_b (on the platform), and $(GJ)_a \ll (GJ)_b$. Moreover, the L_b is much less than L_a as shown in Figure 3.4. Therefore, the second and third terms in equation (3.2.7) can be ignored. Comparing with equation (3.2.6), we also obtain the result that Φ_{max} can be approximated by Φ_{AB}.

Based on the result $(GJ)_a \ll (GJ)_b$, we can simplify the model further by ignoring the deformation occurring on the platform. Putting the discussion in a wider context, we found that the rigidity of the platform, either for torsion (GJ) or for bending (EI), is much larger than the rigidity of arms. Therefore, the movement of the micromirror could be approximated by the torsion or bending results of the support arms.

3.2.1.2 Static Deflection Mode II: parallel movement

Returning to the deflection mode shown in Figure 3.2(b), the parallel displacement of platform in Device A1 can be approximately treated as the bending problem for a fixed-to-fixed beam, as shown in Figure 3.7(a):

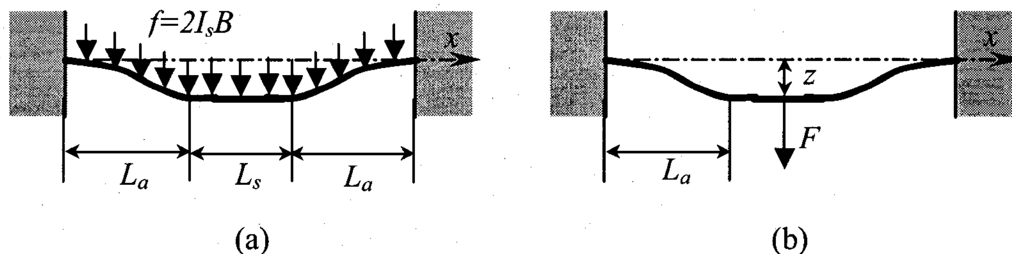

Figure 3.7: Schematic diagrams of clamped-clamped beams

Reproduced with permission of the copyright owner. Further reproduction prohibited without permission.

where L_a denotes the length of a support arm, and f (f=$2I_sB$) is the unit load. L_s is the effective length of one driving trace, while B and I_s are the external magnetic field and driving current, respectively.

A simpler model can be obtained by replacing the uniform distributed forces by a concentrated force F at the central of the platform, as shown in Figure 3.7(b). Here we ignore the deformation of the platform. Then, the total concentrated force F can be approximated as

$$F \approx 0.5 f(2L_a) + fL_s = 2I_sB(L_a + L_s) \qquad (3.2.15)$$

And the vertical displacement of the platform is given by [28]:

$$z \approx \frac{F(2L_a)^3}{192\ (EI)} = \frac{I_sB(L_a + L_s)(L_a)^3}{12\ (EI)} \qquad (3.2.16)$$

in which E is the Young's modulus of the arm, and I is the bending moment of inertia.

➢ *Calculation of centroidal moment of inertia for bending*

To calculate the bending moment of inertia of arms in device A1, the rectangular shape of the cross section, which now contains two different materials, oxide and nitride, can be transformed into a T-shaped cross section with the same Young's modulus as the oxide portion by scaling the width of nitride layer by a factor of r, which is the ratio of the elastic modulus of nitride to oxide, as illustrated in Figure 3.8(b). [29]

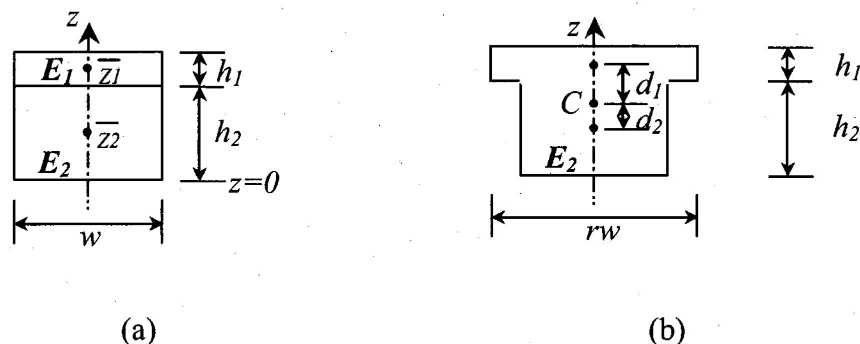

Figure 3.8: The cross-sectional view of a support arm: (a) original; (b) transformed.

Reproduced with permission of the copyright owner. Further reproduction prohibited without permission.

$$r = \frac{E_1}{E_2} = \frac{E_{nitride}}{E_{oxide}} = \frac{380000}{75000} = 5.0667 \quad (3.2.17)$$

The centroid C of the transformed cross section is located at

$$\begin{aligned}\overline{Z} &= \frac{\sum \overline{Z}_i A_i}{\sum A_i} = \frac{\overline{Z}_1 \times r \times w \times h_1 + \overline{Z}_2 \times w \times h_2}{r \times w \times h_1 + w \times h_2} \\ &= \frac{4.85 \times 5.0667 \times w \times 0.5 + 2.3 \times w \times 4.6}{5.0667 \times w \times 0.5 + w \times 4.6} \\ &= 3.2056 \ (\mu m)\end{aligned} \quad (3.2.18)$$

Then, the moment of inertia I of the area, shown in Figure 3.8(b), is given by equation (3.2.19):

$$\begin{aligned}I &= \sum(\bar{I} + Ad^2) = \bar{I}_1 + A_1 d_1^2 + \bar{I}_2 + A_2 d_2^2 \\ &= \frac{1}{12}(5.0667 \times w) \times 0.5^3 \\ &+ 5.0667 \times w) \times 0.5 \times 1.6444^2 \\ &+ \frac{1}{12} w \times 4.6^3 + w \times 4.6 \times 0.9056^2 \\ &= 18.7869\, w \quad [\mu m^4]\end{aligned} \quad (3.2.19)$$

where w is the width of the support arms in μm. For all the devices discussed in this thesis, w is 20 μm.

3.2.2 Dynamic Response Modeling

The resonant response of a micromirror device is an important parameter for many practical applications, such as the application of optical switches, projective display systems, and optical shutters. This section presents the basic theoretical analysis of dynamic response for the device A1.

Reproduced with permission of the copyright owner. Further reproduction prohibited without permission.

3.2.2.1 Classical Vibration Theory for Single Degree-of-freedom Systems

In a single degree-of-freedom system, the motion of the system can be fully specified by a single value at any time [30]. For example, the behaviour of the micromirror can be expressed by the vertical displacement of the platform, when external loads applied on the device in such a way as shown in Figure 3.7. Similarly, the motion of the structure can be related by the rotation angle, if the platform tilts under external magnetic torque excitation as shown in Figure 3.4.

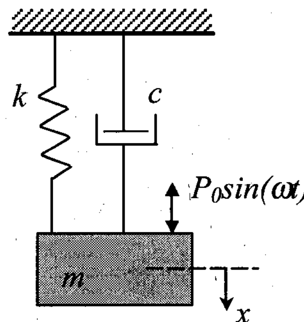

Figure 3.9: The single degree of freedom system subject to forced vibration with viscous damper.

The differential equation governing the forced vibration of a single degree of freedom system, as shown in Figure 3.9, is given by [31]

$$mx''+cx'+kx = P_0 \sin(\omega t) \qquad (3.2.20)$$

with initial conditions

$$x(0) = x_a$$
$$x'(0) = x'_a$$

where x(t) is the deformation, m is the mass of the system, c is the coefficient of damping, k is the stiffness of the structure, and $P_0\sin(\omega t)$ is the external alternating load applied on

Reproduced with permission of the copyright owner. Further reproduction prohibited without permission.

the system.

The theory of mechanical vibration gives the complete solution of the equation (3.2.20), which is the sum of the homogeneous and particular solutions.

When the loading function is given by $P_0\sin(\omega t)$, the particular solution of equation (3.2.20) is also expected to be harmonic. Then steady-state response is: [31]

$$x_p(t) = x_0 \sin(\omega t - \varphi) \tag{3.2.21}$$

where w_0 and φ denote the amplitude and phase angle of the response, respectively:

$$x_0 = \frac{P_0 / k}{\sqrt{(1 - \frac{\omega^2}{\omega_n^2})^2 + (2\xi \frac{\omega}{\omega_n})^2}} \tag{3.2.22}$$

and

$$\varphi = \tan^{-1}(\frac{c\omega}{k - m\omega^2}) \tag{3.2.23}$$

In equation (3.2.22), ω_n is the parameter of undamped natural frequency:

$$\omega_n = \sqrt{k/m} \tag{3.2.24}$$

And, ξ is the damping ratio, which is defined by

$$\xi = \frac{c}{2m\omega_n} \tag{3.2.25}$$

Generally, ξ is unknown and depends on the environment medium, such as air, flow etc. For small values of damping, ξ can be approximated using the bandwidth method, as shown in the equation (3.2.26):

$$\xi = \frac{f_2 - f_1}{2f_{max}} \tag{3.2.26}$$

Reproduced with permission of the copyright owner. Further reproduction prohibited without permission.

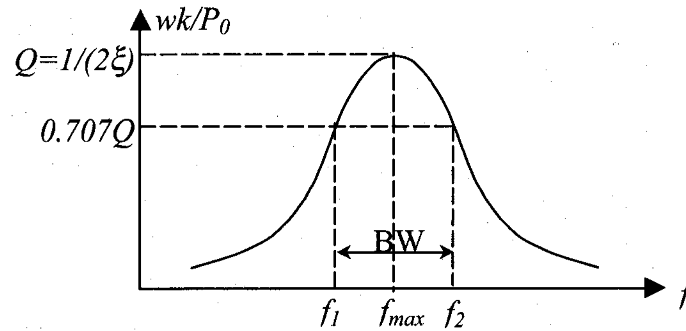

Figure 3.10: Example of a harmonic response curve showing half power points and bandwidth.

where f_{max} is the frequency at which the system has the maximum amplitude of vibration response, while f_1 and f_2 are called the half power points, and they correspond to the amplitude values 0.707 times of the maximum amplitude. In Figure 3.10, we define a value, referred to as the quality factor, Q:

$$Q \approx \frac{1}{2\xi} = \frac{f_{\max}}{f_2 - f_1} \tag{3.2.27}$$

Q can be used for estimating the equivalent viscous damping in a mechanical system.

3.2.2.2 *Dynamic Behaviour for Torsional Systems*

Section 3.2.1.1 discussed static response of the angular deflection for the micromirror device unit A1. The dynamic behaviour of the device can be analyzed by modifying the differential equation (3.2.20) for an angular system. The angular oscillator is described by

$$I\frac{d^2\theta}{dt^2} + C_\theta \frac{d\theta}{dt} + K_\theta \theta = M_e(t) \tag{3.2.28}$$

with angular moment of inertia I, angular damping C_θ, angular stiffness K_θ, and external

Reproduced with permission of the copyright owner. Further reproduction prohibited without permission.

magnetic torque $M_e(t)$, which is given by the equation (3.2.1).

The moment of inertia I, dominated by the mirror platform I_{mirror}, is expressed as

$$I = I_{arms} + I_{mirror} \approx I_{mirror} = \int r^2 dm \qquad (3.2.29)$$

As illustrated in Figure 3.3, the micromirror can be approximately considered as a device composed of an oxide plate and a nitride coating. The angular moment of inertia is given by

$$I \approx I_{mirror} = \int r^2 dm = \int \rho L_m t r^2 dr = \frac{2}{3}(\rho_{ni} t_{ni} + \rho_o t_o) L_m (\frac{w_m}{2})^3 \qquad (3.2.30)$$

where L_m is the length of the mirror plate; ρ is the material density; w_m is the width of the mirror plate; t_{ni} and t_o are the thickness of nitride and oxide, respectively.

The angular stiffness can be obtained from equation (3.2.5) directly.

$$K_\theta = T_{m,tot} / \Phi_{AB} = 2\frac{(GJ)_a}{L_a} \qquad (3.2.31)$$

where L_a is the length of a support arm; $(GJ)_a$ is the torsion rigidity of the arm, and it can be approximately calculated using the method discussed in the section 3.2.1.1. The natural linear frequency is expressed as

$$f_{nr} = \frac{1}{2\pi}\sqrt{\frac{K_\theta}{I}} \qquad (3.2.32)$$

Finally, the steady-state response of the micromirror device unit A1 under external alternating loads can be expressed as

$$\theta(t) = \theta_0 \sin(\omega t - \varphi) \qquad (3.2.33)$$

where

Reproduced with permission of the copyright owner. Further reproduction prohibited without permission.

$$\theta_0 = \frac{BL_sL_dI_s / k_\theta}{\sqrt{\left(1-\frac{f^2}{f_{nr}^2}\right)^2 + \left(2\xi_\theta \frac{f}{f_{nr}}\right)^2}} \tag{3.2.34}$$

θ_0 represents the amplitude of angular oscillation of the micromirror device; I_s is the amplitude of driving current; B, L_s, and L_d denote the external magnetic field, the effective length of an aluminum trace, the distance between two parallel traces on the platform, respectively. ξ_θ can be calculated from the experiment results.

3.2.2.3 The Vertical Vibration

The static response of the parallel displacement for the micromirror device unit A1 was discussed in the Section 3.2.1.2. Similarly, the micromirror plate can have vertical vibration under external alternating loads as shown in Figure 3.7. The dynamic behavior is then described by the following differential equation:

$$M\frac{d^2z}{dt^2} + C_z\frac{dz}{dt} + K_z z = P(t) \tag{3.2.35}$$

where M is the mass of the system; C_z is the coefficient of the damping; P(t) denotes Lorentz forces applied on the devices.

Apparently, the mass of the system is also dominated by the mirror platform.

$$M = M_{arms} + M_{mirror} \approx M_{mirror} = (\rho_{ni}t_{ni} + \rho_o t_o)L_m w_m \tag{3.2.36}$$

where L_m is the length of the mirror plate; ρ is the material density; w_m is the width of the mirror plate; t_{ni} and t_o are the thickness of nitride and oxide, respectively.

The structure stiffness K_z is the ratio of the applied load to the resultant deflection z, as shown in the following equation:

$$K_z = F_{load} / z \tag{3.2.37}$$

For the simple center load mode, K_z can be obtained from the equation (3.2.16).

Reproduced with permission of the copyright owner. Further reproduction prohibited without permission.

$$K_z = \frac{192\,(EI)}{(2L_a)^3} \tag{3.2.38}$$

where L_a is the length of a support arm; EI is the rigidity of the arm, and it can be approximately calculated using the method discussed in the section 3.2.1.2. Similarly, the natural linear frequency is expressed as

$$f_{nz} = \frac{1}{2\pi}\sqrt{\frac{K_z}{M}} = \frac{1}{2\pi}\sqrt{\frac{192EI}{M(2L_a)^3}} \tag{3.2.39}$$

The results from the theoretical estimation discussed in this chapter will be verified by experiment and simulation results.

Reproduced with permission of the copyright owner. Further reproduction prohibited without permission.

Chapter 4

ANSYS Simulation

Finite element analysis (FEA), or the finite element method (FEM), is a numerical technique for analyzing complex engineering problems that do not have closed-form analytical solutions. In the finite element method, a complicate object is divided into many small or manageable pieces, or elements. The behaviour of physical quantities on each element can be described with a relatively simple set of equations. By assembling the elements, the whole system can be represented with an extremely large set of simultaneous equations. This resulting set of equations is then solved to obtain the global approximate solutions. With the rapidly growth of the computing ability of computers and the development of reliable FEM software, FEM is now widely used throughout most areas of engineering; applications of finite element method include linear and nonlinear structural, thermal, coupled-field, flow analysis etc.

A commercial finite element software package ANSYS Version 6.1 was used for simulating the operation of micromirror devices in this project. In general, the finite element analysis using ANSYS includes three distinct steps:

- building the model
- applying loads and obtaining the solutions
- reviewing the results

In the first step, the geometry of the device, element types and constants of material

Reproduced with permission of the copyright owner. Further reproduction prohibited without permission.

properties are defined to create the model. This resulting model is then discretized or meshed. The second step in the finite element analysis involves the definition and application of loads onto the model and obtaining the solution. In the last step, the results of the simulation can be reviewed using ANSYS postprocessors. Contour display, deformed shapes, tabular lists and graph plots can be obtained to interpret the simulation results.

The ANSYS software package includes many built-in programs to deal with different types of finite element simulation problems, such as static, harmonic, and transient analysis. This chapter reviews the simulation of static characteristics and dynamic response of the micromirror devices.

4.1 Building Models

Building a model includes input geometry of the device, choosing a suitable element type, and defining constants, such as the thickness, orientation, Young's modulus, Poisson ratio and other material properties of the composite structures.

Two-dimensional data extracted from L-Edit layout design, as described in the Chapter 2, are used as the base to create the three-dimensional models in ANSYS. The constants of material properties are given in the Table (3-1).

Over 150 different element types can be found in the ANSYS element library. Different element types, having different numbers of nodes and degrees of freedom, are suitable for different analysis types and structures of the devices. Two element types, designated SOLID92 and SOLID46 by ANSYS have been chosen for building the models of micromirror devices.

4.1.1 The Basic Models Using Element SOLID92

SOLID92 is a 3-D 10-Node Tetrahedral Structural Solid element, as shown in Figure 4.1.

Reproduced with permission of the copyright owner. Further reproduction prohibited without permission.

Each node of the element has three degrees of freedom: translations in the x, y and z directions. The tetrahedral shape of the element can represent irregular meshes, which occurred in the simulation for some fine structures in micromirror devices.

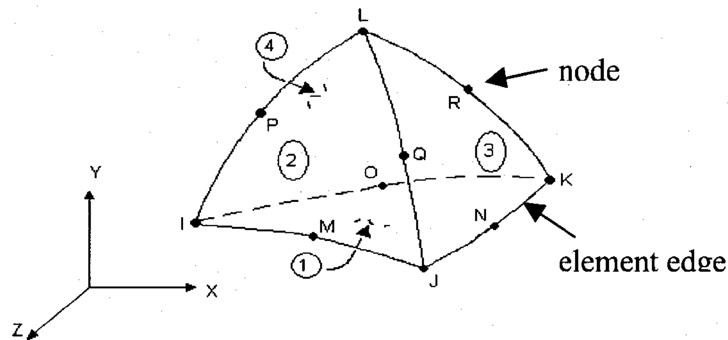

Figure 4.1: Schematic of the 3-D 10-node Tetrahedral Structural Solid element SOLID92

The basic entities of a 3-D micromirror model with element SOLID92 were volumes, which can have irregular shape. Some layout design tools, such as MEMS Pro and AutoCAD, provide special programs to extract a 2-D layout design to a 3-D model. Here the thickness profile, or the process data containing layer thickness information, should be defined before 2-D/3-D conversion.

Using Boolean operators offered by ANSYS, we can modify entities and create the final model. Figure 4.2 gives an example of the half model for a micromirror device. In this model, five volumes represent the nitride layer, aluminum mirror, aluminum traces and the oxide layers that were merged together, respectively.

Following the definition of the system geometry and the element attributes, the system was meshed to generate nodes and elements, as shown in the Figure 4.2(e). The mesh size was refined in order to achieve the convergence of results, which means further refinement of the mesh no longer produces appreciable changes in results.

ANSYS limits the numbers of nodes and elements for a simulation task. Even under this limitation, the more elements/nodes in the model, the higher requirements for the

Reproduced with permission of the copyright owner. Further reproduction prohibited without permission.

computer hardware to solve an analysis problem, such as longer CPU time and much more data storage space.

For the symmetric devices, a good method to reduce the element/node number but still keep the small mesh size is to cut the whole model along the symmetric axis and analyze only one of the resulting pieces. The model shown in Figure 4.2(e) is only a half of the micromirror device A1. This model contains about 22000 elements and more than 35000 nodes after meshing. The micromirror devices with more complicate arm designs have more elements/nodes, and, consequently, require extensive run-time, especially for the dynamic response simulation.

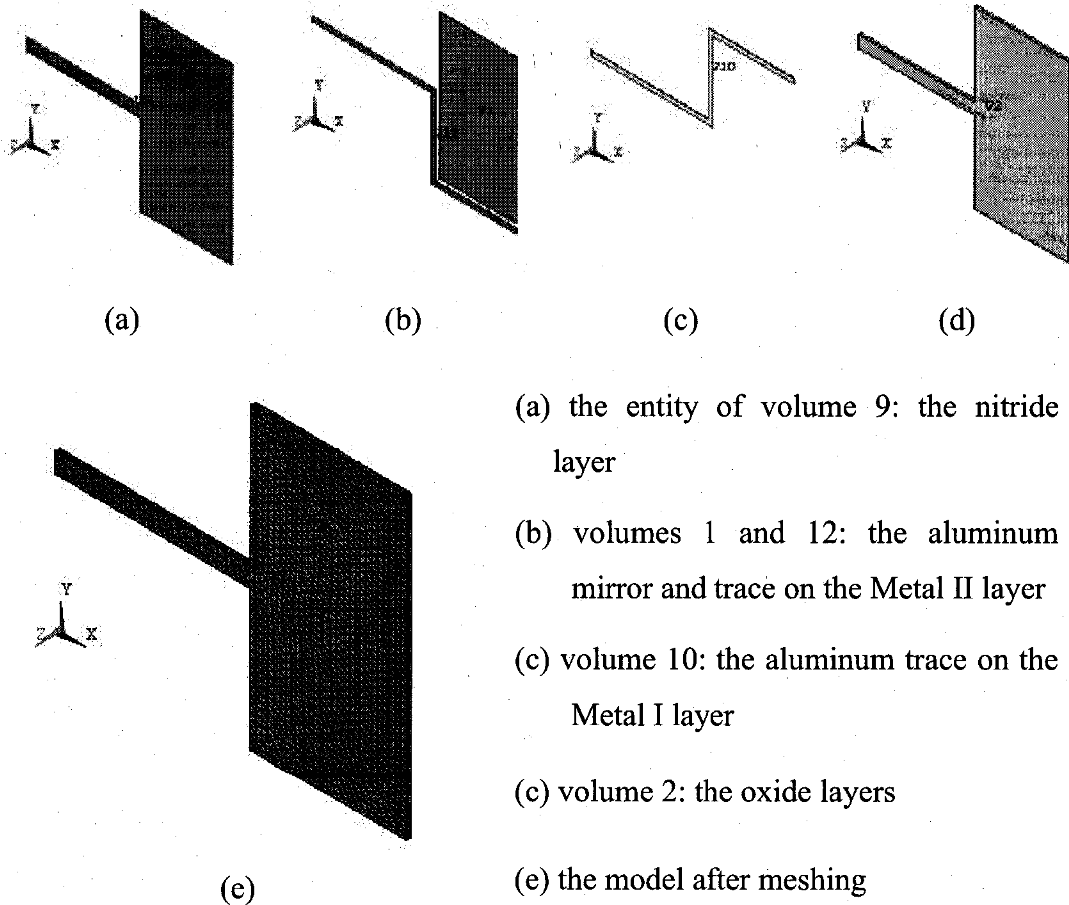

(a) the entity of volume 9: the nitride layer

(b) volumes 1 and 12: the aluminum mirror and trace on the Metal II layer

(c) volume 10: the aluminum trace on the Metal I layer

(c) volume 2: the oxide layers

(e) the model after meshing

Figure 4.2: The half model of a micromirror device.

Reproduced with permission of the copyright owner. Further reproduction prohibited without permission.

4.1.2 Simplified Models Using Element SOLID46

The element type SOLID46 was introduced in order to reduce the number of elements/nodes in the micromirror models. This element is a 3-D layered 8-node structural solid designed to model layered shells or solids, shown in Figure 4.3.

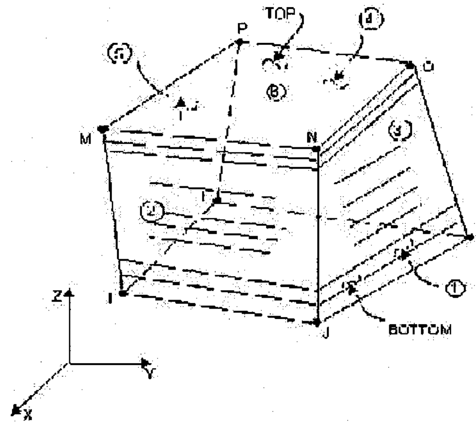

Figure 4.3: Schematic of the 3-D 8-node Layered Structural Solid element SOLID46

A SOLID46 element itself has the layered structure, therefore we can specify only one element along thickness during meshing, and define different element types with different internal layers to achieve a composite structure. This is a method to reduce the meshing work from three-dimensional to two-dimensional, and finally produce fewer nodes and elements for modeling the same device, as shown in Figure 4.4.

In a micromirror device, the SiO_2 section of the platform, enveloping aluminum mirror and traces, can be considered as a homogenous material structure, because aluminum and silicon dioxide have comparable material properties, as indicated in the Table (3-1). Therefore, simple 2-layer elements were generated in the platform and support arms of the micromirror devices. The cross section of the two-layer structure has been illustrated in Figure 3.3(b) already.

When meshing the micromirror models created with element type SOLID46, the number of elements along structural edges was adjusted. For instance, more elements were

Reproduced with permission of the copyright owner. Further reproduction prohibited without permission.

generated in the regions where large stress or strain gradients are expected. Also, mesh refinement for the whole device was conducted to achieve the convergence of simulation results. The final model of micromirror device A1 with element SOLID46 contained only about 5000 elements, thus significantly saved the run-time of simulation and the data storage space.

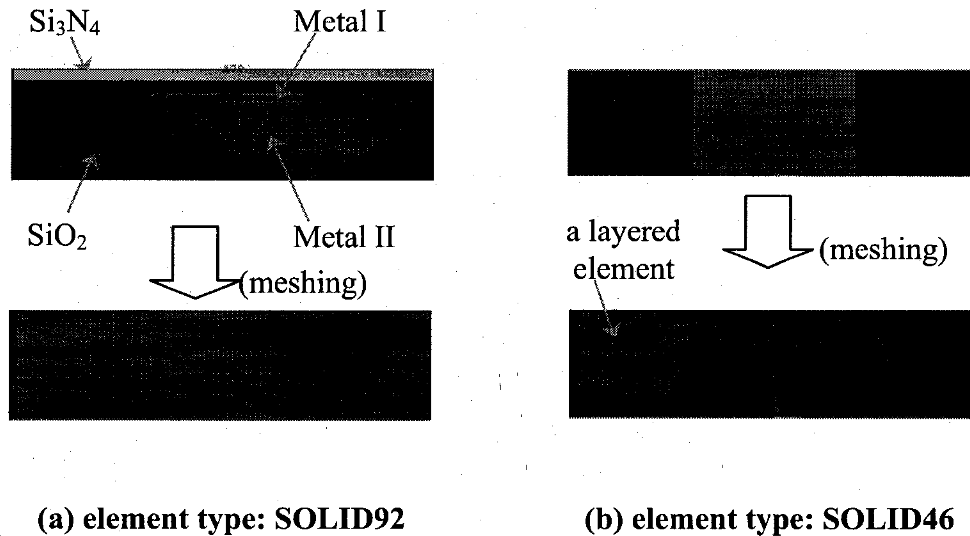

(a) element type: SOLID92 **(b) element type: SOLID46**

Figure 4.4: Cross-sectional view of meshing results on the arm

4.2 Static and Dynamic Analyses

After model creating, the second step in ANSYS simulation process includes load definition and applications. Generally, the loads may be defined as constraints, forces, surface loads, body loads, inertia loads and coupled field loads.

For the micromirror models studied in this project, only constrains and forces were applied. The models were constrained at the ends of support arms in every degree of freedom. This was performed by constraining the end areas in the x, y and z directions to zero. The Lorentz forces on the device were calculated using equation (3.1.1), and applied along the centre line of the aluminum traces. Two examples of complete models, meshed, constrained, and with applied loads (of the micromirror device A2), are shown

Reproduced with permission of the copyright owner. Further reproduction prohibited without permission.

in Figure 4.5.

Both static and dynamic analyses were conducted for the micromirror models. First, in static analysis, the loads are constant for each test. Additional tests were conducted by applying currents varying from 5 mA to 25 mA. Second, ANSYS modal analysis was used to determine the natural frequencies and mode shapes of a micromirror structure. Last, harmonic (sinusoidal) loads were applied in dynamic response analysis. The magnitude, phase angle and the frequency range were required to specify a harmonic load.

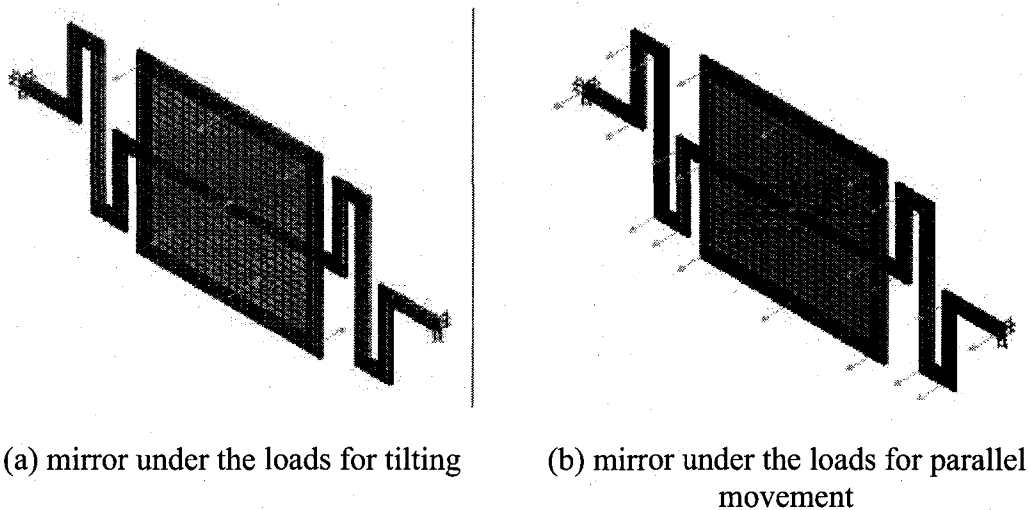

(a) mirror under the loads for tilting (b) mirror under the loads for parallel movement

Figure 4.5: ANSYS models of the micromirror device A2 under influence of simulated Lorentz forces

4.3 ANSYS simulation Results

Several micromirror devices with different arm designs were modeled and simulated in this project. An important result observed is that the static deflection, either angular rotation or parallel movement, of the micromirror device has a linear relationship to the driving current, as shown in Figure 4.6 and Figure 4.7. This linear relationship allows for predictability in the following actuation.

Micromirror devices B and D have two pairs of driving traces, and they can tilt about two

Reproduced with permission of the copyright owner. Further reproduction prohibited without permission.

axes. In Figure 4.6 and Figure 4.7, the label DeviceB:X means device B is only under the actuation resulting from currents flowing through two traces parallel to x direction, while the label DeviceB:Y means device B is actuated by the currents flowing in y direction. Similar labels were defined for device D.

From Figure 4.6 and Figure 4.7, the micromirror device A2 offered the greatest angular deflection and parallel displacement of all of the mirrors tested at the same driving currents. The performances of micromirror device D were also largely than the basic design device A1. Moreover, this design allows for angular deflection in two directions. As for the micromirror devices B and C, the results of them were not as good as device A1, although they have more complicate arm designs.

The Von Mises Stress was observed for each actuation methods related to the curves in Figure 4.6 and Figure 4.7. It was also found that the maximum stresses in each mirror design were quite small, but could be critical in the micro-domain. A linear relationship between the stress and the driving current was also observed, as shown in Figure 4.8 and Figure 4.9.

Table (4-1) gives the first four natural frequencies of micromirror devices simulated by ANSYS. These results will be discussed in the Chapter 5.

Table (4-1) ANSYS results: Natural frequencies of micromirror devices

	f_1 (kHz)	f_2 (kHz)	f_3 (kHz)	f_4 (kHz)
Device A1	34.732	36.492	102.227	144.429
Device A2	16.663	17.500	42.634	65.522
Device B	48.411	63.181	100.052	191.992
Device C	37.556	47.743	82.162	165.831
Device D	21.338	32.390	40.313	91.144

Reproduced with permission of the copyright owner. Further reproduction prohibited without permission.

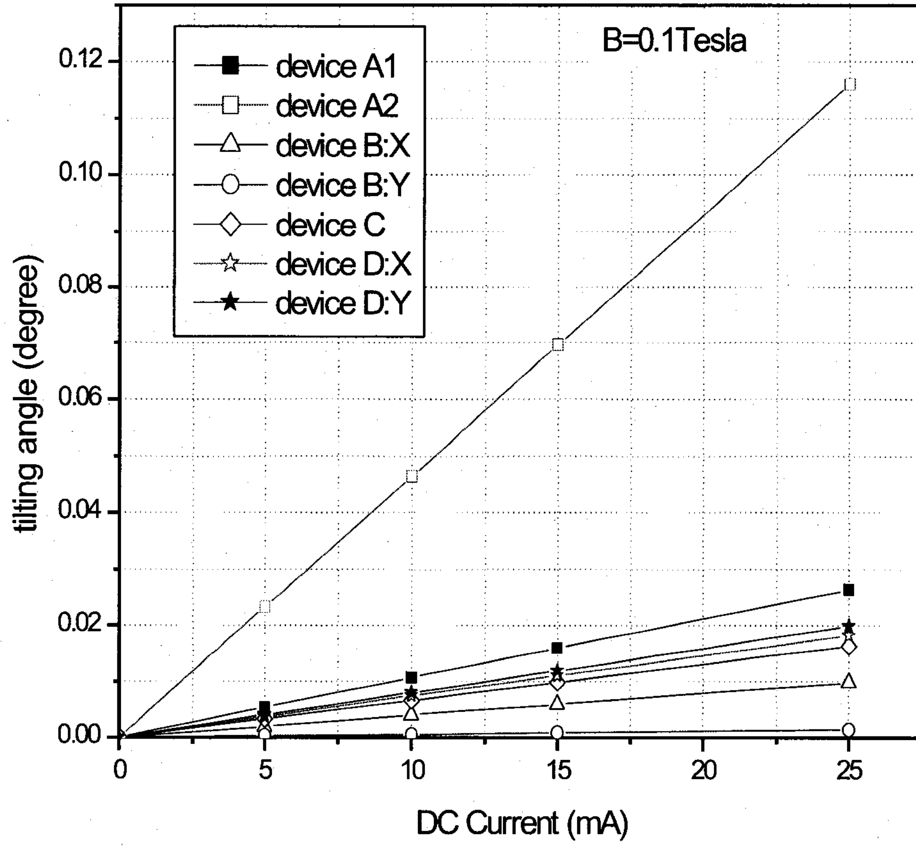

Figure 4.6: The angular deflection of micromirror devices.

Reproduced with permission of the copyright owner. Further reproduction prohibited without permission.

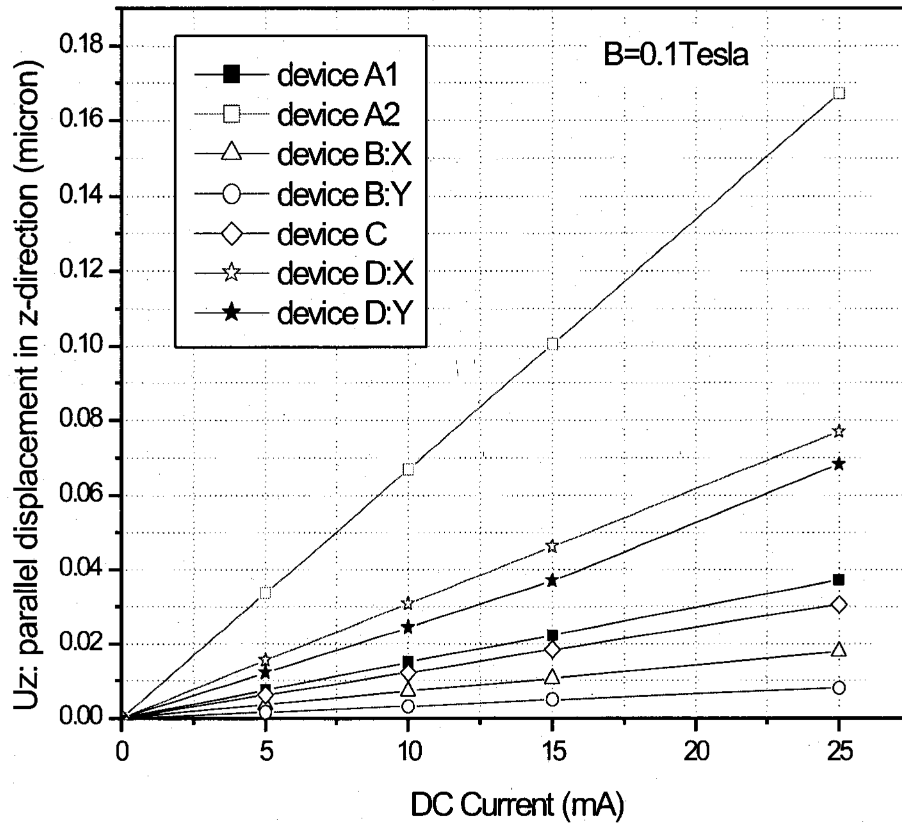

Figure 4.7: The parallel displacement of micromirror devices.

Reproduced with permission of the copyright owner. Further reproduction prohibited without permission.

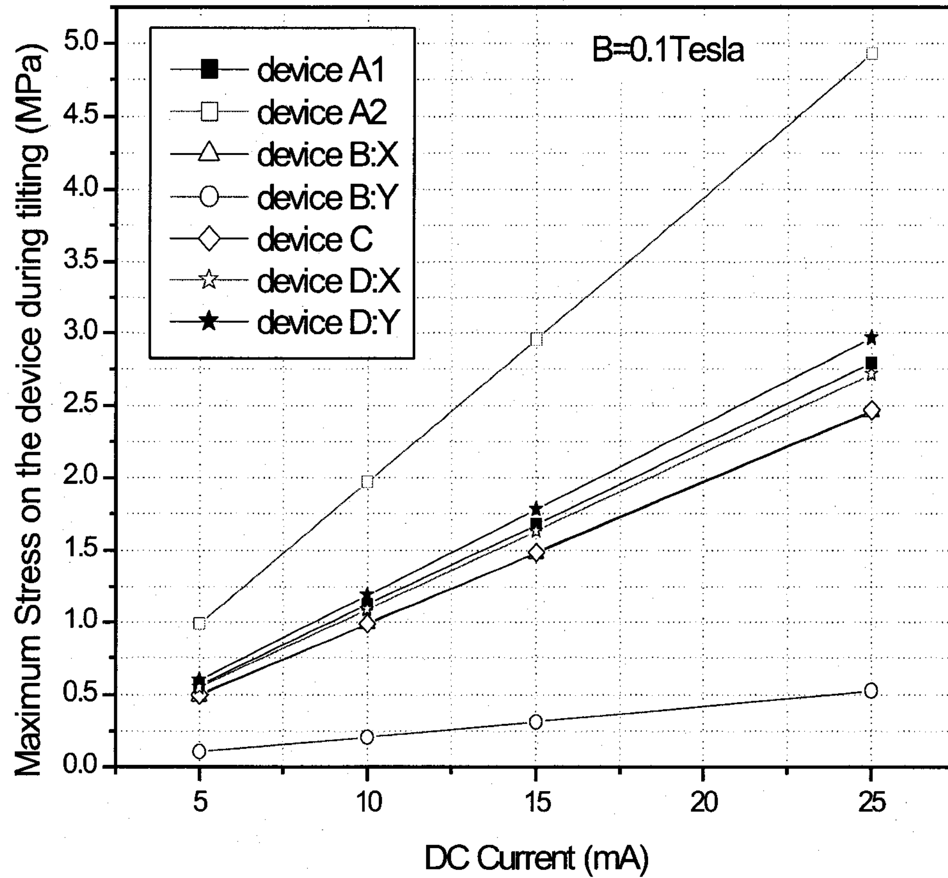

Figure 4.8: Stress on micromirror devices during tilting.

Reproduced with permission of the copyright owner. Further reproduction prohibited without permission.

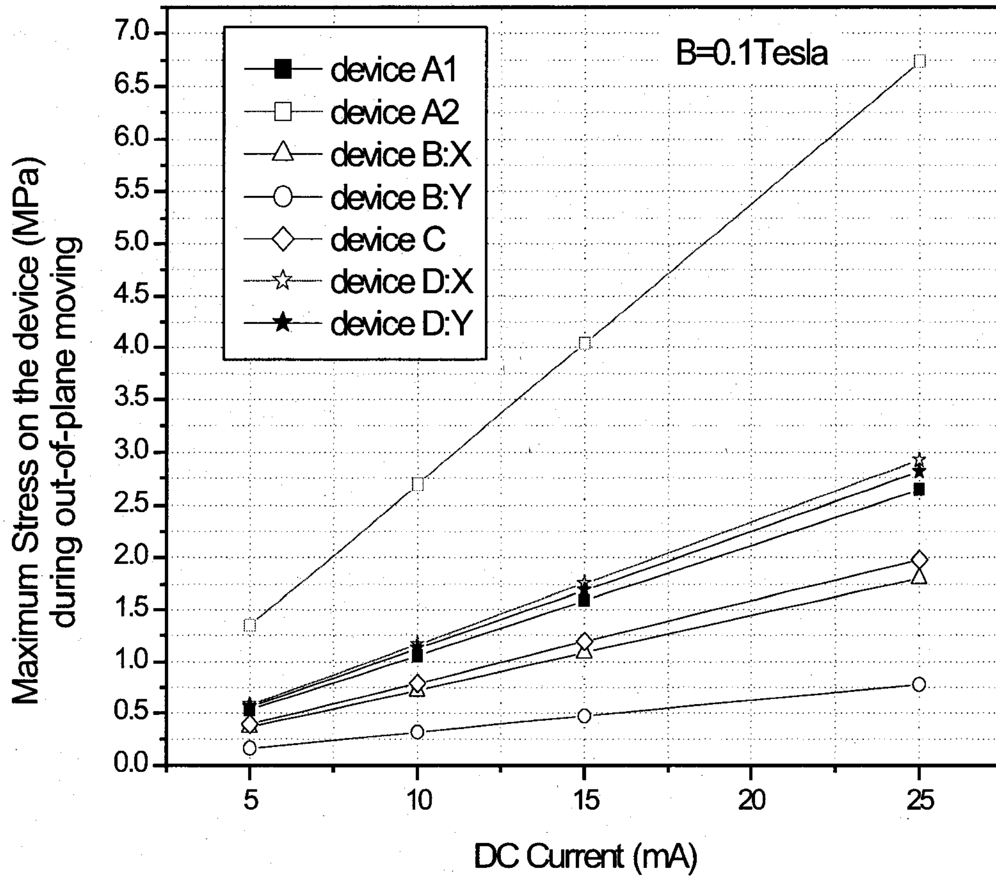

Figure 4.9: Stress on micromirror devices during parallel moving.

Reproduced with permission of the copyright owner. Further reproduction prohibited without permission.

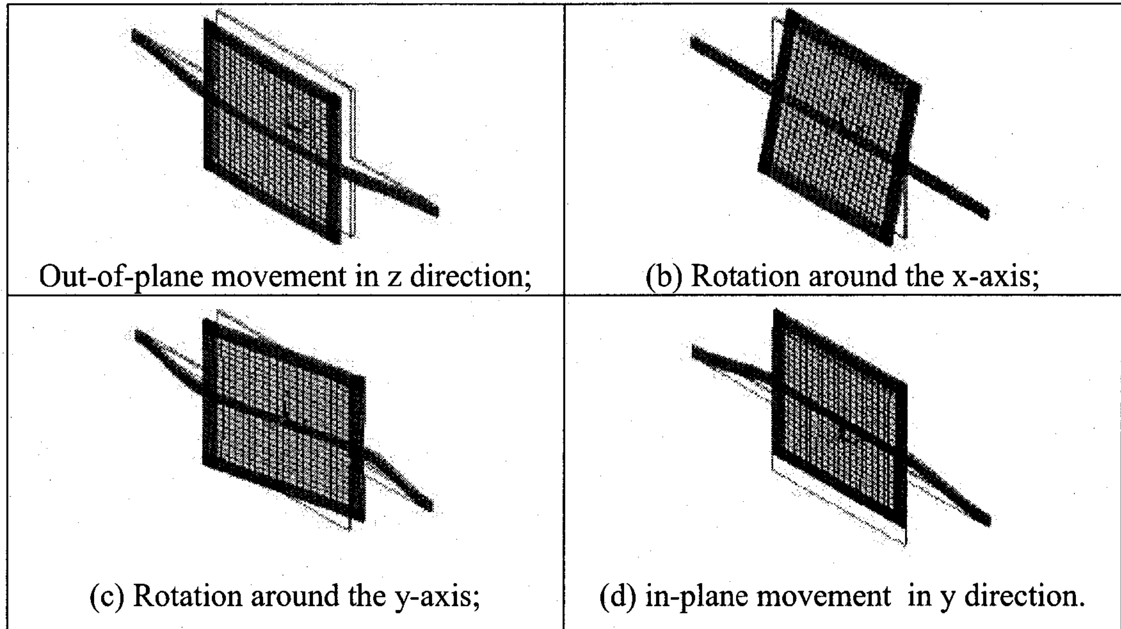

Figure 4.10: Vibration modes of the micromirror device A1.

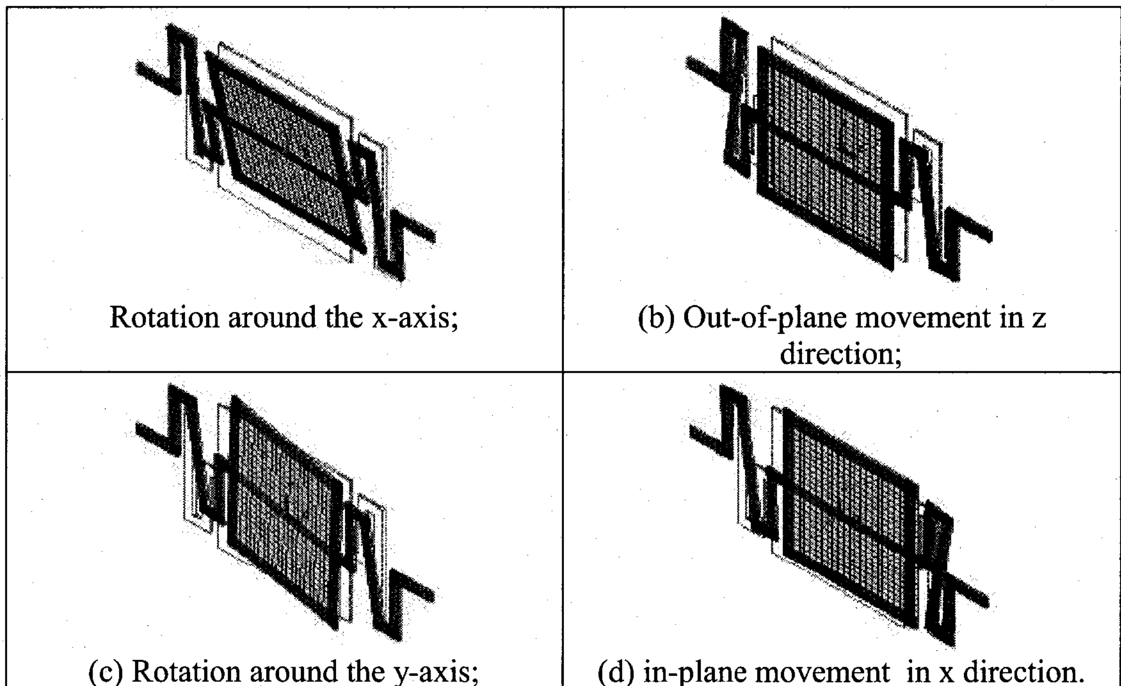

Figure 4.11: Vibration modes of the micromirror device A2.

Reproduced with permission of the copyright owner. Further reproduction prohibited without permission.

The vibration modes of micromirror device A1 and device A2 are given in Figure 4.10 and Figure 4.11, respectively. The shapes of vibration modes are different at different resonant frequencies. Parts (a), (b), (c) and (d) of the figures correspond to the vibration modes at the first four natural frequencies.

4.4 Limitation of ANSYS Simulation for MEMS devices

The accuracy of the ANSYS simulation is dependent on the material parameters and the model geometry. In the simulation work for micromirror devices, use of bulk values of some material properties, regarding the aluminum and several silicon dioxide layers as a uniform layer composed of homogenous material, and the assumption of rectangular cross sections of layers in CMOS devices may cause errors in simulation results. However, ANSYS simulation provides a good way to estimate the performances of the micromirrors and guidance to optimize the micromirror structures in future designs.

Reproduced with permission of the copyright owner. Further reproduction prohibited without permission.

Chapter 5

Experiments and Results

This chapter reviews the experimental methods utilized to measure the static deflection and the dynamic response of the micromirror devices. Results obtained from the experiments are presented, and compared with the data attained from both theoretical analysis and finite element simulation introduced in Chapters 3 and 4, respectively. The possible improvements for present designs are also discussed. Finally, potential applications of micromirror-based devices will be presented in this chapter.

5.1 Experimental Setup for Magnetically Actuation

The magnetically actuated micromirror devices were fabricated using the CMOS 1.5 μm double metal process offered by Mitel Corporation through CMC. The free standing micromirror structures were released by XeF_2 silicon etching, as described in Chapter 2.

In experiments, a 40pin Dual Inline Package (DIP) chip, containing the micromirror devices, was fixed onto a Zero Insertion Force (ZIF) socket. This ZIF socket was placed between the two poles of a horseshoe permanent magnet, which provided the required external magnetic field, as shown in Figure 5.1(a). The resultant magnetic field was measured using a Gaussmeter (Radio Frequency Laboratories, Inc., Model 1890). Within the central volume of 5 mm x 5 mm x 5 mm, as shown in Figure 5.1 (b), the magnetic field was relatively uniform with a value of 0.10 T. The relative variation was about 2.4%.

Reproduced with permission of the copyright owner. Further reproduction prohibited without permission.

(a) Experimental setup of external magnetic field.

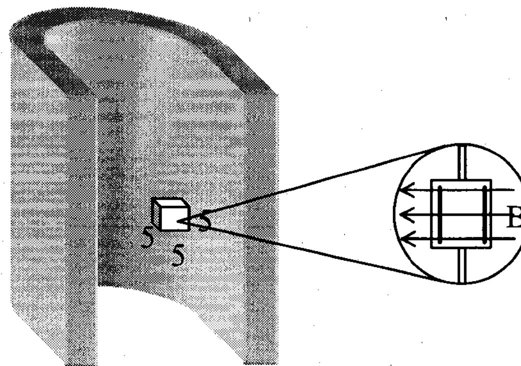

Dimensions are in mm.

(b) Conceptual diagram of the region with uniform magnetic field.

Figure 5.1: The external magnetic field.

For static testing, the actuation current required to produce Lorentz forces was provided by a HP 6205B Dual DC Voltage Supply. A 500 Ω resistor was placed in series with the device to minimize the effects of heating of the current traces in the micromirror devices, which in turn affects the resistance of the traces and produces a change in the actuation

Reproduced with permission of the copyright owner. Further reproduction prohibited without permission.

current. By incorporating the 500 Ω resistor in series, the actuation current will remain relatively constant, because the resistance of the trace, normally in the range from 10 to 30 Ω, is much smaller than 500 Ω. The value of diving current through the trace was obtained by measuring the voltage over this resistor using a HP 34401A Multimeter.

For dynamic testing, a HP 33120A Waveform Generator was used to create sinusoidal or other types of alternating input signals. The output of waveform generator and the voltage over the device were monitored using an oscilloscope, while the accurate value of the driving current was obtained using a HP 34401A multimeter.

The movements, both static and dynamic, of the micromirror platforms were measured by optical methods, as described in the following sections.

5.2 Angular Deflection

5.2.1 Optical Detection Method to Measure Angular deflection of Micromirrors

Figure 5.2 shows the experimental setup for the angular deflection measurement. The beam coming from a laser diode (Thorlabs Model S1021) was focused on the mirror plate of a micromirror device on the chip, and then reflected onto a flat paper screen.

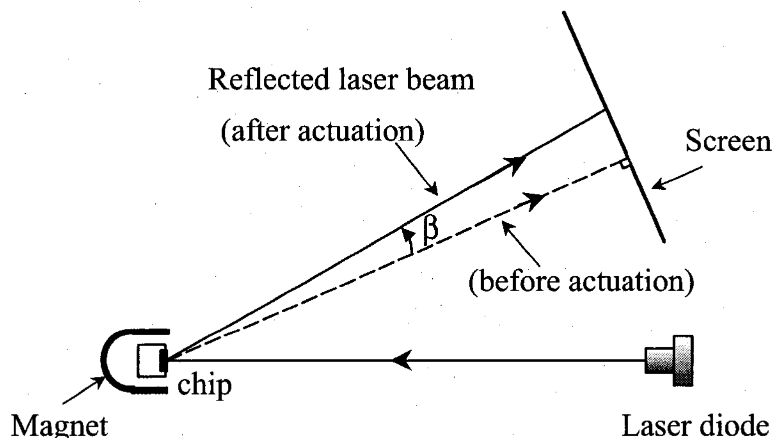

Figure 5.2: The experimental setup for the angular deflection measurement.

Reproduced with permission of the copyright owner. Further reproduction prohibited without permission.

In static deflection testing, the position of the reflected light spot on the screen before and after actuation was measured to determine the deflection angle, θ, of the micromirror, as illustrated in Figure 5.3, where α is the incident angle when the mirror plate is at rest, and β is the rotation angle of the laser beam before and after actuation. θ is the deflection angle of the mirror plate. Then

$$\begin{aligned} &\beta + 2\alpha + 2(90^\circ - \alpha - \theta) = 180^\circ \\ \therefore \quad &\beta = 2\theta \end{aligned} \tag{5.1.1}$$

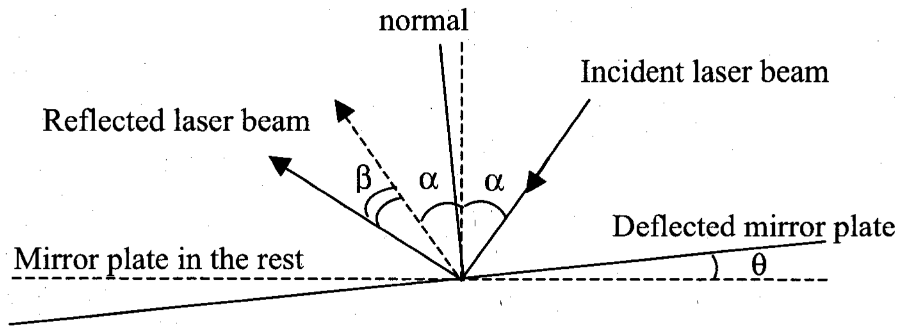

Figure 5.3: Deflection angle illustration.

In the experiments, DC driving currents varying from 5 to 35 mA were applied to the device both with and without the external magnetic field.

The frequency response around resonance was measured using the same experimental setup as for the static deflection test. Sinusoidal wave AC currents were applied to excite the oscillation. The reflected laser beam spread out into a fan of light, the width of which on the screen was measured and then related to the angle of deflection of the oscillating micromirror.

Reproduced with permission of the copyright owner. Further reproduction prohibited without permission.

5.2.2 Experimental Results of the Angular Deflection Testing

The results of the angular deflections for micromirrors, measured using the experimental techniques reviewed above, are presented in the following sections.

5.2.2.1 *Static Deflection*

Three tests were performed for each micromirror device to determine static deflection. In the first test, a DC actuation current was applied on the device in an external magnetic field to activate the micromirror for tilting. Then, the direction of the driving current was reversed in the second step. The last test repeated two previous tests when the external magnetic field was removed.

The purpose of the last two tests mentioned above is to eliminate the thermal effects, which act on the micromirror structures and also contribute to the deflection. As indicated in reference[32], this deflection comes from electro-thermal actuation, which involves Joule heating in the metal layers and subsequent differential thermal expansion of the structural layers.

Several micromirror devices were tested for investigating static deflection. Only the micromirrors in device A1, device A2 and device C showed angular deflections. Other devices did not function properly because problems encountered in design, fabrication or post-processing, as mentioned in the Chapter 2. Figures 5.4, 5.5 and 5.6 show the results, obtained using the optical detection method outlined in Section 5.2.1, for the micromirror device A1, A2 and C, respectively. Here the device A1 and C were activated via double driving traces, while device A2 has only one current driving trace, along one edge of the platform, because of the defects of chip fabrication.

In all Figures concerning static deflection in this section, the term "Thermal" in labels represents the deflection resulting only from electro-thermal actuation. The terms "Lorentz Positive" and "Lorentz Negative" denote the Lorentz force at the top of

Reproduced with permission of the copyright owner. Further reproduction prohibited without permission.

micromirror to tilt the structure up out of the plane of substrate and towards the substrate, respectively.

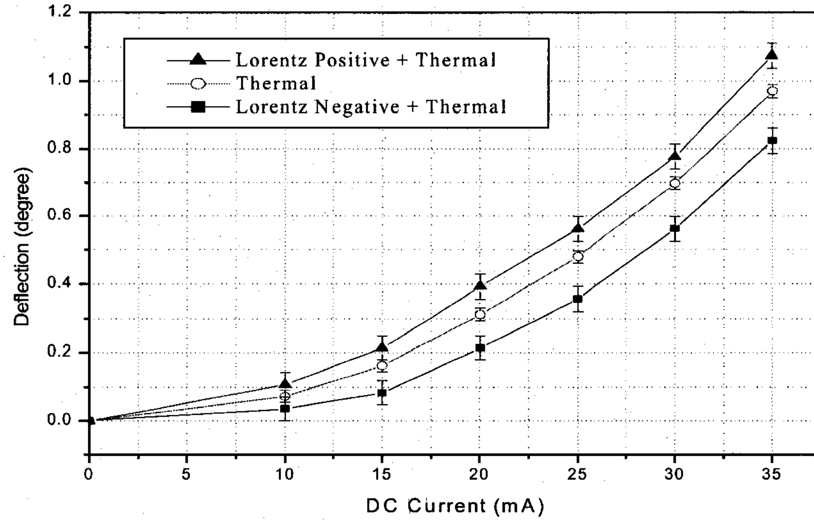

Figure 5.4: Static angular deflection of micromirror device A1.

(activated by double driving traces)

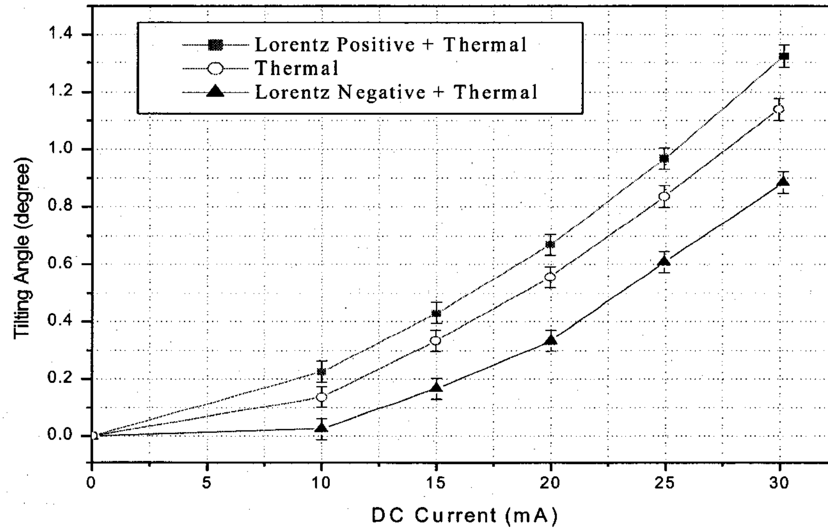

Figure 5.5: Static angular deflection of micromirror device A2.

(activated by a single driving trace)

Reproduced with permission of the copyright owner. Further reproduction prohibited without permission.

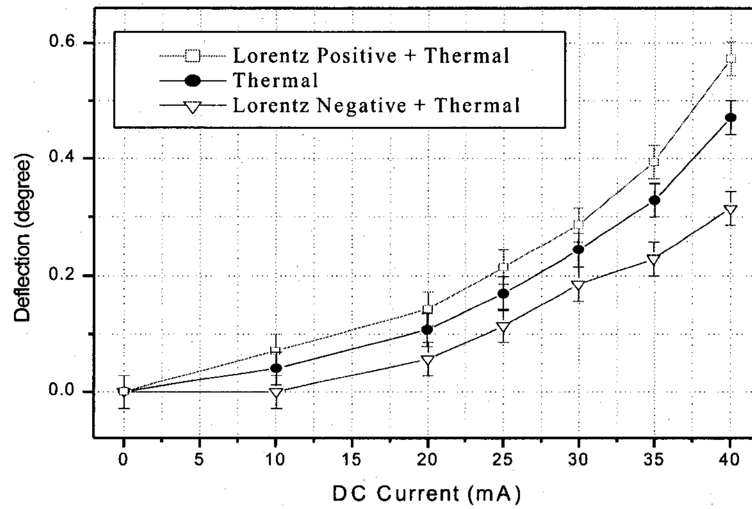

Figure 5.6: Static angular deflection of micromirror device C.
(activated by double driving traces)

In Figures 5.4 to 5.6, the data points are connected with straight lines. The curves are not linear as estimated in Chapter 3 and 4, because the thermal effect is included in the deflection and it is non-linear. In order to extract the magnetic deflection, the thermal effects have been subtracted from the corresponding curves of total deflections. Figure 5.7, 5.8 and 5.9 illustrate the deflection solely contributed by Lorentz forces for the device A1, A2 and C, respectively.

In Figures 5.7 to 5.9, the deflection for device A1, A2 or C is approximately linear with respect to the current, as estimated in previous chapters. However, the curves for deflection, actuated by positive and negative Lorentz forces, are not symmetric. This is a result of residual stress acting on the micromirror structures, which increases the deflection of device in one direction but hinders in the other.

Reproduced with permission of the copyright owner. Further reproduction prohibited without permission.

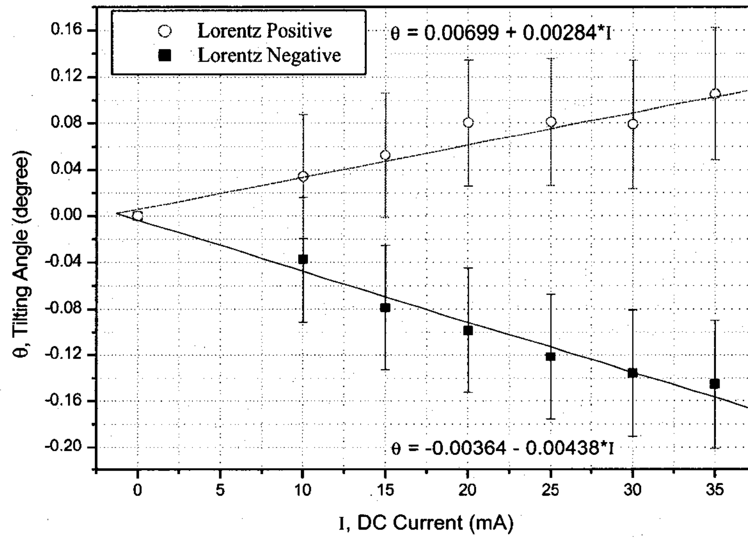

Figure 5.7: Static angular deflection of micromirror device A1 due to Lorentz forces only.

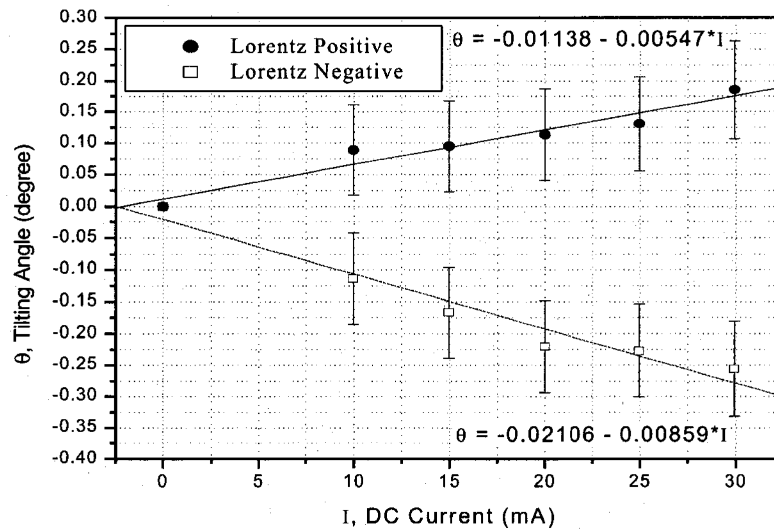

Figure 5.8: Static angular deflection of micromirror device A2 due to Lorentz forces only.

Reproduced with permission of the copyright owner. Further reproduction prohibited without permission.

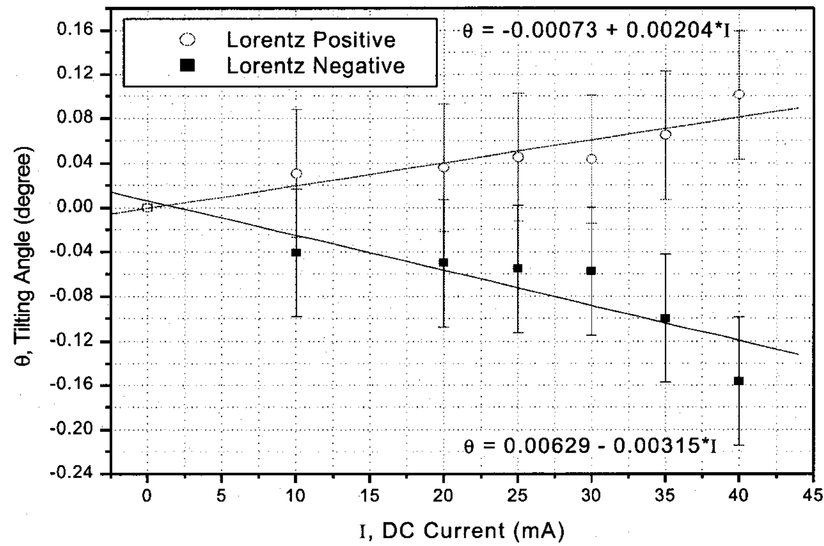

Figure 5.9: Static angular deflection of micromirror device C due to Lorentz forces only.

The experimental results of static angular deflection will be compared with theoretical estimation and FEM simulation in the section 5.2.3.

5.2.2.2 Dynamic Response

The dynamic response of micromirror devices was measured utilizing the method introduced in Section 5.2.1. Figures 5.10, 5.11 and 5.12 show the resonant responses for devices A1, A2 and C, respectively. These results were obtained when sine wave AC currents were applied to actuate the device. The driving current was 21 mA_{pp} (peak-to-peak).

The resonant frequency for device A1 was measured to be approximately 21.2 kHz, 11.3 kHz for device A2, and about 34.7 kHz for device C. When driving current went though two aluminum traces on the mirror platform, the maximum deflection, or the amplitude of vibration at resonance was approximately 6.7° and 2.4° for device A1 and device C, respectively. As for device A2, which has only one driving trace, the maximum deflection at resonance was about 5.6° .

Reproduced with permission of the copyright owner. Further reproduction prohibited without permission.

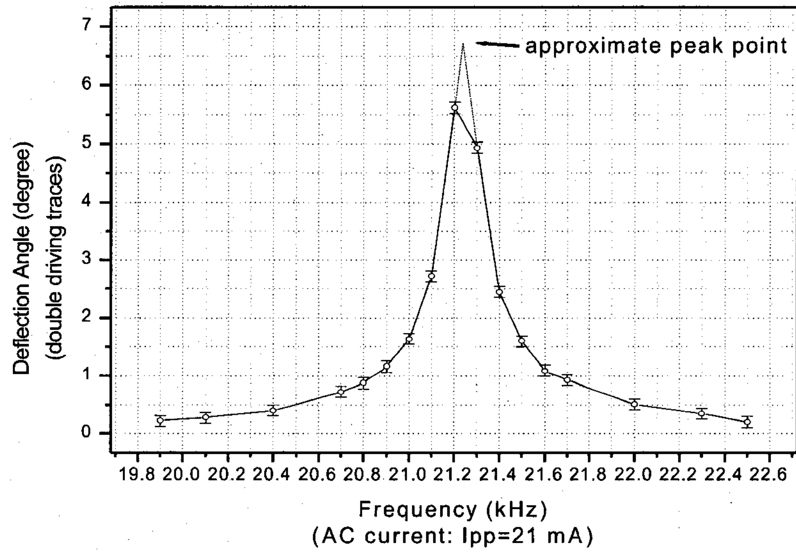

Figure 5.10: Dynamic angular deflection of micromirror device A1.

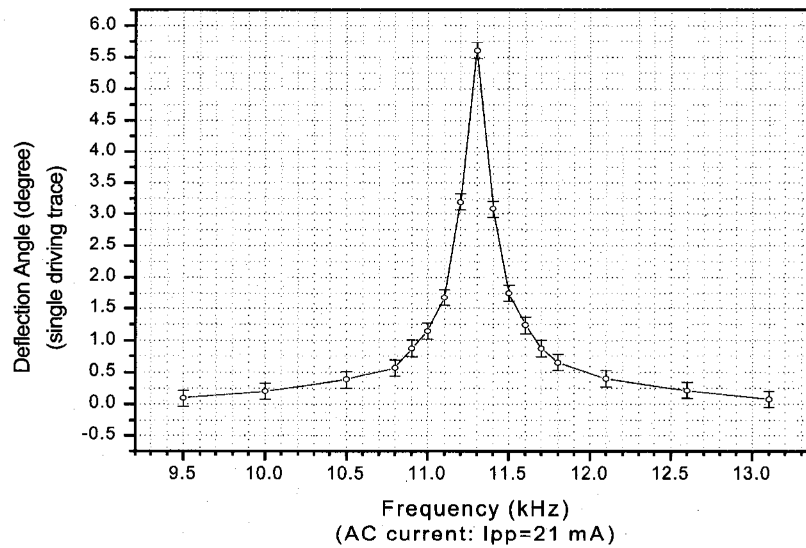

Figure 5.11: Dynamic angular deflection of micromirror device A2.

Reproduced with permission of the copyright owner. Further reproduction prohibited without permission.

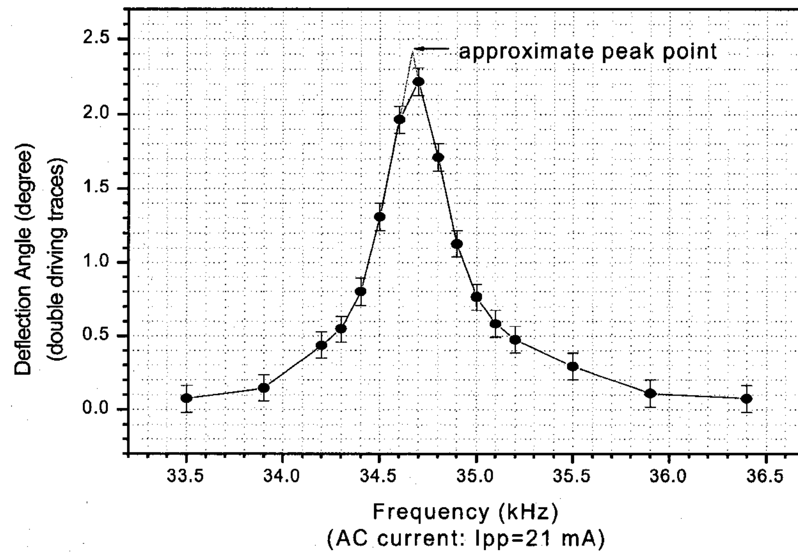

Figure 5.12: Dynamic angular deflection of micromirror device C.

At resonance, the angular deflection of the micromirror device was much larger than it under the DC current actuation. The resonant frequencies of micromirrors have been measured under different input currents. Figure 5.13 illustrates the relationship between the maximum rotation angles at resonance and the amplitude of input driving current for device A1, A2 and C, respectively. The curves in this Figure are approximately linear, as predicted in the Section 3.2.2.1. (Also, device A1 and device C were actuated by double current traces, while only one driving current went through deice A2; that means device A2 operates only under about half of the Lorentz force compared to devices A1 and C.)

It was found that the resonant frequencies of micromirror devices changed slightly under different input current. For instance, when the input current increased from 4 mA_{pp} to 30mA_{pp}, the resonant frequency of device C decreased from 34.70 kHz to 34.62 kHz. The shift of resonant frequency may result from the variation of temperature of the support arms. The increased current increased the average temperature of composite arms, and changed the inherent stress and stiffness of the arms, thus changing the resonant frequency. For the micromirror devices studied in this project, the resonant frequency variation with input current was less than 0.1 kHz. This variation must be considered in

Reproduced with permission of the copyright owner. Further reproduction prohibited without permission.

some applications, such as a precise resonant sensor.

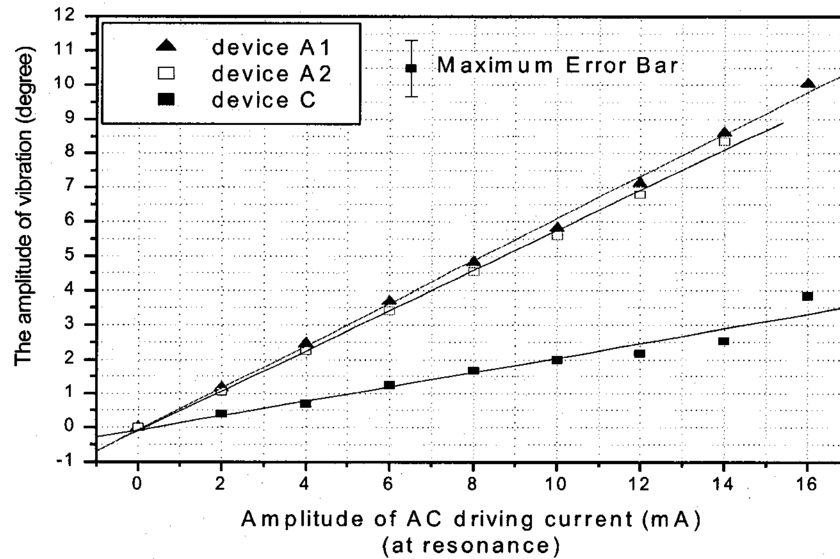

Figure 5.13: Maximum angular deflections at resonance for given value of AC current.

5.2.3 Discussion on the Angular Deflection Testing

In this section, the performance of static angular deflection of micromirror devices obtained from optical testing is compared with the data from finite element simulation. For the simplest design Device A1, the experimental data are also compared with the theoretical calculation results.

5.2.3.1 Static Deflection

Figure 5.14 shows the resultant data obtained from optical testing, analytical calculation and ANSYS simulation for the micromirror Device A1. The Figure 5.15 and 5.16 illustrate the results of optical experiments and ANSYS simulation for micromirror Devices A2 and C, respectively.

Reproduced with permission of the copyright owner. Further reproduction prohibited without permission.

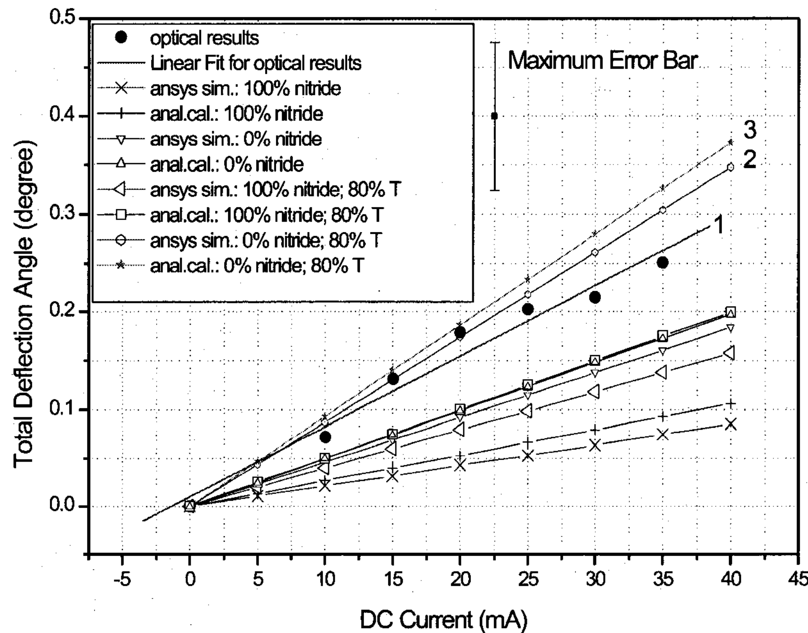

Figure 5.14: ANSYS, theoretical, and optical experimental data for static angular deflection of micromirror device A1.

In Figure 5.14, 5.15 and 5.16, the label "total deflection" denotes the total angular displacement up and down. It was obtained by reversing the DC driving current, as described in section 5.2.2.1. These figures show that experimental deflections of micromirror devices are all larger than the corresponding analytical calculation and ANSYS simulation for the models built up from the original designs. The discrepancy could result from the reasons as follows:

1. Inaccurate thickness profile used in the analytical calculation and ANSYS simulation

The layer thickness profile used in calculation and simulation is obtained from the data of CMOS 1.5 micron process provided by Mitel Corporation. However, Mitel concedes that the specified thickness of the layers may deviate by 10 to 20%. Furthermore, some design rules have to be violated in order to create MEMS structures using the standard CMOS fabrication process, so that some layers may be attacked by subsequent

Reproduced with permission of the copyright owner. Further reproduction prohibited without permission.

processing steps; thus the thickness of some layers may be changed. Also, over-etching in the post processing could change the dimension of the device. When the thickness of the structure decreases, the centroidal moment of inertia also decreases and finally results in a larger deflection of the real structure than that of the analytical or FEM.

The analytical estimation and ANSYS simulation of device A1 for the model that has 20% shrinkage in thickness are presented in Figure 5.14. Also, Figure 5.15 and 5.16 give the simulation results of varied-thickness models for the device A2 and C, respectively.

2. The nitride passivation layer was diminished after etching

In the original designs of micromirror devices as described in the chapter 2, the topmost layer on each device is a 0.5 μm thick nitride layer, serving as a part of the passivation layer. The nitride layer contributes greatly to the stiffness of the devices, because Young's modulus of nitride is about five times greater that of the silicon dioxide and aluminum layers. Therefore, a reduced thickness of the nitride layer could result in an increase of the deflections.

ANSYS simulations and theoretical calculations were conducted not only for the original designs, but also for the models with varying thickness of the nitride layer. As shown in Figure 5.14, the model of nitride-free but with 20% shrinkage in thickness best approximates the experimental results (curve 1). The FEM (curve 2) and theoretical (curve 3) models show excellent agreement of results for the micromirror Device A1, with errors of approximately 9% for nitride-free models; larger deviations are evident in comparing the two models with experimental data (curve 1). For the Device A1, there is approximate 24% difference between the best-fit curve for the total deflection (curve 1) and the analytical calculation results represented by curve 3, and 16% difference between curve 1 (experimental data) and curve 3 (nitride-free and 80% thickness ANSYS model).

Reproduced with permission of the copyright owner. Further reproduction prohibited without permission.

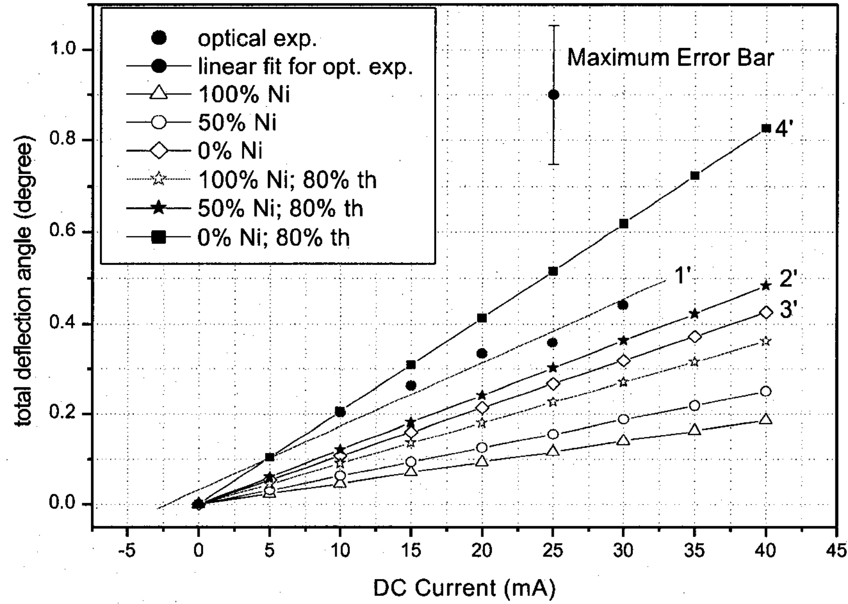

Figure 5.15: ANSYS simulation and optical experimental data for static angular deflection of micromirror device A2.

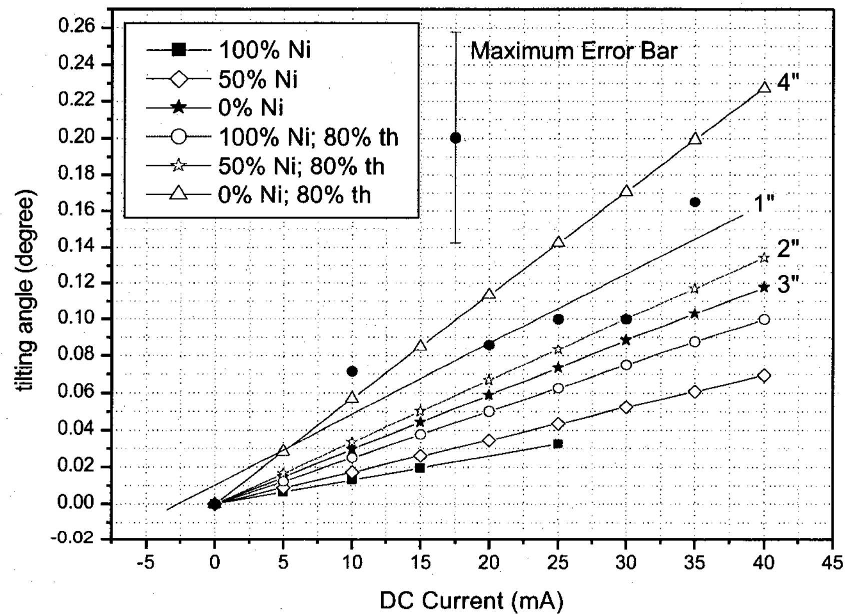

Figure 5.16: ANSYS simulation and optical experimental data for static angular deflection of micromirror device C.

Reproduced with permission of the copyright owner. Further reproduction prohibited without permission.

In Figure 5.15, curve 1′ represents the linear fit of experimental results, and curve 2′ and 4′ are the ANSYS simulation results for the 80% thickness models with 50% and 0% nitride layer, respectively. Data in curve 3′ are from the ANSYS simulation for the simple nitride-free model. For device A2, experimental results are most close to curve 2′, the difference between curve 1′ and curve 2′ is about 20%; it is approximately 30% between curve 1′ and curve 3′, and 36% between curve 1′ and curve 4′.

Similar results are obtained for device C as shown in Figure 5.16, where the curve numbers are similar to those in Figure 5.15. The differences between curve 1″ and other curves are: 19% for curve 2″, 29% for curve 3″, and 38% for curve 4″.

Table (5-1): Finite element, analytical and optical results for Figures 5.14, 5.15, and 5.16.

	Device A1[a]	Device A2[b]	Device C[a]
Methods	Slope [°/mA]	Slope [°/mA]	Slope [°/mA]
Optical	7.26 x10^{-3}	1.41 x10^{-2}	3.82 x10^{-3}
ANSYS (100% thickness) 100% Nitride	2.13 x10^{-3}	4.66 x10^{-3}	1.31 x10^{-3}
50% Nitride	2.78 x10^{-3}	6.24 x10^{-3}	1.74 x10^{-3}
0% Nitride	4.60 x10^{-3}	1.06 x10^{-2}	2.95 x10^{-3}
ANSYS (80% thickness) 100% Nitride	3.95 x10^{-3}	9.01 x10^{-3}	2.51 x10^{-3}
50% Nitride	5.22 x10^{-3}	1.21 x10^{-2}	3.35 x10^{-3}
0% Nitride	8.70 x10^{-3}	2.06 x10^{-2}	5.69 x10^{-3}
Analytical (80% thickness) 100% Nitride	4.50 x10-3		
0% Nitride	9.32 x10-3		

NOTE:
a: The slopes were calculated from the linear-fitted approximation curves for the experimental data;
b: the driving current flows through two parallel aluminum traces on the mirror platform;
c: single driving trace on the mirror platform.

Reproduced with permission of the copyright owner. Further reproduction prohibited without permission.

From Figure 5.14, 5.15, 5.16 and table(5-1), the simulation results from models with 80% thickness and a diminished nitride layer are most close to the experimental results. Device A1 is little different from Device A2 and Device C. The last two designs have more complicated support arms, and there are more residues around the corners of these arms, therefore change the resonant frequencies.

3. Residual stress on the micromirror device.

Micromirror devices are comprised of certain layers, which are either in tension or in compressing as a consequence of thermal cycles and differing deposition rates during manufacture. These compressive and tensile stresses will limit the deflection of structure either into or out of the plane of motion.

5.2.3.2 Dynamic Response

In this section, the data obtained in Chapter 3 and Chapter 4 for the dynamic behavior of micromirror devices are compared with the experimental results.

Similar to the static analysis discussed in the last section, the experimental results of the dynamic response of real devices are quite different from those of the models built up using the original thickness profile. Real devices perform the larger deflections at the resonance and lower resonant frequencies. By reducing the thickness of the nitride layer and even the total thickness of the device, deflections compatible with the experimental results can be obtained from both analytical calculation and finite element analysis.

The damping ratios used in analytical calculation and finite element analysis are borrowed from the results of optical experiments. It is approximately 0.33% for the device A1, 0.58% for the device A2, and about 0.37% for the device C. Figure 5.17 illustrates the analytical estimation, ANSYS simulation and optical measurements for device A1. Figure 5.18 and 5.19 show the results from finite element analysis and optical experiments for device A2 and C, respectively.

Reproduced with permission of the copyright owner. Further reproduction prohibited without permission.

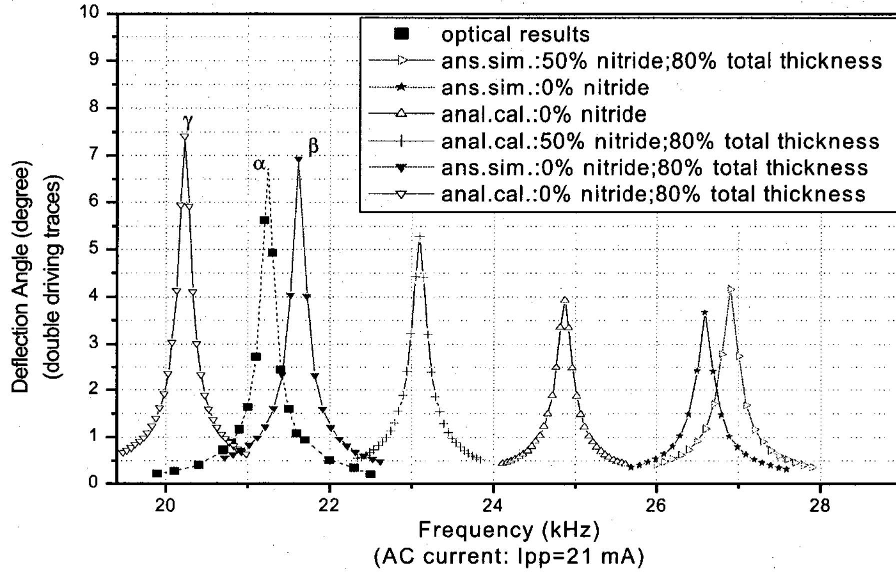

Figure 5.17: ANSYS, theoretical, and optical experimental data for dynamic response of micromirror device A1 (angular deflection).

The maximum deflections and frequencies at resonance of are also presented in Table 5.2. For the device A1, the resonant frequency and deflection obtained from optical experiments correspond with least error to the nitride-free and reduced dimension model (80% of thickness). The difference in maximum deflection between the simulated (curve β) and optical results (curve α) is approximately 3.3%, in comparison with a difference of approximately 10.4% between analytical (curve γ) and optical results; the difference in resonant frequency is about 1.8% between curve β and curve α, and 4.8% between the analytical (curve γ) and optical data (curve α). The Figures 5.14 and 5.17 would suggest that the thickness of the real device is smaller than the original design of micromirror device A1, and most nitride passivation layer is etched during post-processing in XeF_2.

Reproduced with permission of the copyright owner. Further reproduction prohibited without permission.

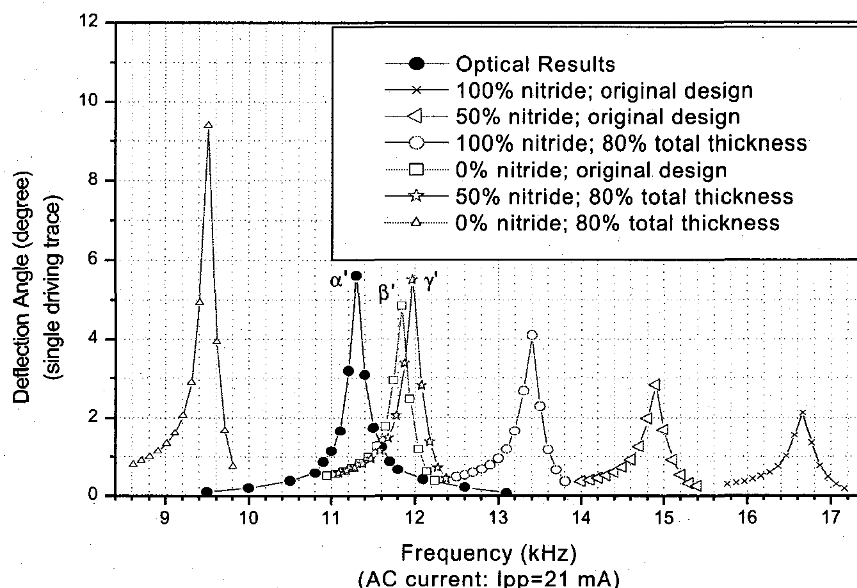

Figure 5.18: ANSYS simulation and optical experimental data for dynamic response of micromirror device A2 (angular deflection mode).

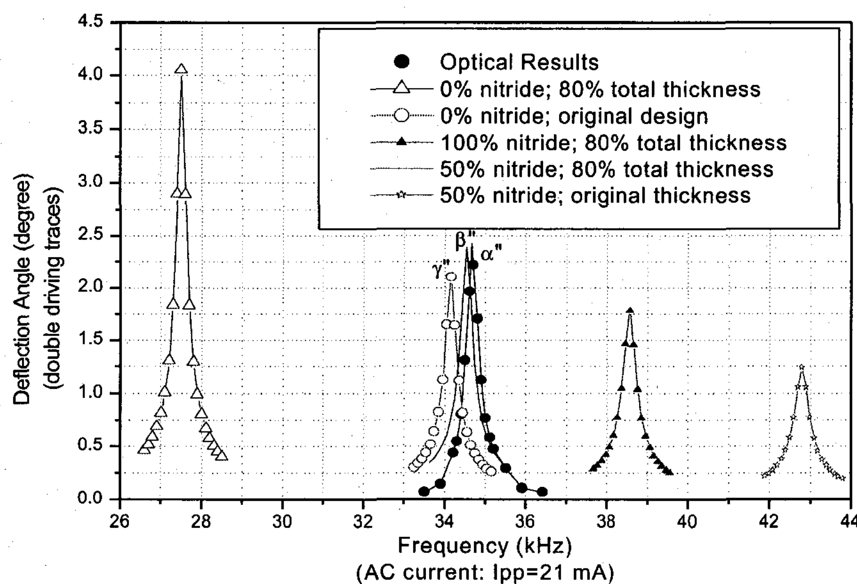

Figure 5.19: ANSYS simulation and optical experimental data for dynamic response of micromirror device C (angular deflection mode).

Reproduced with permission of the copyright owner. Further reproduction prohibited without permission.

Table (5-2): Finite element, analytical and optical results for Figures 5.17, 5.18, and 5.19.

Method	Device A1		Device A2		Device C	
	f (kHz)	θ (degree)	f (kHz)	θ (degree)	f (kHz)	θ (degree)
Optical	21.24	6.72[a]	11.3	5.60[b]	34.67	2.42[a]
ANSYS (100% thickness) 100% Nitride	36.49	1.68	16.66	2.12	47.74	0.93
50% Nitride	32.93	2.22	14.91	2.83	42.80	1.24
0% Nitride	26.59	3.66	11.84	4.83	34.15	2.10
ANSYS (80% thickness) 100% Nitride	29.88	3.14	13.40	4.09	38.57	1.78
50% Nitride	26.89	4.16	11.98	5.48	34.54	2.39
0% Nitride	21.62	6.94	9.52	9.39	27.50	4.06
Analytical (80% thickness) 50% Nitride	23.09	5.29				
0% Nitride	20.226	7.4194				

NOTE:
a: the driving current flows through two parallel aluminum traces on the mirror platform;
b: single driving trace on the mirror platform.

As for the device A2 and C, the optical results show good agreement with two FEM models: one is for the device without nitride passivation layer; and in the other model, the nitride layer is firstly diminished by 50%, and then the total device shrinks 20% in thickness. The differences in maximum deflection and in resonant frequency are presented in the Table 5.3.

Reproduced with permission of the copyright owner. Further reproduction prohibited without permission.

Table (5-3): The errors of two finite element analysis models.

	Device A2		Device C	
ANSYS Model	$\Delta f/f_0$	$\Delta\theta/\theta_0$	$\Delta f/f_0$	$\Delta\theta/\theta_0$
Model I: 100% thickness, 0% Nitride	4.8%	13.8%	1.5%	13.2%
Model II: 80% thickness, 50% Nitride	6.0%	2.1%	0.4%	1.2%

NOTE: ($\Delta f/f_0$) is the difference in resonant frequency between simulated and optical results; and ($\Delta\theta/\theta_0$) denotes the difference in maximum deflection.

The dynamic response of device A1 and static deflection results discussed in the section 5.2.3.1 suggests that the actual thickness of micromirror device is smaller than the standard values given by Mitel. All the devices were fabricated in the same batch. Therefore the best-fit ANSYS models for A2 and C would be those with shrinkage in total thickness as well as partial etching on the nitride layer.

The difference between experimental results and finite element simulation could also result from other reasons, such as uncertainties in material properties of the constitute layers, residue and other fabrication problems.

- The values of material properties for thin films are quite different from their bulk values. Differences in material properties used for simulation will result in the difference of the resonant frequencies between simulation and experiment results.
- Mass of residue around the support arms, residual stress, over-etched aluminum layers, breakage and cracks on the arms and platforms, and other fabrication and post-processing defects will all change the resonant frequency of a micromirror device.

Optimization of structure design will be discussed in the later section.

Reproduced with permission of the copyright owner. Further reproduction prohibited without permission.

5.3 Parallel Displacement

5.3.1 Optical Detection Method to test parallel displacement of Micromirrors

The schematic of the experimental setup for testing the parallel displacement is shown in Figure 5.20. Here the collimated Helium-Neon laser was used as a signal light source. The beam enters a beam splitter and is divided into two parts. In the measurement arm, the light reflected from the micromirror is back to the beam splitter and is redirected to a screen. On the other hand, the light folded to the reference arm is then reflected by a fixed reflection mirror. After carefully adjusting the optical components, such as lenses, filters and mirrors, two output beams from measurement and reference arms can yield interference fringes on the opaque screen.

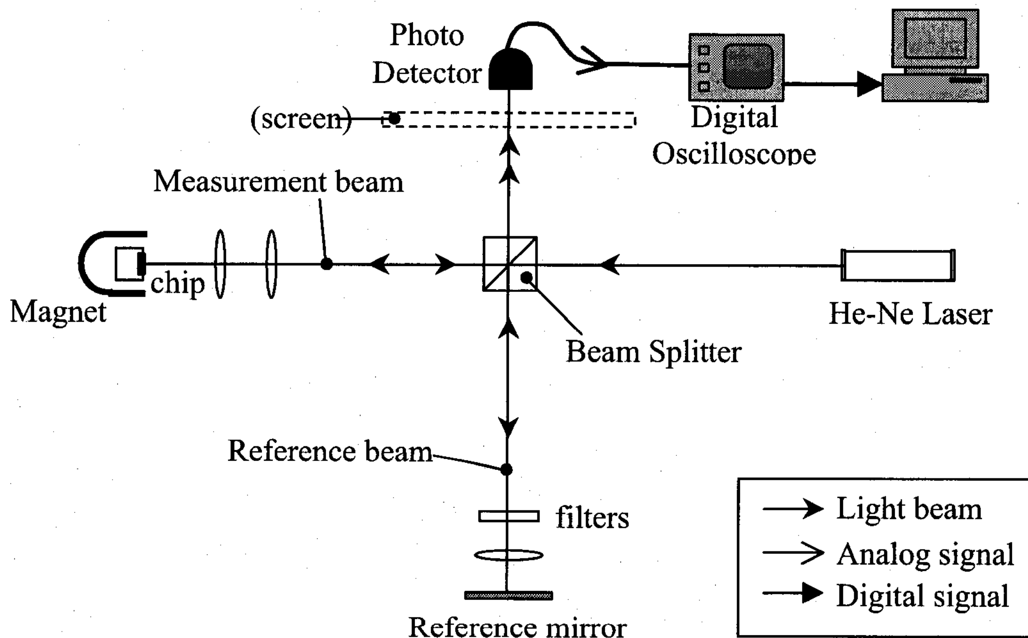

Figure 5.20: The experimental setup for the parallel displacement measurement.

Reproduced with permission of the copyright owner. Further reproduction prohibited without permission.

When micromirror vibrates under activation of a known driving current, the interference fringes moves on the screen. This movement can be also observed using a photo detector, which converts the optical power of interference pattern into a current signal containing information regarding the displacement of the micromirror.

This experimental system is a simple Michelson interferometer. The electric field of the reference beam is:

$$E_r = \mathrm{Re}\{ E_{r0} \exp[j(\omega_0 t - k_0 L_r + \phi_{r0})]\} \tag{5.3.1}$$

where

E_{r0} = complex reference field amplitude,

ω_0 = optical angular frequency,

k_0 = propagation constant in air,

L_r = distance light traveled in the reference beam,

ϕ_{r0} =static phase shift introduced in the reference beam.

Similarly, the electric field of the measurement beam is:

$$E_m = \mathrm{Re}\{ E_{m0} \exp[j(\omega_0 t - k_0 (L_m + 2\delta(t)) + \phi_{m0})]\} \tag{5.3.2}$$

where

E_{m0} = complex reference field amplitude,

L_m = distance light traveled in the measurement beam,

$\delta(t)$ = displacement of the micromirror,

ϕ_{m0} =static phase shift introduced in the measurement beam.

And the resulting interference intensity at the photodetector is:

$$P_{out} = P_r + P_m + 2\sqrt{P_r P_m} \cos[\Phi_0' + 2k_0\delta(t)] \tag{5.3.3}$$

where

P_r = the irradiance of reference light,

P_m = the irradiance of measurement light when micromirror is still,

Φ_0' = static optical path length difference between the measurement and

Reproduced with permission of the copyright owner. Further reproduction prohibited without permission.

reference arms, and $\Phi_0' = 2k_0(L_m - L_r) + \phi_{r0} - \phi_{m0}$.

then

$$P_{out} = P_{tot}\{1 + M\cos[\Phi_0' + 2k_0\delta(t)]\} \tag{5.3.4}$$

where

$\Phi = \Phi_0' + 2k_0\delta(t)$ is phase,

$P_{tot} = P_r + P_m$ is the DC-term,

$M = \dfrac{2\sqrt{P_r P_m}}{P_r + P_m}$ is called the modulation depth of the inference.

The amount of displacement of micromirror $\delta(t)$ can be transduced to phase modulation of the output signal, and then the phase change is converted to the intensity change. When the target mirror produces a large displacement, the interference fringes sensitively move on the screen. The movement of the interference fringes is related to the displacement of the target mirror as follows:

$$\Delta L = n\frac{\lambda}{2} \tag{5.3.5}$$

where n is a specific number of interference fringes to pass by a fixed point on the screen, λ is the wavelength of the laser (0.6328 μm), and ΔL denotes the traveled distance of the micromirror.

5.3.2 Results and Discussion

In the experiments, DC currents were firstly applied to the device. But this interferometric profiler is high sensitive to environment disturbances, such as air currents in the room, table ground vibration and other mechanical drift occurred on optical components in the measurement system. Therefore, the final results of the static response are unstable.

One way to reduce the effect of random noisy signals is to perform measurement by

Reproduced with permission of the copyright owner. Further reproduction prohibited without permission.

using AC driving currents to introduce phase modulation. Several different wave types of AC currents have been applied on micromirror devices both with and without the external magnetic field. The amplitude of current wave was also changed, as shown in Figure 5.21 (a) and (b), which show the driving input signals and output signals from the photo detector. The upper traces in (a) and (b) indicate the sine wave voltage inputs over a 500 Ω resistor placed in series with the device. The lower traces in both figures indicate the interference fringe movements.

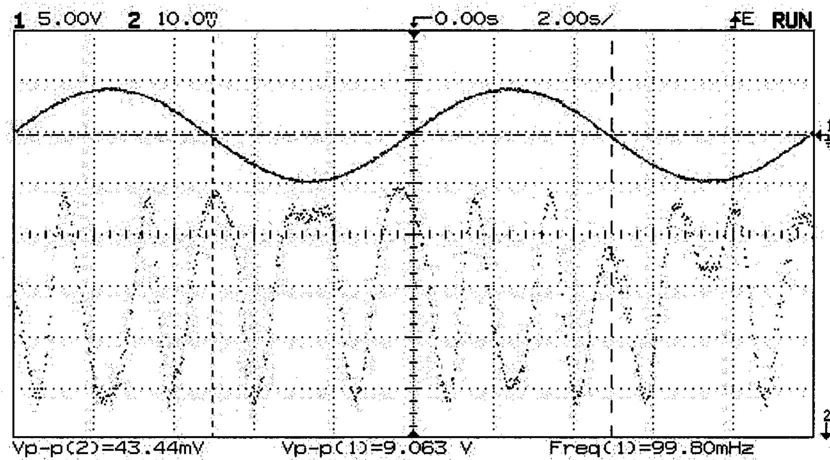

(a)

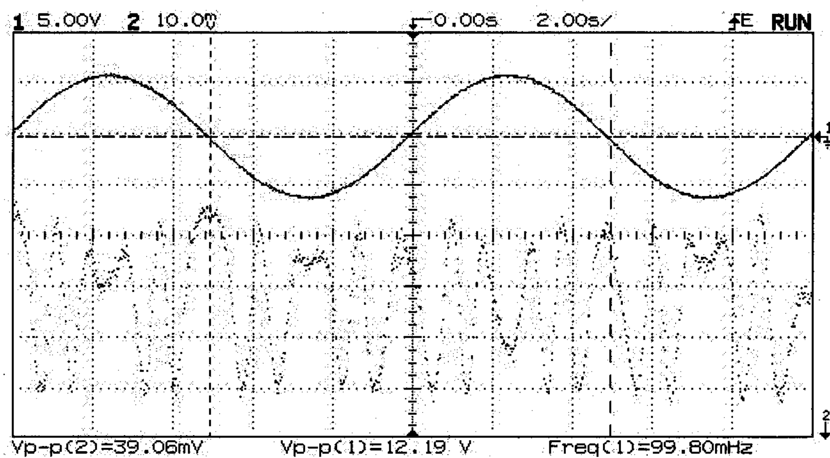

(b)

Figure 5.21: The interference fringe movements under different driving currents.

Reproduced with permission of the copyright owner. Further reproduction prohibited without permission.

In Figure 5.21, more interference fringes moved in (b) than in (a) because the input voltage signal in (b) (12.19 V_{pp}) is larger than that in (a) (9.063 V_{pp}). Also, more interference fringes moved in the half cycle of positive signals than the periods of negative signal input both in (a) and (b).

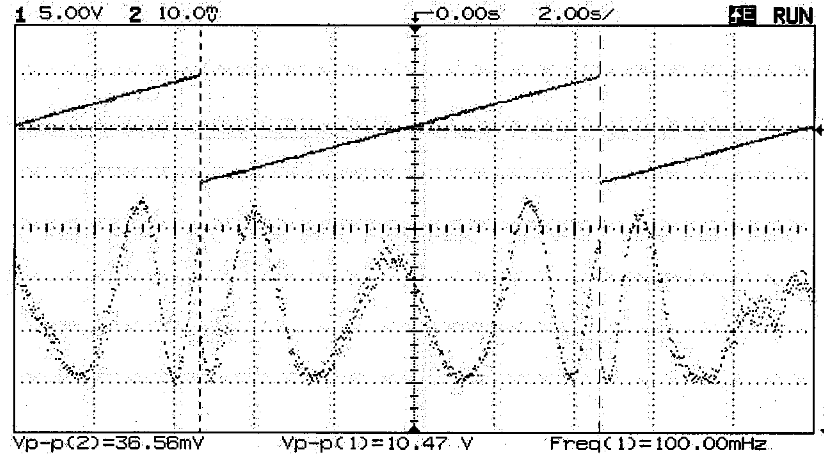

(a) with an external magnetic field

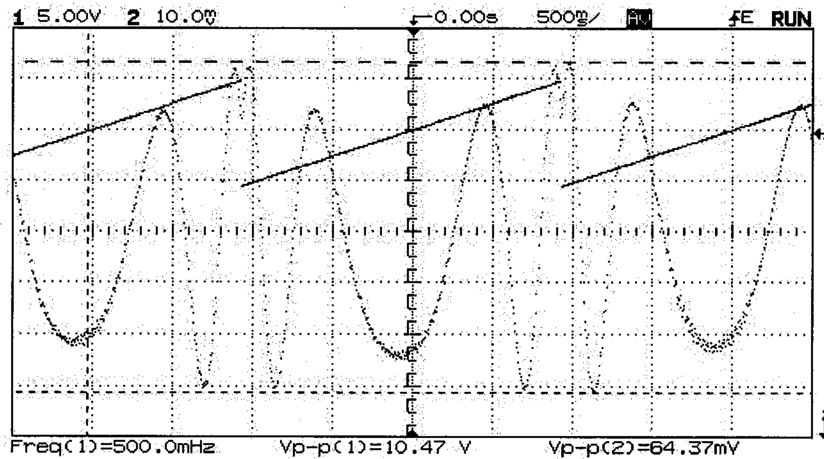

(b) without external magnetic field

Figure 5.22: The interference fringe movements with or without external magnetic field.

Reproduced with permission of the copyright owner. Further reproduction prohibited without permission.

Figure 5.23 compares the results from micromirror movements under an external magnetic field (a) and those without external magnetic field (b). Figure 5.23 (b) shows the interference fringes move symmetrically in both negative and positive half cycle. However, the fringes will move faster in the positive half cycle than in negative one when there is an external magnetic field as shown in Figure 5.23 (a). The difference of movements is a result from the thermal effect.

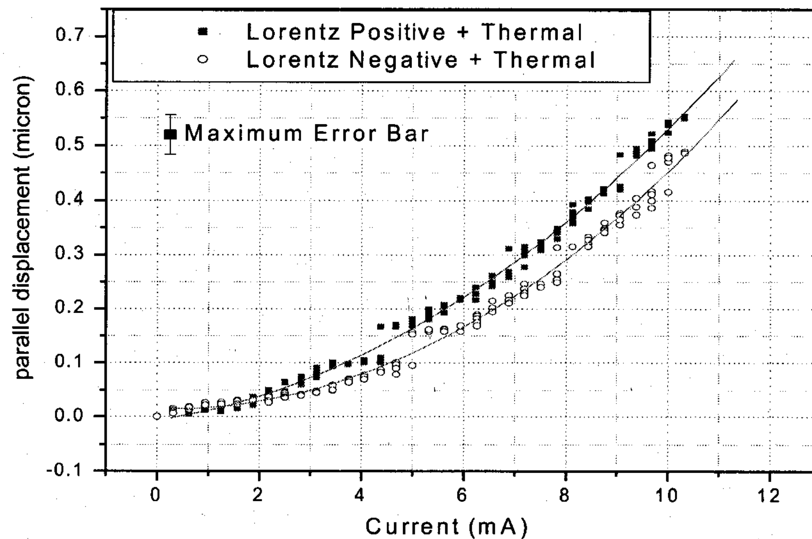

Figure 5.23: The parallel displacement of the micromirror device A1.

Figure 5.23 shows the parallel displacement of a micromirror device A1. The labels "Lorentz positive" and "Lorentz Negative" denote the movement of micromirror under positive or negative driving currents. The label "Thermal" indicates the movement contributed by thermal effects.

Figure 5.24 shows the result of parallel displacement of the micromirror device. The thermal effects have been deducted from the results illustrated in Figure 5.23. The variation of data is quite large, because the parallel displacement of micromirror is obtained from phase analysis and there are many reasons other than thermal effects, which could also modulate phase of the output signal of the photo detector.

Reproduced with permission of the copyright owner. Further reproduction prohibited without permission.

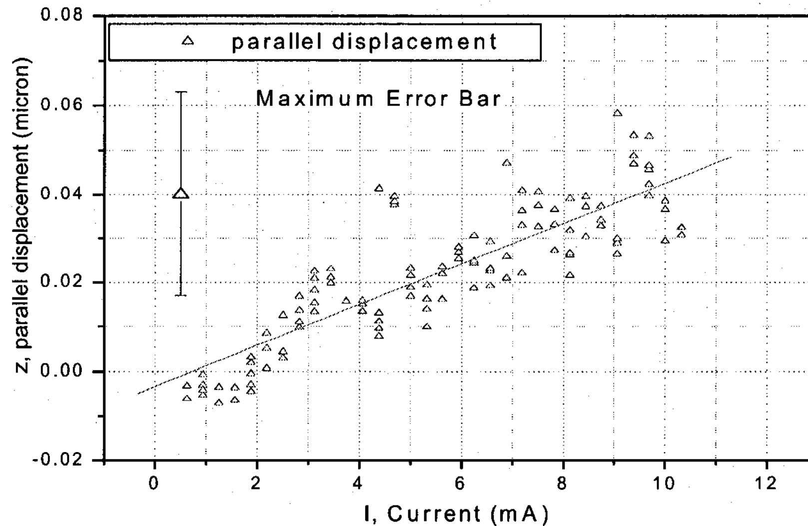

Figure 5.24: The parallel displacement of the micromirror device A1 due to Lorentz force only.

Incident laser beam is directed to the center of mirror plat in the experiment to measure parallel movement. At low frequency, the micromirror platform performs a parallel displacement. However, it was found that tilting of actuated micromirror was observed at resonant frequency. That is because micromirror platforms are not exactly symmetric.

As reported, several measurement systems have been built up to measure the vertical displacement of MEMS devices, such as the system using common path heterodyne profilometers or differential profilometers, using phase shifting methods, or using self referencing [33-38].

Reproduced with permission of the copyright owner. Further reproduction prohibited without permission.

5.4 Device Design and Optimization

As discussed in Chapter 3, the performance of micromirror devices was largely determined by the structure of support arms. Thus the optimization of micromirror structure could be mainly focused on the design of support arms.

Several micromirror devices, which have the same mirror platform design but different shape of support arms, were simulated and tested. The simulation and experimental results show that the Device A2, under the same actuation current, can generate the largest deflection on the mirror platform than other designs studied in this project. More complicate arm design can be developed to further improve the performance of micromirror devices.

Even for the same design of support arms, there are several factors important to optimize the performance, such as the length, width and thickness of a support arm.

If the support arm is considered to be a simply supported beam, by Hook's Law, the longer the beam is, the larger amount of torsion or bending is achieved in the end of the beam. Also, reducing the width and thickness of support arms can minimize the moment of inertia of the arm and reduce the overall stiffness of the micromirror device, therefore produce a larger deflection on the mirror.

However, the fragility of the support arm also increases when the arm becomes longer and/or thinner. After post-processing, a residual stress inherent throughout the device causes the free ends of micromirror structures to spring out of the plane of the CMOS die. For a simply support beam, the critical stress, or the stress at which this structure will fail is given by [39]:

$$\sigma_{critical} = \frac{\pi^2 EI}{L^2 A} \tag{5.4.1}$$

Reproduced with permission of the copyright owner. Further reproduction prohibited without permission.

where ***I*** is the moment of inertia, ***L*** is the length, and ***A*** is the cross-sectional area of the support arm. The device with longer support arms is more prone to breakage than the device with shorter arms, because the critical stress for the former is smaller. For the same reason, increasing the thickness and the width of support arms will create a more robust device. Furthermore, in the fabrication processes, increasing the width of support arms will potentially protect the aluminum layer from over-etching, which often occurred in the region where aluminum is very close to the edge open to the substrate and could be damaged from side of the support arm by seepage between the oxide layers.

The previous study by [40] also indicates that there is a design threshold for the length and/or width of the structures that can be designed and successfully fabricated using CMOS technology.

Finite element modeling of the device designs can simulate device performance before fabrication, therefore it can be used to predict the optimum design of support arms.

5.5 Potential Applications

There are many possible applications for magnetically actuated micromirror devices, such as:

- Optical switches and interferometer: under different actuation modes, the vibration of the micromirror structures may be used as an optical chopper, a switch or an interferometer.
- Magnetic field sensor: The motion of the micromirror is a function of the external magnetic field. Thus the deflection of the micromirror device could be used to measure the magnetic field intensity.
- Resonant sensor: the resonant frequency of the structure is sensitive to a variety of measurands, such as pressure and the mass of the moving structure. Thus the

Reproduced with permission of the copyright owner. Further reproduction prohibited without permission.

micromirror device can be designed as a pressure sensor or a mass sensor.

- Optical scanner: large tilt can be achieved as the micromirror device is excited at its resonant frequency. Therefore the device can be used as a miniature optical scanner, which is a key component in the image display and detector system.

Many other potential applications could be also developed for magnetically actuated micromirrors. For all the practical applications, devices still need greatly optimization.

Reproduced with permission of the copyright owner. Further reproduction prohibited without permission.

Chapter 6

Conclusions and Future Work

6.1 Magnetically Actuated Micromirror devices

Novel magnetically actuated CMOS micromachined micromirror devices have been introduced, characterized, and simulated in this thesis.

The work presented in this thesis includes four major parts: (1) Several micromirror devices with different support arm structures were designed, fabricated using standard CMOS technology, and post-processed; (2) Analytical estimation for static and dynamic behaviors for the simplest design of micromirror device; (3) ANSYS simulation of the static deflection and dynamic response under the different actuation modes, such as angular tilting and parallel displacement; (4) Experimental characteristics. The experimental results were then compared with the data obtained from simple analytical estimation or finite element simulation.

The deflections of the devices in parallel displacement mode were determined to be small. But, under the torsional actuation, the micromirror device produced appreciable angular deflection, especially when device vibrated at the resonant frequency. In angular tilting mode, good agreement exists between the experimental results, ANSYS simulation and analytical estimation. The static angular deflection of the micromirror devices varies linearly with the actuating currents. Moreover, it was observed that the experimental

Reproduced with permission of the copyright owner. Further reproduction prohibited without permission.

results of the micromirror devices coincided to the model prediction obtained when nitride passivation layer was excluded from the model both in static and dynamic analysis. It is therefore hypothesized that the topmost nitride layer on the micromirror device was etched during the post processing in XeF_2. Last, compared with the analytical calculation and ANSYS simulation results, the structure stiffness and resonant frequency of micromirror devices obtained from the experiments also indicated that the thickness of practical device is smaller than in the original design. This could come from the thickness deviation of layers in CMOS fabrication process.

6.2 Future work

The work presented in this thesis is preliminary, and future research may include:

- Device Optimization. As mentioned in this thesis, some fabrication problems, such as over-etched aluminum regions, were due to intentional violation of CMOS design rules. The solution is to optimize the micromirror devices according to the design criteria that ensure compatibility of MEMS design with CMOS manufacturing protocols.
- Device simulation. First, finite element modeling is a faster and relative economical approach for device optimization compared with the development process only including fabrication and test. Second, the micromirror models need further improvement. For example, the models built up with element type SOLID92 can be used after sub-structuring process, which will increase the calculation speed. Last, other than structural analysis, the electromagnetic analysis can be performed in ANSYS multi-physics environment. This analysis can be useful for evaluating the Lorentz force actuation method compared to the traditional methods, such as voltage differential method. Also thermal loads can be analyzed for micromirror devices.

Reproduced with permission of the copyright owner. Further reproduction prohibited without permission.

- Anisotropic etching. Silicon etching using XeF_2 is fast, simple and cost effective. However, the isotropic nature of the etchant results in the undercutting problem of the device. The device etched using XeF_2 is fragile and easy to cracking or breaking. Good structures could be attained through anisotropic etching, such as TMAH etching. But the appropriate etching process must be developed in order to protect aluminum layer from TMAH, and to solve the problem of low reproducibility.

- Piezoresistive detection. Based on the piezoresistive characteristics of the polysilicon resistor, the static deflection and the dynamic response of the micromirror devices could be also detected by measuring the resistance of the polysilicon resistor embedded in the structures.

- On-die magnet. The magnetic field of the micromirror actuation is provided by an external magnet. Further development of the device may include the depositing a thin film of magnet material on same die.

- Develop custom micromachined micromirror devices. Standard CMOS fabrication process may significantly reduce performance of optical devices compared to custom micromachining in the issues such as shape control, thermal stability, and heat dissipation.

Reproduced with permission of the copyright owner. Further reproduction prohibited without permission.

References

[1] S.M. Spearing, "Materials Issues in Microelectromechanical Systems (MEMS)", *Acta Mater.*, vol. 48, 2000, pp 179-196

[2] K.E. Peterson, "Silicon as a Mechanical Material", *Proc. IEEE*, vol. 17 no. 5, May 1982, pp 420-457

[3] H.C. Nathanson, W.E. Newell, R.A. Wickstron and J.R. Davis Jr., "The Resonant Gate Transistor", *IEEE Trans. Electron Dev.*, vol. ED-14, 1967, pp 117-121

[4] Y.C. Tai, R.S. Muller, "Pin Joints, Gears, Springs, Cranks, and Other Novel Micromechanical Structures", *Tech. Digest, Transducers '87*, 1987, p. 853

[5] W.S.N. Trimmer, M. Mehregany, "Microgears and Turbines Etched from Silicon", *Tech. Digest, Transducers '87*, 1987, p.853

[6] M. Parameswaran, H.P. Baltes, A.M. Robinson, "Polisilicon Microbridge Fabrication Using Standard CMOS Technology", *Digest of Technical Papers, IEEE Solid-State Sesors and Actuators Workshop*, Hilton Head Island, June 1988, pp 148-150

[7] M. Parameswaran, "Microelectronic and Micromechanical Sensors and Actuators in CMOS Technology", *Ph.D. Thesis*, University of Alberta, Canada, 1990

[8] M. Parameswaran, H.P. Baltes, Lj. Ristic, A.C. Dhaded, and A.M. Robinson, "A New Approach for the Fabrication of Micromechanical Structures", *Sensor and Actuators*, vol. 19, 1989, pp 289-307

Reproduced with permission of the copyright owner. Further reproduction prohibited without permission.

[9] O. Brand, H. Baltes and U. Baldenweg, "Thermally Excited Silicon Oxide Beam and Bridge Resonators in CMOS Technology", *IEEE. Trans. On Electron. Devices*, vol. 40, No. 10, October 1993

[10] Yuan Ma, "CMOS Optical Micro-Radiator Vacuum Sensor", *Ph.D. Thesis*, University of Alberta, Canada, 2002

[11] K.B. Brown, "Gas Pressure Measurements with Cantilever-in-Cantilever Micro-structures", *MSc Thesis*, University of Alberta, Canada, 1999

[12] A. Gotz, I. Garcia, C. Cane, E.L. Tomayo etc., "Micromachined Solid State Integrated Gas Sensor for the Detection of Aromatic Hydrocarbons", *Sensors and Actuators*, B44, no. 1-3, pt 5(1997), pp. 483-487

[13] Jacobs-Cook A.J., Bowen M.E.C. "Novel optical fibre/microresonator interfacing technology", *Sensors and Actuators,* A37-38, 540-545 (1993)

[14] Rao Y.J., Culshaw B. "Comparison between optically excited vibrations of silicon cantilever and bridge microresonators", *Sensors and Actuators,* A30, 203-208 (1992)

[15] Hassaun Jones-bey, "The Big World of Little MEMS", *Laser Focus World*, Jan. 2001, p 122-130

[16] C.R. Giles, V. Aksyuk, "Silicon MEMS Optical Switch Attenuator and its Use in Lightwave Subsystems", *IEEE Journal on Selected Topics in Quantum Electronics*, vol. 5 n1, Jan-Feb 1999, p 18-25

[17] M. Hoffmann, P. Kopka, "Bistable Micromechanical Fiber-optic Switches on Silicon with Thermal Actuators", *Sensors and Actuators, -A: Physical*, vol 78 n1, Nov. 1999, p 28-36

[18] R. Goering, T. Martin, "Miniaturized Piezoelectrically Driven Fiber Optic Switches with Transmittive Microoptics", *Proceedings of SPIE The*

Reproduced with permission of the copyright owner. Further reproduction prohibited without permission.

International Society for Optical Engineering, vol. 3878, 1999, p 136-143

[19] Evan L. Goldstein, Lih-Yuan Lin, "Lightwave Micromachines for Optical Networks", *Optics & Photonics New*, Mar. 2001, p 60-65

[20] M. Bourne, "MEMS Move Quickly into the Optical-switching Market", *WDM Solutions*, Jan. 2001, p 27-29

[21] D. Mlynek, Y. Leblebici, Ph. Renaud, "Intelligent Cross-Bar Switch for Optical Telecommunications based on Micro-Mirror Array", *from the web site:* http://www.ece.wpi.edu/~leblebic/switch/

[22] Shi-Sheng Lee, Long-Sun Huang, "Free-space Fiber-Optic Switches Based on MEMS Vertical Torsion Mirrors", *Journal of Lightwave technology*, vol. 17 n 1, Jan. 1999, p 7-13

[23] Kuntao Ye and Fred R. Beyette Jr., "Characterization of a monolithic silicon MEMS technology in standard CMOS process," *SPIE Conference on Optoelectronic Information Processing*, Denver CO, August 2001.

[24] G. Yan, Philip C.h. Chan, I-Ming Hsing etc., "An improved TMAH Si-etching Solution Without Attacking Exposed Aluminum", *Sensors and Actuators*, A89, 2001, ppt 135-141

[25] M. Paranjape, A. Pandy, S. Brida, "Dual-doped TMAH Silicon Etchant for Microelectromechanical Structures and Systems Applications", *J. Vac. Sci. Technol., A* 18(2), Mar/Apr 2000, ppt. 738-742

[26] The on-line database: "*MEMS* and *Nano*technology Clearinghouse" at http://www.memsnet.org/material/silicondioxidesio2film/

[27] Daryl L. Logan, "Mechanics of Materials", *HarperCollis Publishers Inc.*, New York, 1991

Reproduced with permission of the copyright owner. Further reproduction prohibited without permission.

[28] Roark and Young, "Formulas for Stress and Strain: Fifth Edition", *McGraw-Hill Inc.*, 1975

[29] F.P. Beer, E.R. Johnston, Jr., "Mechanics of Materials", McGraw-Hill Ryerson, Toronto, 1985

[30] J.P. Den Hartog, "Mechanical Vibration", *Dover*, 1985

[31] Singiresu S. Rao, "Mechanical Vibrations", *Addison-Wesley Publishing Company*, 1990

[32] Y. Ma, "Magnetically Actuated CMOS Micromachined CIC Devices", *MSc Thesis*, University of Alberta, Canada, 1997

[33] A.D. Kersey, M. Coke and D.A. Jackson, "Linearized Polarimetric Optical Sensor Using a Heterodyne-type Signal Recovery Scheme", *Electron. Lett.* 20, 1984, pp. 209

[34] H. Zhao, R. Liang, L. Dacheng etc., "Practical Common-path heterodyne Surface Profiling Interferometer with Automatic Focusing", *Opt. Lasers Technol.*, 33, 2001, 259-65

[35] X. Chen, M. Gramalia, J. Yeazell, "Phase-shifting Interferometry with Uncalibrated Phase Shift", *Appl. Opt.*, 2000, 38, 585-91

[36] K.E. Okada, J. McKelvie, "Reference Phase Shift Determination in Phase Shifting Interferometry", *Opt. Lasers Eng*, 1995, 22, 77-90

[37] K. Okada, A. Atsushi and J. Tsujiuchi, "Simultaneous Calculation of Phase Distribution and Scanning Phase in Phase Shifting interferometry", *Opt. Commun.*, 1991, 84, 118-24

[38] Z. Ge, "Self-reference Method for Phase-shift Interferometry", *Proc. SPIE*, 2001, 4416, 152-7

Reproduced with permission of the copyright owner. Further reproduction prohibited without permission.

[39] A.P. Boresi, R.J. Schmidt, O.M. Sidebottom, "Advanced Mechanics of Materials: Fifth Edition", *John Wiley & Sons*, 1993, U.S.A

[40] J. Wylde and T. Hubbard, "Elastic Properties and Vibration of Micromachined Structures Subject to Residual Stresses", *IEEE Can. Conf. Electrical and Computer Engineering*, Edmonton, 1999

Reproduced with permission of the copyright owner. Further reproduction prohibited without permission.

Appendix A

The calculation of twist angle on the support arm in device A1

The simplest micro-mirror device A1 is shown in Figure A.1. In this figure, L_a denotes the length of support arm, and L_d indicates the distance between two parallel aluminum traces on the platform. L_s is the effective length of one driving trace, while B and I_s are the external magnetic field and driving current, respectively.

When driving currents have opposite directions in the two parallel aluminum traces on opposite edges of the platform, Lorentz forces produce the platform tilt around the support arms. The arms are considered to be rigid at supports A and D. The mechanical equilibrium is obtained when the mechanical restoring torque is equal to the magnetic torque.

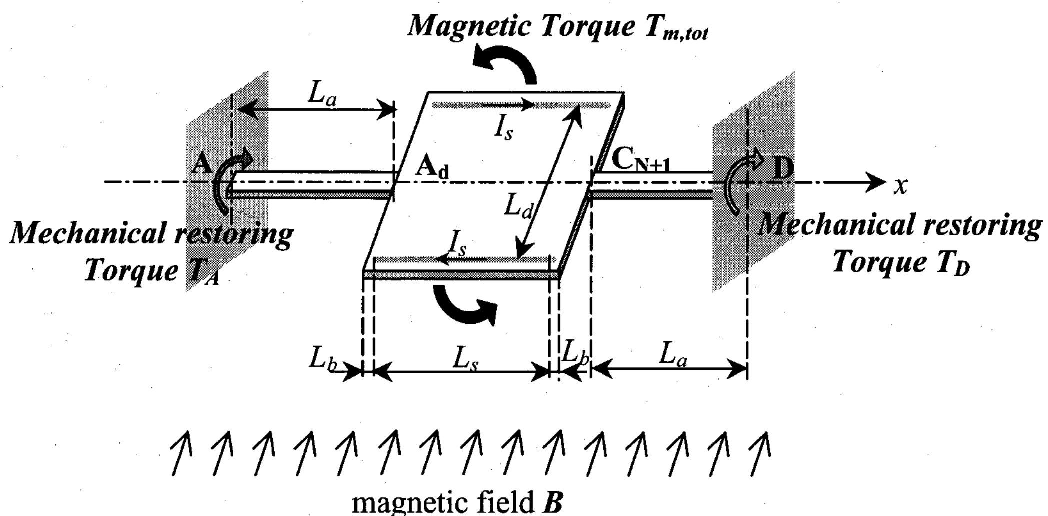

Figure A.1: The mechanical equilibrium of the micromirror device A1

Reproduced with permission of the copyright owner. Further reproduction prohibited without permission.

The torsional equation of equilibrium is

$$T_A + T_D = T_{m,tot} = 2(BL_sI_s)\frac{L_d}{2}\cos\theta = (BL_sI_s)L_d\cos\theta \approx (BL_sI_s)L_d \tag{A.1}$$

Here, θ is the rotation angle. In practice, θ is very small, then $\cos\theta$ (≈ 1) can be ignored. And the device is symmetric, then

$$T_A = T_D = \frac{T_{m,tot}}{2} \tag{A.2}$$

➢ ***Twist angles:***

The Lorentz force applied on one aluminum trace actually is uniformly distributed load. Therefore, firstly, we divide the platform into *N+2* segments (A_dC_0, C_0C_1, … , $C_{N-1}C_N$, C_NC_{N+1}) along x-direction. The first segment BC_0 and the last segment C_NC_{N+1} do not have magnetic torques applied on them, and the length is L_b, which is the distance from the end of aluminum trace to the border of platform. As for other *N* segments, the length of each segment equals to L_s/N. Then the magnetic torque generated on each segment is given by

$$T_{m0} = BI_sL_d(L_s/N) = T_{m,tot}/N \tag{A.3}$$

where $T_{m,tot}$ is the total magnetic torque.

Secondly, we cut sections one at a time through AA_d, A_dC_0, C_1C_2, … , C_NC_{N+1}, and $C_{N+1}D$ to determine the internal torque in each section:

Section AA_d and A_dC_0:

T_A is the mechanical restoring torque on point A. Then the internal torques T_{AAd} and T_{AdC0} can be expressed in terms of the reaction torques by drawing free-body diagrams of sections of the device as shown. The resulting equations are:

Reproduced with permission of the copyright owner. Further reproduction prohibited without permission.

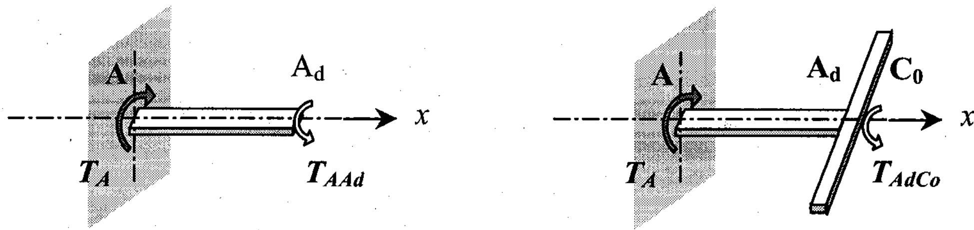

$$\sum T = 0: \qquad T_{AA_d} = T_A \tag{A.4}$$

$$\sum T = 0: \qquad T_{A_dC_0} = T_A \tag{A.5}$$

Section C_0C_1:

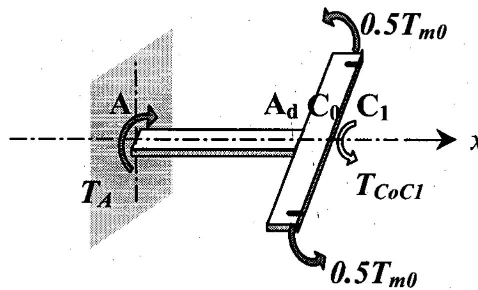

$$\sum T = 0: \qquad T_{C_0C_1} = T_A - T_{m0} \tag{A.6}$$

Section $C_{k-1}C_k$:

$$\sum T = 0: \qquad T_{C_{K-1}C_K} = T_A - kT_{m0} \tag{A.7}$$

Section $C_{N-1}C_N$:

$$\sum T = 0: \qquad T_{C_{N-1}C_N} = T_A - NT_{m0} \tag{A.8}$$

Section C_NC_{N+1}:

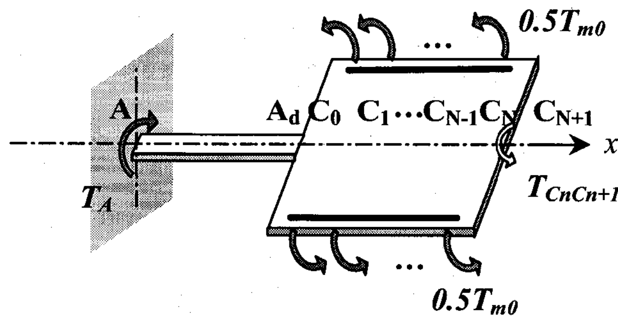

Reproduced with permission of the copyright owner. Further reproduction prohibited without permission.

$$\sum T = 0: \qquad T_{C_N C_{N+1}} = T_A - NT_{m0} \tag{A.9}$$

Section $C_{N+1}D$:

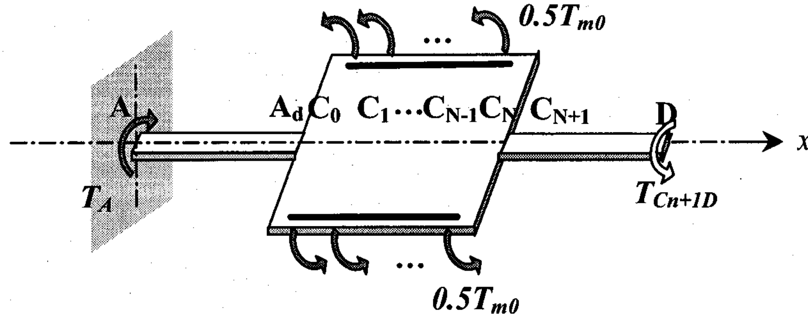

$$\sum T = 0: \qquad T_{C_{N+1}D} = T_A - NT_{m0} = -T_D \tag{A.10}$$

Next, considering the geometry of deformation, we observe that the total angle of twist is zero because the device is fixed at both ends. Therefore an additional equation is given by

$$\Phi_{total} = 0 \tag{A.11}$$

or

$$\Phi_{AA_d} + \Phi_{A_dC_0} + \Phi_{C_0C_1} + \cdots + \Phi_{C_{k-1}C_k} + \cdots + \Phi_{C_{N-1}C_N} + \Phi_{C_NC_{N+1}} + \Phi_{C_{N+1}D} = 0$$

For linear elastic materials, the rate of change of angular twist over the length L is formulated by [27]

$$\frac{\Phi}{L} = \frac{T}{(GJ)} \tag{A.12}$$

then

Reproduced with permission of the copyright owner. Further reproduction prohibited without permission.

$$\begin{aligned}\Phi_{total} &= \left(\frac{TL}{GJ}\right)_{AA_d} + \left(\frac{TL}{GJ}\right)_{A_dC_0} + \left(\frac{TL}{GJ}\right)_{C_0C_1} + \cdots + \left(\frac{TL}{GJ}\right)_{C_{N-1}C_N} + \left(\frac{TL}{GJ}\right)_{C_NC_{N+1}} + \left(\frac{TL}{GJ}\right)_{C_{N+1}D} \\ &= \frac{T_AL_a}{(GJ)_{AA_d}} + \frac{T_AL_b}{(GJ)_{A_dC_0}} + \frac{(T_A - T_{m0})(L_s/N)}{(GJ)_{C_0C_1}} + \cdots \\ &\quad + \frac{(T_A - kT_{m0})(L_s/N)}{(GJ)_{C_{K-1}C_K}} + \cdots + \frac{(T_A - NT_{m0})(L_s/N)}{(GJ)_{C_{N-1}C_N}} \\ &\quad + \frac{(T_A - NT_{m0})L_b}{(GJ)_{C_NC_{N+1}}} + \frac{(T_A - NT_{m0})L_a}{(GJ)_{C_{N+1}D}} \\ &= 0 \end{aligned} \tag{A.13}$$

(GJ), known as the torsional rigidity, is determined by the cross section geometry and mechanical properties of the torsion beam. In this device, two arms are symmetric, therefore

$$(GJ)_{AA_d} = (GJ)_{C_{N+1}D} = (GJ)_a \tag{A.14}$$

Practically, the small segments of micro-mirror platform are not exactly same, because the distribution of aluminum traces along x-axis is not always uniform, as illustrated in Figure 3.4. But the disordered area (in A_dC_0 and C_NC_{N+1} sections) is only a small part of the whole platform, and the properties of aluminum and silicon dioxide are quite similar by the Table (3-1); thus we assume all segments of the platform have the same value of (GJ):

$$(GJ)_{A_dC_0} = (GJ)_{C_0C_1} = (GJ)_{C_NC_{N+1}} = (GJ)_b \tag{A.15}$$

By combining (A.13), (A.14), and (A.15), we can get

$$T_A\left[\frac{2L_a}{(GJ)_a} + \frac{2L_b + L_s}{(GJ)_b}\right] = NT_{m0}\left[\frac{L_a}{(GJ)_a} + \frac{L_b}{(GJ)_b}\right] + \frac{(N+1)}{2}\frac{T_{m0}L_s}{(GJ)_b} \tag{A.16}$$

When N is a quite large number, using equation (A.3), we obtain

$$\frac{N+1}{2}T_{m0} \approx \frac{N}{2}T_{m0} = \frac{T_{m,tot}}{2} \tag{A.17}$$

Reproduced with permission of the copyright owner. Further reproduction prohibited without permission.

here $T_{m.tot}$ is the total magnetic torque on the whole platform. Then, from equations (A.16) and (A.17), we can also get the restoring torque T_A and T_D, as same as equation (A.2)

$$T_A = T_D = \frac{T_{m,tot}}{2}$$

By the equations above, twist angle of each section can be obtained as well. The twist angle on point A_d is:

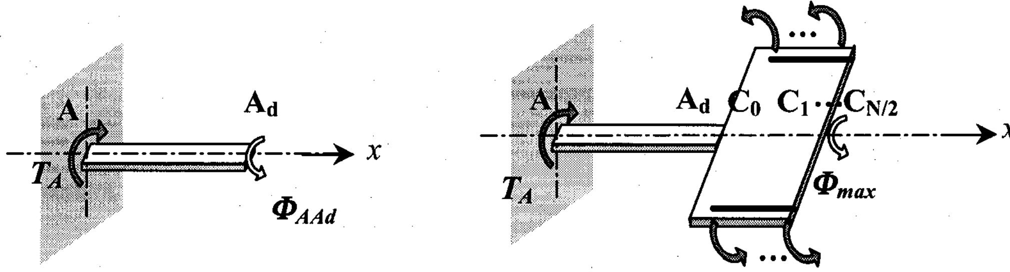

$$\Phi_{AA_d} = \frac{T_A L_a}{(GJ)_a} = \frac{T_{m,tot} L_a}{2(GJ)_a} \tag{A.18}$$

The maximum twist angle occurs just at the middle of the platform (perpendicular to the x-axis), and this angle is given by

$$\begin{aligned} \Phi_{\max} &= \Phi_{AA_d} + \Phi_{A_dC_0} + \Phi_{C_0C_1} + \ldots + \Phi_{(N/2-1),N/2} \\ &= \frac{T_A L_a}{(GJ)_a} + \frac{T_A L_b}{(GJ)_b} + \sum_{n=1}^{N/2} \frac{(T_A - nT_{m0})(L_s / N)}{(GJ)_b} \\ &\approx \frac{T_{m,tot} L_a}{2(GJ)_a} + \frac{T_{m,tot} L_b}{2(GJ)_b} + \frac{T_{m,tot} L_s}{8(GJ)_b} \\ &(N \gg 1) \end{aligned} \tag{A.19}$$

Reproduced with permission of the copyright owner. Further reproduction prohibited without permission.

Appendix B

B-I: Figures of ANSYS Simulation Results

The following pictures were captured from ANSYS result plots.

(a) parallel movement in z direction;

(b) stress distribution when moved as in (a);

(c) Rotation around the x-axis;

(d) stress distribution when moved as in (c).

Figure B.1: Example of static deflection on micromirror device A1.

Reproduced with permission of the copyright owner. Further reproduction prohibited without permission.

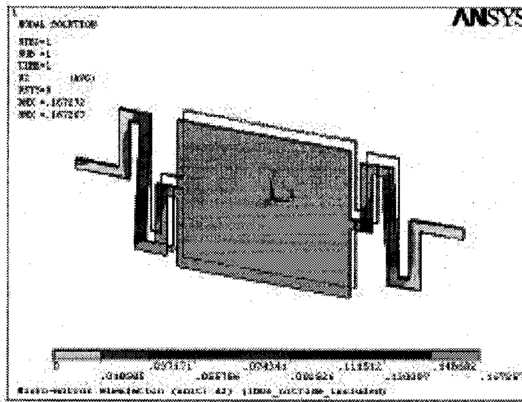

(b) parallel movement in z direction;

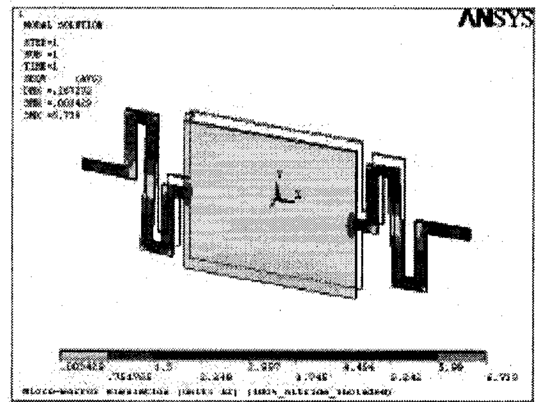

(b) stress distribution when moved as in (a);

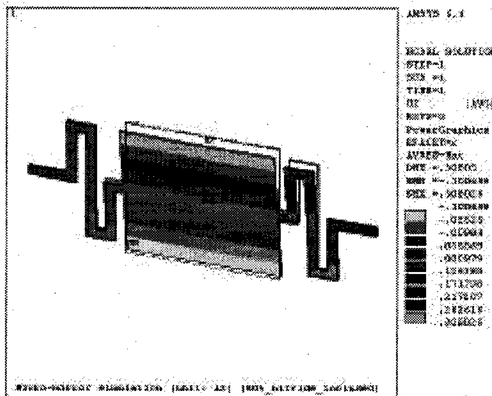

(c) Rotation around the x-axis;

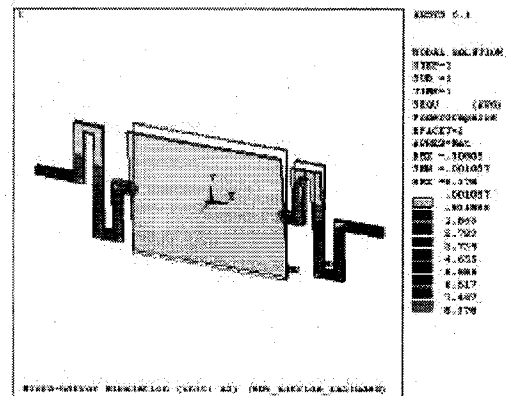

(d) stress distribution when moved as in (c).

Figure B.2: Example of static deflection on micromirror device A2.

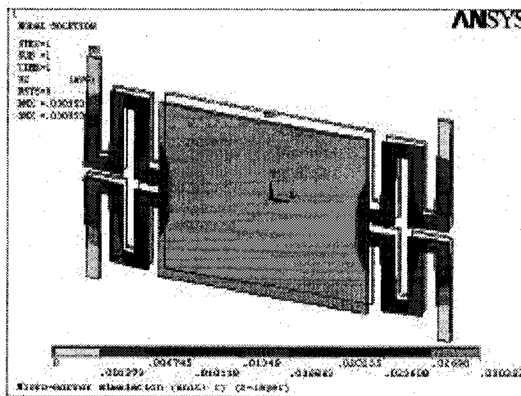

(c) parallel movement in z direction;

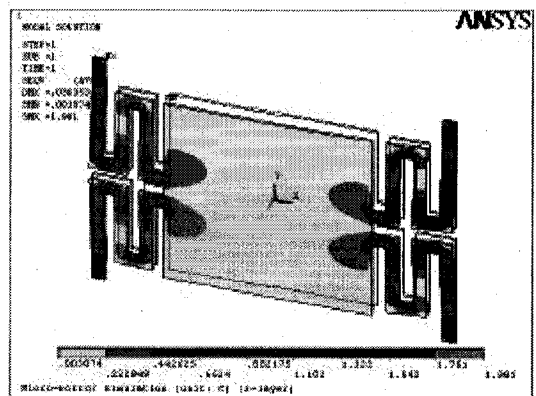

(b) stress distribution when moved as in (a);

Figure B.3: Example of static deflection on micromirror device C.

Reproduced with permission of the copyright owner. Further reproduction prohibited without permission.

(c) Rotation around the x-axis;

(d) stress distribution when moved as in (c).

Figure B.3: Example of static deflection on micromirror device C (continued).

(a) parallel movement in z direction;

(b) stress distribution when moved as in (a);

Figure B.4: Example of static deflection on micromirror device B.

Reproduced with permission of the copyright owner. Further reproduction prohibited without permission.

(c) Rotation around the x-axis; (d) stress distribution moved as in (c).

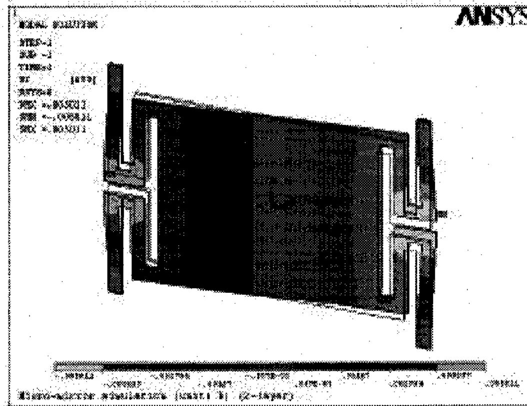

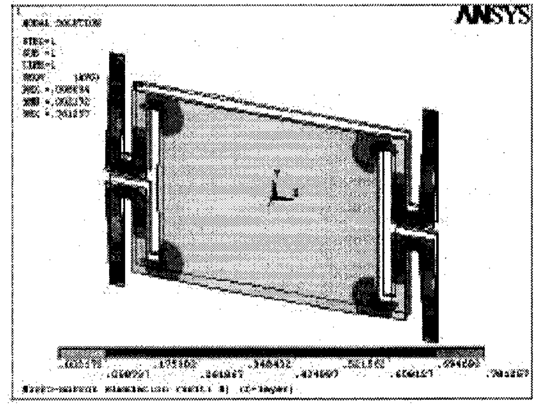

(e) Rotation around the y-axis; (f) stress distribution when moved as in (e).

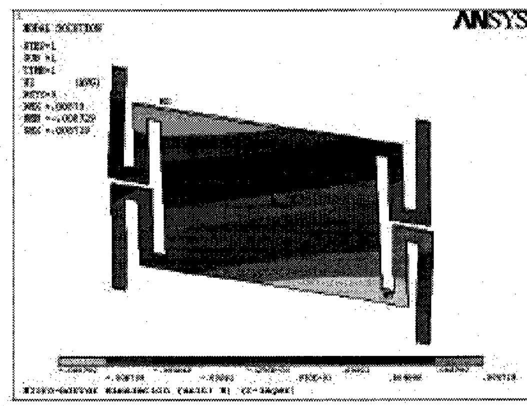

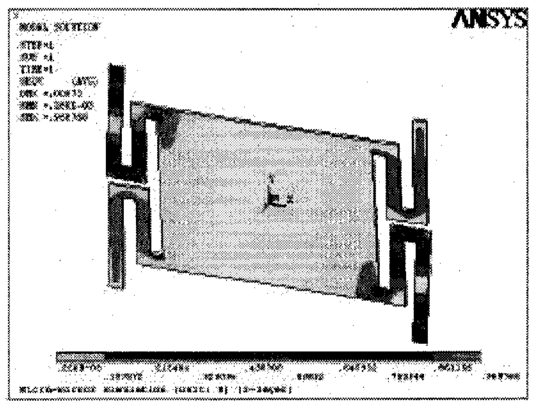

(g) Rotation around the xy direction; (h) stress distribution when moved as in (g).

Figure B.4: Example of static deflection on micromirror device B (continued).

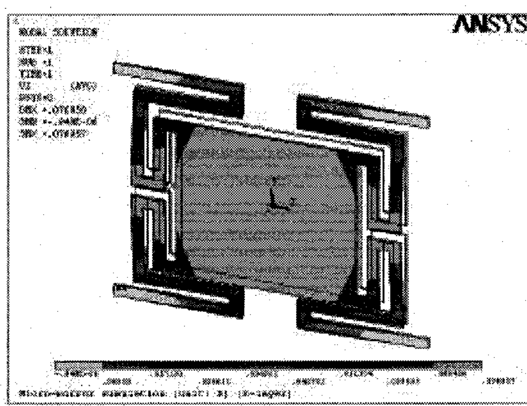

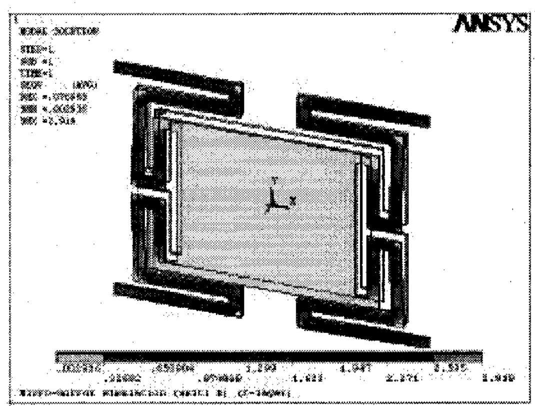

(a) parallel movement in z direction; (b) stress distribution when moved as in (a);

Figure B.5: Example of static deflection on micromirror device D.

Reproduced with permission of the copyright owner. Further reproduction prohibited without permission.

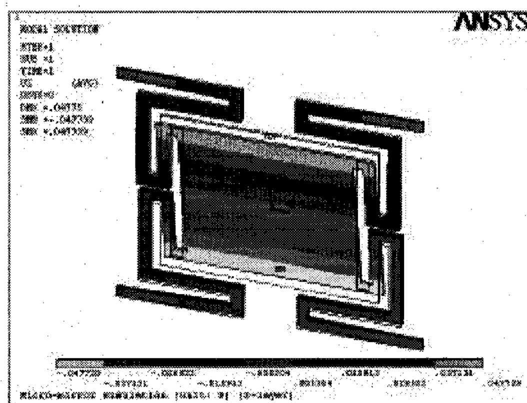

(c) Rotation around the x-axis;

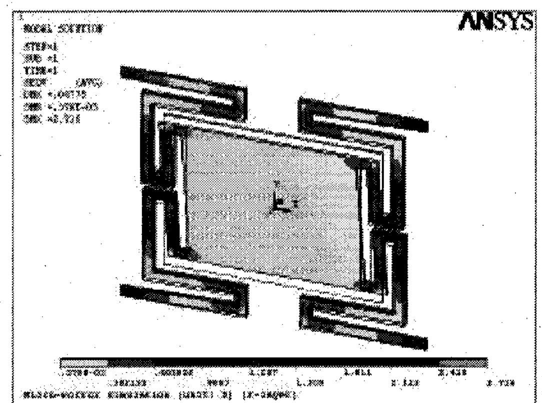

(d) stress distribution when moved as in (c).

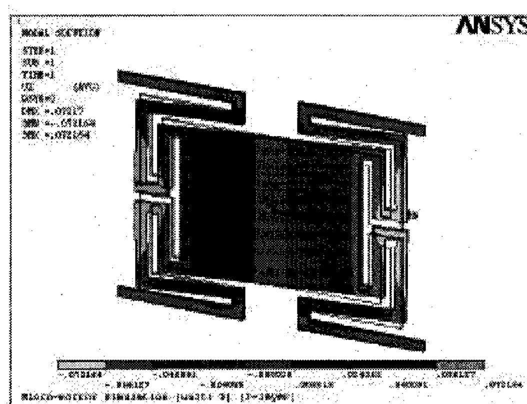

(e) Rotation around the y-axis;

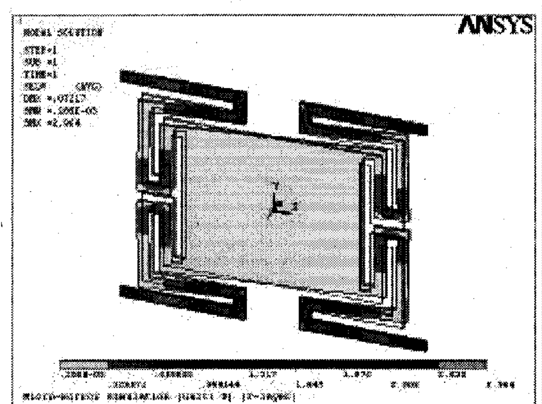

(f) stress distribution when moved as in (e).

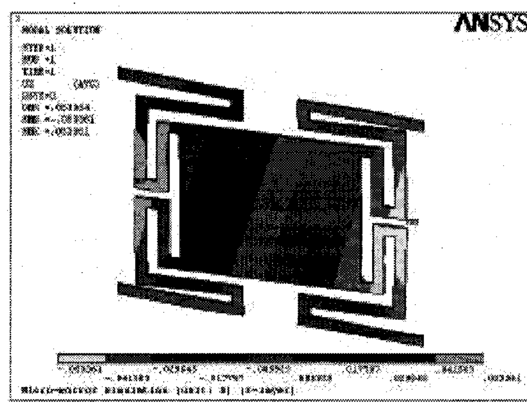

(g) Rotation around the xy ;

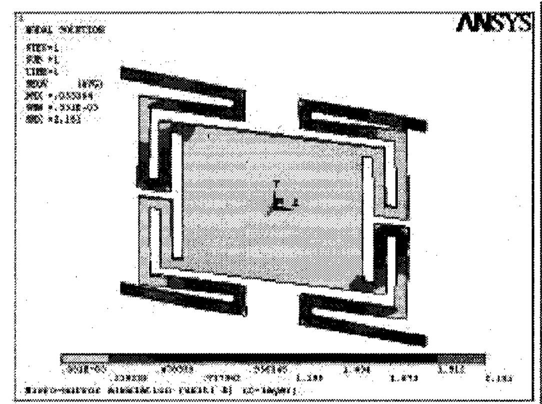

(h) stress distribution when moved as in (g).

Figure B.5: Example of static deflection on micromirror device D (continued).

Reproduced with permission of the copyright owner. Further reproduction prohibited without permission.

B-II: ANSYS Simulation Command files

The following are example ANSYS command files, utilized to compile the FEM results presented in Chapter 4 and 5. Device geometry, material properties, meshing control, constrains and loads are all defined in the files.

Device A1:

```
/filnam,sd46_A1
/TITLE, Micro-mirror simulation (unit: A1) (2-layer)
/PREP7

!*******************************************************
!generate model:

th1=0.5             !th1: nitride layer
xt=1.0              !ratio of  nitride layer (xt>0.0)
t1=xt*th1           !thickness of nitride layer

x2=1.0              !ratio of oxide layer (for passivation layer)
th2=4.1+0.5*x2      !th2=1.5+0.8+1.0+0.8+0.5=4.6 (no nitride layer)
th2_2=4.1           !th2=1.5+0.8+1.0+0.8 (no passivation layer)

tk=t1+th2           !total thickness

!------------------------------------------------------------------------------------
!define material properties: from
http://www.memsnet.org/material/silicondioxidesio2film/
!Young's modulus [(kg.microns/s^2)/(microns^2)]

MP,EX,1,75000       !Material Prop. for silicon dioxide: E = 75GPA
MP,PRXY,1,,0.17     !Material Prop. for silicon dioxide: poisson's ratio=0.17
MP,DENS,1,2.2e-15   !Material Prop. for silicon dioxide: density [kg/(microns^3)]

MP,EX,2,380000      !Material Prop. for nitride: Young's mudulus E=380GPA
MP,PRXY,2,,0.24     !Material Prop. for nitride: Poisson's ratio=0.24
MP,DENS,2,3.1e-15   !Material Prop. for nitride: density [kg/(microns^3)]

MP,EX,3,74140       !Material Prop. for aluminum: Young's mudulus E=74.14GPA
MP,PRXY,3,,0.33     !Material Prop. for aluminum: Poisson's ratio=0.33
```


Reproduced with permission of the copyright owner. Further reproduction prohibited without permission.

```
MP,DENS,3,2.7e-15    !Material Prop. for aluminum: density [kg/(microns^3)]

!*******************************************************************
!define element type and options
!Element Type: layered solid element "Solid46"

ET,1,SOLID46,0,0,1,0,2,0  !keyopt(1)~(6)
keyopt,1,8,0              !kop(8) for solid46
keyopt,1,9,0              !kop(9) for solid46
keyopt,1,10,0             !kop(10) for solid46

!------------------------------
!define the real constant set 1
!------------------------------
!if there is a nitride layer:
R,1,2,0,1,2,,             !
RMORE,1,,,,,              !1 means: buttom of the body is  the reference plan
RMORE,1,90,th2,2,90,t1,                    !materials, thickness, and orientations


!------------------------------
!define the real constant set 2
!------------------------------
!if there is a nitride layer:
R,2,6,0,1,6,,             !
RMORE,1,,,,,              !1 means: buttom of the body is  the reference plan
RMORE,1,90,1.5,3,90,0.8,
RMORE,1,90,1.0,3,90,0.8,
RMORE,1,90,0.5,2,90,t1


!----------------------------------------------------
!define the real constant set 1 (without nitride layer)
!----------------------------------------------------
!if there is a nitride layer:
!R,1,1,0,1,1,,            !
!RMORE,1,,,,,             !1 means: buttom of the body is  the reference plan
!RMORE,1,90,th2           !materials, thickness, and orientations


!----------------------------------------------------
!define the real constant set 2 (without nitride layer)
!----------------------------------------------------
```


Reproduced with permission of the copyright owner. Further reproduction prohibited without permission.

```
!if there is a nitride layer:!R,2,5,0,1,5,,                    !
!RMORE,1,,,,,           !1 means: buttom of the body is  the reference plan
!RMORE,1,90,1.5,3,90,0.8,
!RMORE,1,90,1.0,3,90,0.8,
!RMORE,1,90,(0.5*x2)


!****************************************************
!Define constants of mirror design
Lm1=135                 !Mirror width--X
Lm2=125                 !Mirror height--Y
t=8                     !Trace width
b=20                    !arm width

tb2=25                  !mirror to edge--Y
tb1=25                  !mirror to edge--X
La=200                  !length of one arm

sx=Lm1+tb1+La           !width of opening (half)

!---------------------------------------------
!Define blocks of left_arm
!---------------------------------------------
block,-sx,-(Lm1+tb1),0,b/2,0,tk

!--------------------------------
!!Define blocks of half platform
!--------------------------------
block,-Lm1,0,0,b/2,0,tk
block,-Lm1,0,b/2,Lm2,0,tk
block,-Lm1,0,Lm2,(Lm2+tb2/2),0,tk
block,-Lm1,0,(Lm2+tb2/2),(Lm2+tb2),0,tk

block,-(Lm1+tb1/2),-Lm1,0,b/2,0,tk
block,-(Lm1+tb1/2),-Lm1,b/2,Lm2,0,tk
block,-(Lm1+tb1/2),-Lm1,Lm2,(Lm2+tb2/2),0,tk
block,-(Lm1+tb1/2),-Lm1,(Lm2+tb2/2),(Lm2+tb2),0,tk

block,-(Lm1+tb1),-(Lm1+tb1/2),0,b/2,0,tk
block,-(Lm1+tb1),-(Lm1+tb1/2),b/2,Lm2,0,tk
block,-(Lm1+tb1),-(Lm1+tb1/2),Lm2,(Lm2+tb2/2),0,tk
block,-(Lm1+tb1),-(Lm1+tb1/2),(Lm2+tb2/2),(Lm2+tb2),0,tk

VSYMM,X,ALL,,,0,
```


Reproduced with permission of the copyright owner. Further reproduction prohibited without permission.

```
VSYMM,Y,ALL,,,0,

vglue,all

!*************************************************************
!create mesh by specifying number of elements along given lines
!!a1=40                  !elements number along support arms
!!a2=8
b1=10                    !elements number along half-platform x
b2=10                    !elements number along half-platform y
b3=15                    !elements number along arm x

lesize,59,,,1,,,,,       !only one element along thickness

lesize,639,,,b1,,,,,0
lesize,671,,,b1,,,,,0
lesize,19,,,b2,,,,,0
lesize,648,,,b2,,,,,0

lesize,7,,,b3,,,,,0
lesize,163,,,b3,,,,,0

mshkey,1
esize,2
smrtsize,,,,2,,,,,,,,
vmesh,all

asel,all
vsel,all
esel,all

finish
save,,
!------------------------------------------------------------


!*******************************************************
/clear,nostart

resume,sd46_A1,db
/filnam,sd46_A1_DCro
/stitle,1,DC test load (Ix=25mA)

/solu
```


Reproduced with permission of the copyright owner. Further reproduction prohibited without permission.

```
!enter analysis type
antype,0                !static analysis
eqslv,front,,           !try frontal methods first
!!eqslv,pcg,1e-7


!Add zero displacement constraint at beginning of each arm
DA,5,ALL,0
DA,315,ALL,0
DA,83,ALL,0
DA,347,ALL,0

!Define forces that will act on structure
Lplat=(270+25)*1e-6   !length of Al trace in platform [m]

Ix=(25/1000)            !DC current [A]
B=0.1                   !magnetic field [Tesla]
!all forces have unit of [kg.microns/s^2]
F1=(Ix*Lplat*B/3.0)*(1000000)

!on plate:
FK,64,FZ,F1
FK,31,FZ,F1
FK,168,FZ,F1

FK,272,FZ,-F1
FK,239,FZ,-F1
FK,376,FZ,-F1
!*****************************************************
solve
fini
save,,
!*****************************************************
```

☞ The codes listed above are example input files for ANSYS simulation of micromirror devices. Models and simulation conditions are adjusted in the analysis process. For instance, harmonic and modal analyses are performed by replacing codes in solution phase of above command files.

Reproduced with permission of the copyright owner. Further reproduction prohibited without permission.